

225274
132p.

**SPACE-TIME EVOLUTION OF CYCLOTRON
MASER INSTABILITIES GENERATING
AURORAL KILOMETRIC RADIATION**

A. Bers and A. K. Ram

Plasma Fusion Center

Massachusetts Institute of Technology

Cambridge, MA 02139

Final Report of Accomplishments

April 1, 1990 – March 31, 1994

NASA Grant No. NAGW-2048

Final Report of Accomplishments

April 1, 1990 – March 31, 1994

NASA Grant No. NAGW-2048

SPACE-TIME EVOLUTION OF CYCLOTRON MASER INSTABILITIES GENERATING AURORAL KILOMETRIC RADIATION

A. Bers and A. K. Ram

TABLE OF CONTENTS

Abstract	1
Introduction	1
Accomplishments	2
Appendix A	A1
Paper in <i>Physics of Space Plasmas</i> (1990), SPI Conference Proceedings and Reprint Series, Number 10	
Appendix B	B1
Abstract and viewgraphs of the oral presentation at the 1990 fall meeting of the American Geophysical Union	
Appendix C	C1
Paper in <i>Geophysical Research Letters</i>	
Appendix D	D1
Abstract and viewgraphs of the oral presentation at the 1991 fall meeting of the American Geophysical Union	
Appendix E	E1
Paper in <i>Physics of Space Plasmas</i> (1991), SPI Conference Proceedings and Reprint Series, Number 11	
Appendix F	F1
Paper in <i>Plasma Physics and Controlled Fusion</i>	
Appendix G	G1
Paper in <i>Physics of Space Plasmas</i> (1993), SPI Conference Proceedings and Reprint Series, Number 13	

This is the final report of accomplishments in the time period from April 1, 1990 to March 31, 1994 under the NASA Grant No. NAGW-2048.

ABSTRACT

The research carried out on this three-year grant was on the space-time evolution of electron cyclotron maser-like electromagnetic instabilities. Specifically, the work was aimed at understanding the conditions for the emission of radiation at the fundamental of and the harmonics of the electron cyclotron frequency. This was done with the purpose of explaining the observed features of auroral kilometric radiation (AKR). Our research also included work on the nonlinear evolution of the three wave interaction. The three wave interactions are ubiquitous to a variety of plasmas, including those in the solar loops, and may explain the saturation of some types of AKR. The last part of our research was on nonlinear wave-particle interactions. Within the auroral regions, acceleration of ions by electrostatic waves has been observed. The work carried out was on basic aspects of nonlinear wave-particle interactions when the wave frequency is an integer multiple of the ion-cyclotron frequency.

INTRODUCTION

Our work was motivated by the need to understand the detailed properties of radiation emitted by loss-cone type of electron distribution functions. This was done for the purposes of comparing proposed theoretical models with observed characteristics of auroral kilometric radiation (AKR). It has been established that relativistic electrons with a loss-cone distribution in the auroral region is the source of AKR [C. S. Wu and L. C. Lee, *Astrophys. J.*, **230**, 621 (1979)]. The instability giving rise to AKR is known as the cyclotron-maser instability (CMI) and has been extensively studied since it was initially proposed [see C. S. Wu, *Space Sci. Revs.*, **41**, 215 (1985), and references therein]. However, in order to make detailed comparisons between the properties of CMI and the observations, it was necessary to study the space-time evolution of CMI. This was the principal focus of our grant.

In addition, we initiated two studies on nonlinear interactions relevant to space plasma

physics in a broader context: the space-time evolution of nonconservative three-wave interactions (3WI) in which one wave is unstable and the other two are damped; and the acceleration of ions by chaotic dynamics induced by lower-hybrid waves which are typically at high multiples of the ion-cyclotron frequency.

In the following, we summarize our accomplishments in these three studies, and append copies of our relevant publications.

ACCOMPLISHMENTS

In this NASA grant-supported research, we established the distinguishing features between absolute and convective instabilities generated by anisotropic electron distribution functions in an ambient magnetic field. We then studied the properties of such instabilities when propagating across the magnetic field. This was done in order to understand the harmonic emission of AKR which was first pointed out by Benson [R. F. Benson, *J. Geophys. Res.*, **90**, 2753 (1985)] and later by others from different observations.

The use of the Green's function analysis [see A. Bers, in *Handbook of Plasma Physics*, Vol. 1, Chapter 3.2, eds. M. W. Rosenbluth and R. Z. Sagdeev (North-Holland, 1983), and references therein] to determine the distinguishing properties of absolute and convective instabilities was presented in an invited talk at the 1990 Cambridge Workshop in Geoplasma Physics and published in the proceedings of this conference [A. K. Ram and A. Bers, in *Physics of Space Plasmas (1990)*, Proceedings of the 1990 Cambridge Workshop in Geoplasma Physics, SPI Conference Proceedings and Reprint Series, Number 10, eds. T. Chang, G. B. Crew, and J. R. Jasperse (Cambridge, MA: Scientific Publ. Inc., 1991), pp. 351–365], attached in Appendix A. This work pointed out for the first time that bursts of radiation with narrow bandwidth in frequency could be associated with an absolute instability and did not require any feedback mechanisms as had been proposed earlier [W. Calvert, *J. Geophys. Res.*, **87**, 8199 (1982)].

At the 1990 American Geophysical Union meeting in San Francisco (December 3–7, 1990) we presented in an oral session the application of the pinch-point technique to electromagnetic instabilities of the type generated in the auroral regions [Appendix B]. For the first time, we presented the spectral differences between absolute and convective

instabilities. These spectral differences are important in correlating theoretical models with observations.

A paper detailing the Green's function and pinch point technique, its domain of validity, and its important features was published in *Geophysical Research Letters* [Appendix C]. This paper cleared previous misconceptions on absolute and convective instabilities and the use of the pinch point technique to determine the nature of instabilities in a linearly unstable medium.

At the 1991 American Geophysical Union meeting in San Francisco (December 9–13, 1991), we presented, in an oral session, the application of the pinch point technique to determine the nature of the electromagnetic instabilities of the type generated in the auroral regions [Appendix D]. We considered those instabilities that propagate across the ambient magnetic field and studied in detail the emission at the fundamental of and the second harmonic of the electron cyclotron frequency (ω_{ce}). Our objective was to determine, within the realm of linear instability theory, the size of the source region required for AKR to achieve substantial amplitudes, and the conditions for the generation of harmonic AKR. One of the interesting features of the pinch point, Green's function analysis, is that it determines the pulse-front velocity of the unstable wavepackets in the medium. Our previous studies [G. Francis, A. K. Ram, and A. Bers, *Phys. Fluids*, **29**, 255 (1986)] have demonstrated that this pulse-front velocity of propagation is not intuitively obvious for a given dispersion relation of unstable waves. For the electron cyclotron maser instabilities, we find that for low densities ($\omega_{pe}/\omega_{ce} \lesssim 10^{-2}$, where ω_{pe} is the electron plasma frequency), the emission at ω_{ce} is an absolute instability whose pulse-front velocity is nearly the speed of light. As the density is increased this velocity decreases. From these pulse-front velocities, we can determine the scale lengths of the density inhomogeneities required for the linearly growing wavepacket to reach a given amplitude. For instance, when $\nu_{ce} = \omega_{ce}/2\pi = 500$ kHz in order to have a linear growth to 4 e-foldings, the scale length required at $\omega_{pe}/\omega_{ce} = 0.01$ is about 123 km while for $\omega_{pe}/\omega_{ce} = 0.142$ the scale length is about 4 km. (The other parameters needed to get these numbers are indicated in Appendix D.) For $\omega_{pe}/\omega_{ce} > 0.144$ the instability at ω_{ce} with phase velocities greater than the speed of light (c) are stabilized. For $\omega_{pe}/\omega_{ce} \lesssim 0.144$ the instability at ω_{ce} is an absolute instability with

phase velocities greater than c , and thus not subject to Landau damping. The instability at $2\omega_{ce}$ is convective for phase velocities greater than c and absolute for phase velocities less than c . The scale length for this emission to grow to 4 e-foldings for $\omega_{pe}/\omega_{ce} = 0.01$ is about 42 m. However, this instability can be stabilized by thermal effects for slightly oblique propagation across the magnetic field. This limits the instability to propagate almost directly across the magnetic field. This may explain why emission at harmonics is not observed all the time and also why this emission is not observed very far away from the source region.

On a more general and basic physics level, we also studied the nonlinear space-time evolution of the three-wave interaction (3WI) with an unstable growing pump coupled to two damped daughter waves. This could be one of the saturation mechanisms for the cyclotron maser instabilities discussed above. The three-wave interaction is a generic plasma phenomenon which has been encountered in a variety of plasmas. The time evolution of the spatially uniform 3WI has been used to explain the observational features of the solar flare plasma [L. Vlahos, R. R. Sharma, and K. Papadopoulos, *Astrophys. J.*, **275**, 374 (1983)]. The time evolution model has been extensively studied and found to exhibit chaotic behavior when there is dephasing in the 3WI [J. M. Wersinger, J. M. Finn, and E. Ott, *Phys. Fluids*, **23**, 1142 (1980)]. Since instabilities, even in the linear case, propagate in space and time, the spatio-temporal behavior of the 3WI needed to be studied. While the conservative 3WI (where the pump does not grow and the daughter waves do not damp) has been studied extensively, both numerically and analytically [D. J. Kaup, A. H. Reiman, and A. Bers, *Rev. Mod. Phys.*, **51**, 915 (1979)], ours has been the first effort at understanding the non-conservative 3WI. One of the interesting features that came out of these studies is the observation of spatio-temporal chaos: the chaotic interaction of spatially localized structures. This did not require that the 3WI be dephased. The localized structures would manifest themselves as bursts when observed by satellites travelling through the unstable medium. An overview of the spatio-temporal evolution of the 3WI was presented at an invited talk of the 1991 Cambridge Workshop in Theoretical Geoplasma Physics (June 24–28, 1991) and published in the proceedings [Appendix E], and, as an invited talk, at the 1992 International Conference on Plasma Physics, Innsbruck, Austria. The latter was

then published as a paper in a journal [Appendix F].

The final part of our research was to study the nonlinear wave-particle interaction for the purposes of understanding the transverse acceleration of ions by electrostatic waves in the auroral zones. The basic aspects of the nonlinear interaction and the interesting aspects of the interaction when the wave frequency is an integer multiple of the ion-cyclotron frequency were presented in an invited talk at the 1993 M.I.T. Symposium on the Physics of Space Plasmas: “Chaos, Stochasticity, and Strong Turbulence,” and published in the proceedings [A. K. Ram and A. Bers, in *Physics of Space Plasmas (1993)*, Proceedings of the 1993 Cambridge Workshop in Geoplasma Physics and the 1993 M.I.T. Symposium on the Physics of Space Plasmas: “Chaos, Stochasticity, and Strong Turbulence,” Number 13, eds. T. Chang and J. R. Jasperse (Cambridge, MA: M.I.T. Center for Theoretical Geo/Cosmo Plasma Physics, 1995), pp. 341–377]. This paper is attached in Appendix G.

APPENDIX A

SPI CONFERENCE PROCEEDINGS AND REPRINT SERIES

Series Editor: T. S. Chang

Number 10

Physics of Space Plasmas (1990)

*Proceedings of the
1990 Cambridge Workshop in Geoplasma Physics on
Magnetic Fluctuations, Diffusion and
Transport in Geoplasmas and the
1990 MIT Winter Symposium on the
Physics of Space Plasmas*

EDITORS

T. Chang, G. B. Crew and J. R. Jasperse



Scientific Publishers, Inc.

ABSOLUTE VERSUS CONVECTIVE ANALYSIS OF INSTABILITIES IN SPACE PLASMAS

Abhay K. Ram and Abraham Bers
Plasma Fusion Center, M.I.T., Cambridge, MA 02139

ABSTRACT

A brief description of the pinch-point analysis of the Green's function for studying the space-time evolution of instabilities in a homogeneous medium is presented. This analysis determines if an instability propagates in space-time as an absolute instability or as a convective instability. The pinch-point technique is applied to the study of electron cyclotron maser type of instabilities. Such instabilities are believed to be a source of some types of observed planetary, solar and stellar emissions, and, in particular, of auroral kilometric radiation. The pinch-point analysis also brings out the spectral differences between absolute and convective instabilities that should be important in correlating theoretical models with observations.

I. INTRODUCTION

Laboratory, Space, and Astrophysical plasmas are rich sources of electromagnetic radiation whose intensities are above the thermal levels of emission. There are two generic ways of generating this radiation. The first is due to some internal sources of free energy which excite, from noise, an instability inside the plasma. This occurs, for instance, due to spatial gradients or anisotropies inherent in the plasma. The second way that the plasma acts as a source of electromagnetic radiation is by stimulated scattering of some of the externally incident electromagnetic waves. This may happen when the incident waves couple nonlinearly to some normal modes of the plasma and unstably drive, from noise, the scattered radiation from inside the plasma. In either case, the instability evolves in the free energy source region leading, eventually, to electromagnetic radiation propagating out of the plasma.

An aspect of the radiation that is observed and measured by a detector or a probe, located in the source region or far away from it, is the intensity of the emission as a function of either the frequency or the wavelength of the emission. In order to understand the emission, one would like to know about the onset of the instability that leads to the observed emission, the propagation in space and time of the instability through the source region and beyond, and, finally, the evolution towards the saturated nonlinear state which is eventually observed. In this paper we are going to

discuss features of the linear evolution and propagation of instabilities in a homogeneous medium that would have distinguishable signatures in the observed spectra.

The linear evolution and propagation of instabilities in a homogeneous medium has been discussed before [1]. The essence of the Green's function technique used in these studies is presented in section II. In section III this technique is applied to the propagation of cyclotron maser type of instabilities. Such instabilities are considered to be a source of auroral kilometric radiation [2, 3]. The characteristic features associated with the propagation of such instabilities through space and time are also discussed in section III.

II. GREEN'S FUNCTION ANALYSIS OF INSTABILITIES

The propagation of a small amplitude signal in a homogeneous medium is described by an equation of the form:

$$\mathcal{L} \vec{\psi}(\vec{r}, t) = \int d^3 r' \int dt' \overline{\overline{M}}(\vec{r} - \vec{r}', t - t') \cdot \vec{\psi}(\vec{r}', t') + \vec{S}_{ext}(\vec{r}, t) \quad (1)$$

where \mathcal{L} is a linear operator, $\vec{\psi}$ is a vector function describing the small amplitude signal, $\overline{\overline{M}}$ describes the medium through which the signal is propagating, and \vec{S}_{ext} is either a noise source or an external source acting on the medium. The space-time Fourier transform of the above equation yields:

$$\overline{\overline{D}}(\vec{k}, \omega) \cdot \vec{\psi}(\vec{k}, \omega) = \vec{S}_{ext}(\vec{k}, \omega) \quad (2)$$

where $\overline{\overline{D}}$ is a sum of the Fourier transform of the left-hand side of Eq. (1) and the Fourier transform of $\overline{\overline{M}}$. If, for some real \vec{k} , the corresponding ω 's satisfying $\det \{ \overline{\overline{D}}(\vec{k}, \omega) \} = D(\vec{k}, \omega) = 0$ (where \det denotes the determinant) are such that the imaginary part of ω is > 0 , then the medium is considered to be unstable to a perturbation with that particular \vec{k} and ω . Eq. (2) can be solved for $\vec{\psi}(\vec{k}, \omega)$, so that the solution to Eq. (1) is given by:

$$\vec{\psi}(\vec{r}, t) = \int_L \frac{d\omega}{2\pi} \int_F \frac{d^3 k}{(2\pi)^3} \frac{\overline{\overline{D}}_{adj}(\vec{k}, \omega) \cdot \vec{S}_{ext}(\vec{k}, \omega)}{D(\vec{k}, \omega)} \exp(i\vec{k} \cdot \vec{r} - i\omega t) \quad (3)$$

where $\overline{\overline{D}}_{adj}$ is the adjoint matrix of $\overline{\overline{D}}$, and L and F are the appropriate Laplace and Fourier contours of integration, respectively, which are chosen to satisfy causality [1].

While Eq. (3) gives the general space-time propagation of a signal in a medium driven by \vec{S}_{ext} , we are usually interested in the natural response of the medium. The Green's function technique gives a physical and general insight into the response properties of the medium [4]. The Green's function solution, $\vec{G}(\vec{r}, t)$, is obtained by replacing \vec{S}_{ext} in Eq. (1) by $\delta(\vec{r})\delta(t)\vec{I}$, where \vec{I} is the identity tensor. The Green's function approach is equivalent to evaluating the response of the medium to a localized, broadband, "white" noise source. The response to a general perturbation is then obtained by convolving the Green's function with the perturbation [4].

In what follows, we shall consider scalar fields, ψ , and only one spatial dimension. For this case the Green's function is given by:

$$G(z, t) = \int_L \frac{d\omega}{2\pi} \int_F \frac{dk}{2\pi} \frac{1}{D(k, \omega)} \exp(ikz - i\omega t) \quad (4)$$

where k is the wave-number in the z direction. The generalization to vector fields and higher spatial dimensions is more complicated but can be carried out in a straightforward manner.

Even for simple dispersion functions, $D(k, \omega)$, it is frequently difficult to compute the Green's function analytically. However, we are not generally interested in the transient solution to $G(z, t)$. Rather, we would like to know the time-asymptotic behavior of $G(z, t)$. It has been determined that, in an unstable medium, the time-asymptotic evolution of $G(z, t)$ can belong to one of only two possible categories [5, 6]:

- (a) an *absolute instability*, where the response grows in time and encompasses more and more of the space as a function of time – the response always including the spatial location of the initial perturbation; thus, every spatial point eventually becoming unstable;
- (b) a *convective instability*, where the response grows in time but propagates away from its point of origin; thus, any spatial point eventually becoming stable.

While the above classification of the time-asymptotic Green's function into two categories for an unstable medium is useful, it still leaves us with the daunting task of solving for $G(z, t)$ in the time-asymptotic limit. This task was considerably simplified by the "pinch-point" formalism that was originally put forth by Bers and Briggs [6, 7]. This formalism presented a convenient way to determine whether an unstable medium was absolutely unstable or convectively unstable, and, furthermore, completely determined the time-asymptotic Green's function. According to the pinch-point procedure, the time-asymptotic Green's function is completely determined by those k_0, ω_0 which satisfy:

$$D(k_0, \omega_0) = 0, \quad \frac{\partial D(k_0, \omega_0)}{\partial k} = 0 \quad (5)$$

and are "pinch points". A pinch point is determined by the analytic continuation, in the complex ω -plane, of the Laplace contour, L , towards the real ω -axis [1, 7]. As L is lowered towards the real ω -axis the corresponding Fourier contour, F , is subsequently modified to satisfy causality. This is ensured by requiring that F does not intersect any branches obtained by the mapping of the L -contour into the complex k -plane through the dispersion relation: $D(k, \omega) = 0$. This condition is violated when two branches of the L -contour in the complex k -plane coming from opposite sides of the real k -axis meet and "pinch" the Fourier contour. This defines the pinch point in the complex k -plane and it requires that the Laplace contour be deformed past the corresponding (branch) point in the complex ω -plane (satisfying $D(k, \omega) = 0$). If a pinch point exists, and the corresponding point in ω is in the upper half plane at $\omega = \omega_0$, then the medium is absolutely unstable with the time-asymptotic form of the Green's function given by:

$$\lim_{t \rightarrow \infty} G(z, t) \Big|_{z=0} \sim \frac{1}{t^{1/2}} \exp(-i\omega_0 t) \quad (6)$$

Otherwise, the medium is convectively unstable.

The time-asymptotic form of $G(z, t)$ at the origin of the laboratory coordinate system ($z = 0$) is given by Eq. (6). The spatial form of $G(z, t)$ is obtained by doing the pinch-point analysis in all possible inertial frames which are moving with respect to the laboratory frame [6, 8]. In an inertial frame moving with velocity v with respect to the laboratory frame, the Green's function is given by:

$$G(z', t') = \int_{L'} \frac{d\omega'}{2\pi} \int_{F'} \frac{dk'}{2\pi} \frac{1}{D_v(k', \omega', v)} \exp(ik'z' - i\omega't') \quad (7)$$

where the primed quantities are evaluated in the moving frame. D_v is given by:

$$D_v(k', \omega', v) = D[k(k', \omega', v), \omega(k', \omega', v)] \quad (8)$$

and the relation between the primed and the unprimed quantities is given by the Lorentz transformations:

$$\begin{aligned} z &= \gamma_v (z' + vt'), & t &= \gamma_v \left(t' + \frac{v}{c^2} z' \right), \\ k &= \gamma_v \left(k' + \frac{v}{c^2} \omega' \right), & \omega &= \gamma_v (\omega' + vk') \end{aligned} \quad (9)$$

where $\gamma_v = (1 - v^2/c^2)^{-1/2}$.

Then, as in Eq. (6), the time-asymptotic response of $G(z', t')$ at the origin of the primed coordinate system is:

$$\lim_{t' \rightarrow \infty} G(z', t') \Big|_{z'=0} \sim \frac{1}{(t')^{1/2}} \exp \{-i\omega'_0(v)t'\} \quad (10)$$

where the pinch point frequency in the primed coordinate system, $\omega'_0(v)$, is a function of the observer velocity. By using the transformation equations given in Eq. (9) it is easy to show that:

$$\lim_{t \rightarrow \infty} G(z, t) \Big|_{z=vt} \sim \left(\frac{\gamma_v}{t}\right)^{1/2} \exp\left\{-i\frac{\omega'_0(v)}{\gamma_v}t\right\} \quad (11)$$

Besides determining the spatial and temporal evolution of $G(z, t)$ in the time-asymptotic limit for an absolute instability, it is clear that this procedure also determines the spatial and temporal evolution of a convective instability.

Thus, from the pinch-point analysis the following properties of an unstable medium can be determined:

- (a) the absolute versus convective nature of the unstable medium;
- (b) the space-time evolution (i.e. the spatial and temporal growth rates) of a localized (at $z = 0$) noise source from an initial time to a time where the transient response of the system to the initial perturbations can be ignored;
- (c) the velocity of propagation of the instability in the medium.

This last point is very important. In general, the velocity of propagation is not related to a group velocity of any mode satisfying the dispersion relation $D(k, \omega) = 0$. In particular, for an absolutely unstable medium the concept of a group velocity cannot be defined. Thus, ray-tracing in an absolutely unstable medium is meaningless.

It is important to note that the Green's function describes the natural responses of an infinitely extended medium. In contrast to responses in a bounded medium, this must entail that there be no (initial) excitations at infinity or, that, at infinity, the initial excitations decay faster than the space-time normal modes. If, at infinity, the initial conditions do not decay faster than the the space-time normal modes, it is meaningless to describe or distinguish the space-time evolution of these initial conditions in terms of the inherent properties of absolute and convective instabilities in that medium. By not paying attention to these mathematical details one can make misguided and misleading statements about the theory of absolute and convective instabilities [9].

III. SPACE-TIME EVOLUTION OF CYCLOTRON MASER TYPE OF INSTABILITIES

The cyclotron maser instability driven by a loss-cone distribution is believed to be a favorable explanation for the auroral kilometric radiation [2, 3], the Jovian decametric emission and similar emissions from Saturn and Uranus, certain types of continuum solar microwave bursts, and microwave emission from some flare stars [10]. In this section we consider a highly anisotropic, ring-like, electron distribution function in a uniform, background magnetic field and study the space-time evolution of instabilities propagating along the magnetic field [11-13]. Furthermore, we will use the pinch-point analysis to determine important characteristics that will help distinguish absolute instabilities from convective instabilities.

The electron distribution function is assumed to be of the form:

$$f_0(p_\perp, p_\parallel) = \frac{1}{2\pi p_{0\perp}} \delta(p_\perp - p_{0\perp}) \delta(p_\parallel - p_{0\parallel}) \quad (12)$$

in a homogeneous magnetic field, \vec{B}_0 . Here p_\perp and p_\parallel are the magnitude of the perpendicular (to \vec{B}_0) and parallel components of the momentum, respectively, and \vec{p}_0 is a constant momentum. Assuming the ions to be forming a cold, neutralizing background, the relativistic Vlasov equation leads to the following dispersion relation for right-handed circularly polarized electromagnetic waves propagating along \vec{B}_0 :

$$D(k, \omega) = (c^2 k^2 - \omega^2) \left\{ (\omega - kv_\parallel - \omega_c)^2 + \frac{1}{2} \frac{v_\perp^2}{c^2} \omega_p^2 \right\} + \omega_p^2 (\omega - kv_\parallel) (\omega - kv_\parallel - \omega_c) \quad (13)$$

where

$$v_\perp = \frac{p_{0\perp}}{\gamma_0 m_e}, \quad v_\parallel = \frac{p_{0\parallel}}{\gamma_0 m_e}, \quad \gamma_0 = \sqrt{1 + \frac{p_0^2}{m_e^2 c^2}}, \quad \omega_p = \frac{\omega_{p0}}{\sqrt{\gamma_0}}, \quad \omega_c = \frac{\omega_{c0}}{\gamma_0}$$

m_e is the electron rest mass, and ω_{p0} and ω_{c0} are the electron plasma and electron cyclotron frequencies, respectively, corresponding to the rest mass of the electrons. For $\omega_{p0}/\omega_{c0} = 0.2$, $v_\parallel = 0$ and $v_\perp = 0.2c$, the roots of the dispersion relation (real and imaginary parts of ω) are plotted in Fig. 1 as a function of real k . There are three branches of $D(k, \omega)$ corresponding to the whistler mode (whose phase velocity is less than the speed of light), an electromagnetic mode (whose phase velocity is greater than the speed of light) and a negative energy mode. The coupling of the

negative energy mode to the whistler mode or the electromagnetic mode leads to the whistler instability or the relativistic instability, respectively.

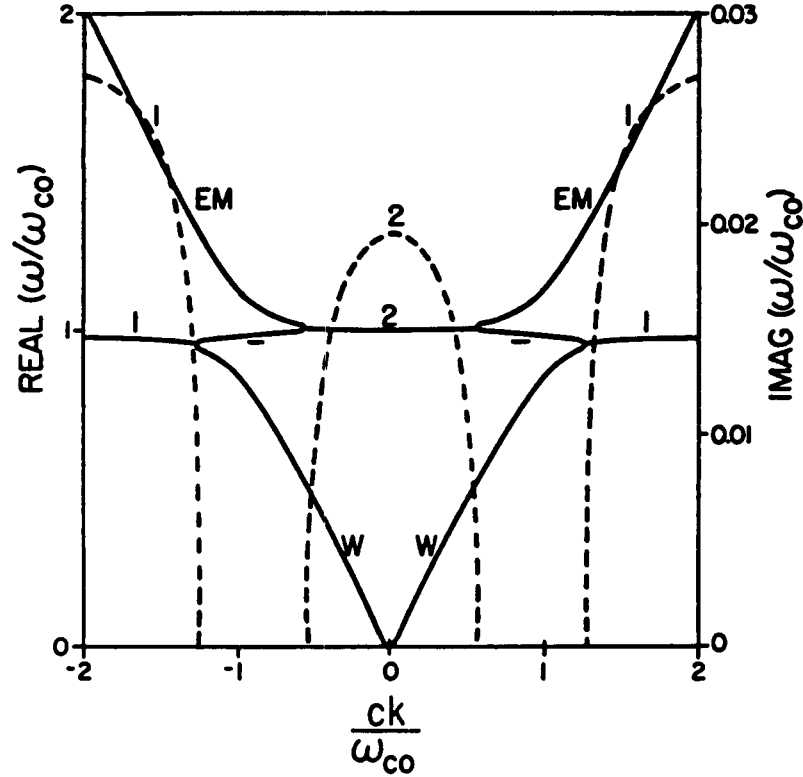


Figure 1. Real (solid line) and imaginary (dashed line) parts of the normalized frequency versus real, normalized wavenumbers. These are the roots of the dispersion function given in Eq. (13) for $\omega_{p0}/\omega_{c0} = 0.2$, $v_{\parallel} = 0$, and $v_{\perp} = 0.2c$. W is the whistler branch, EM is the electromagnetic branch, $-$ indicates the negative energy branch, 1 corresponds to the whistler instability and 2 to the relativistic instability.

For the parameters indicated above the pinch-point analysis in the laboratory frame shows that there are three pinch points with two of them corresponding to the whistler instability and one to the relativistic instability. The pinch points of the whistler instability are at $k_0 = \pm\infty$ and $\omega_0/\omega_{c0} \approx 0.98 + 0.028i$, while the pinch point of the relativistic instability is at $k_0 = 0$ and $\omega_0/\omega_{c0} \approx 0.999 + 0.02i$. Thus, the whistler and the relativistic instabilities are absolute instabilities with the whistler instability having a higher growth rate. The time-asymptotic form of the Green's function is determined by doing the pinch point analysis in all the iner-

tial frames moving with different velocities with respect to the laboratory frame. From Eq. (11):

$$\lim_{t \rightarrow \infty} \left| \ln \{G(z, t)\} \right|_{z=vt} \sim \frac{\omega'_{oi}(v)}{\gamma_v} t \quad (14)$$

where ω'_{oi} is the imaginary part of ω'_o . Here we have neglected the $\ln(t)$ term for large t . In Fig. 2 we have plotted the "pulse shape", i.e. $\omega'_{oi}(v)/\gamma_v$ as function of the observer velocity v . Since, in Fig. 2, the product of the abscissa with t gives z , and the product of the ordinate with t gives the right-hand side of Eq. (14), Fig. 2 gives the time-asymptotic, self-similar evolution of the magnitude of the logarithm of the Green's function.

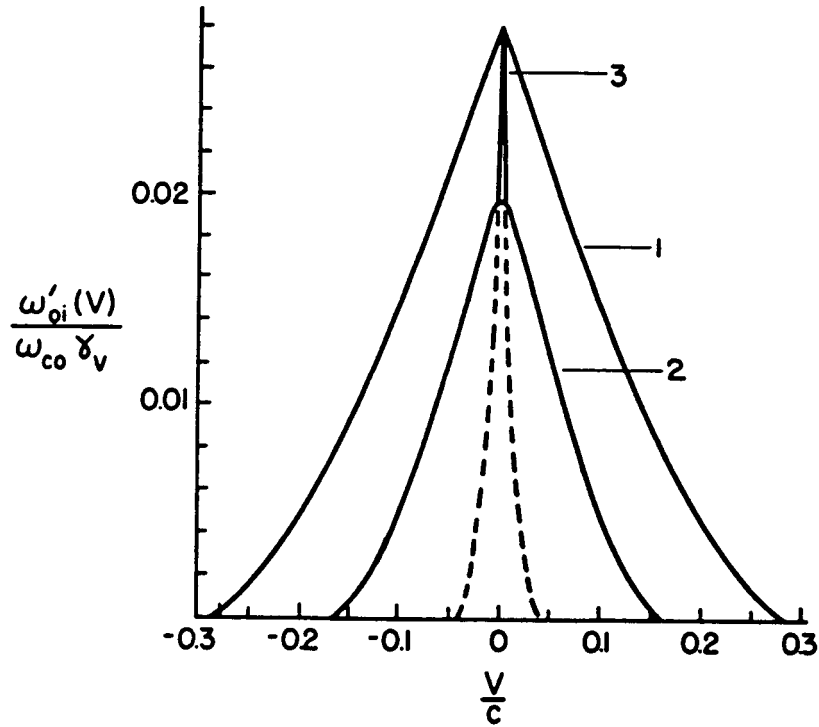


Figure 2. The appropriately normalized pulse shapes for the whistler (1,3) and the relativistic (2) instabilities. The parameters are the same as for Fig. 1. The dashed line indicates that the pinch point corresponding to 3 has been dissolved by 2. The pulse shapes for 1 and 2 are those of an absolute instability.

The two pinch points for the whistler waves (labeled 1 and 3 in Fig. 2), which have the same frequency at $v = 0$ (i.e. in the laboratory frame), become degenerate for $v \neq 0$. However, when $|v| \approx 0.005$, the whistler pinch point (3) interacts with the relativistic pinch point (labeled 2). Here,

the whistler pinch point (3) is "dissolved" [1] by the relativistic pinch point (2). Thereafter, for $|v| \gtrsim 0.005$, only the pinch points corresponding to the whistler instability (1) and the relativistic instability survive. In the rest of the discussion we shall consider only these two pinch points. From Fig. 2 the absolute nature of the two instabilities is quite clear.

The whistler instability, while it has a larger growth rate than the relativistic instability, can be stabilized by thermal spreading of the ring distribution [12, 13]. The relativistic instability is not affected by thermal effects as its phase velocity is greater than the speed of light. So, instead of studying just the whistler instability, we shall also determine the behavior of the relativistic instability.

In Eq. (11), the dominant variation of the Green's function in space and time is given by the exponential. The factor multiplying the exponential varies slowly with space and time. By neglecting this factor, the real part of the time-asymptotic Green's function is given by:

$$\Gamma(z, t) = \cos \left[\frac{1}{\gamma_v} \omega'_{or}(z/t)t \right] \exp \left[\frac{1}{\gamma_v} \omega'_{oi}(z/t)t \right] \quad (15)$$

where, now, $\gamma_v = [1 - (z/ct)^2]^{-1/2}$, and ω'_{or} is the real part of ω'_o . For an observer at a fixed point $z = z_o$, with $|z_o| > 0$, $\Gamma(z_o, t)$ gives the temporal history of an instability which has evolved from a broadband noise source located at $z = 0$ at time $t = 0$.

By the very nature of an absolute instability, $\Gamma(z_o, t)$ will continue to grow in time for all times. In Figs. 3a and 3b we have plotted the frequency spectrum of $\Gamma(z_o, t)$, i.e. $|\Gamma(z_o, \omega)|$, for the whistler and relativistic instabilities, respectively. The power spectrum is very narrow-band for both instabilities and the peak of the spectrum occurs near the laboratory pinch point frequency, $\omega'_{or}(v = 0)$. Thus, to an observer in the unstable medium, the two absolute instabilities would correspond to very narrow frequency spectra.

As $v_{o||}$ is increased, the maximum of the pulse shape occurs at an observer velocity $v = v_{o||}$. For the same parameters as indicated above, the two instabilities become convective when $v_{o||} \gtrsim 0.18c$. In order to illustrate the effect of relativity, and the characteristics of convective instabilities, we consider the case where $v_{o||} = 0.85c$. The corresponding pulse shape is plotted in Fig. 4. Again, there are two pinch points corresponding to the whistler instability (labeled 1 and 3) and one pinch point for the relativistic instability (labeled 3). Pinch point 3 is dissolved by the relativistic instability and we are left with two pinch points (1 and 2). The pulse shape is highly asymmetric as compared to the pulse shape in Fig. 2. This asymmetry is due to the relativistic effects. It is clearly evident that the two instabilities are convective.

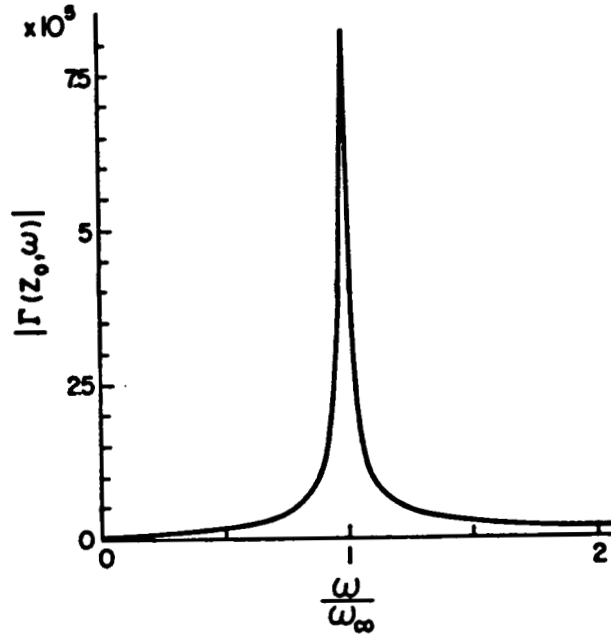


Figure 3a. The frequency spectrum of $\Gamma(z_0, t)$, with $z_0\omega_{c0}/c = 50$, for the whistler instability (labeled 1 in Fig. 2).

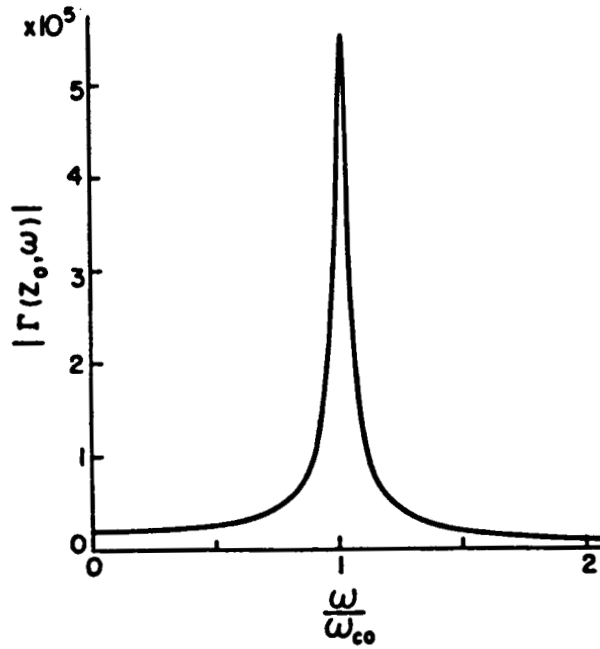


Figure 3b. The frequency spectrum of $\Gamma(z_0, t)$, with $z_0\omega_{c0}/c = 50$, for the relativistic instability (labeled 2 in Fig. 2).

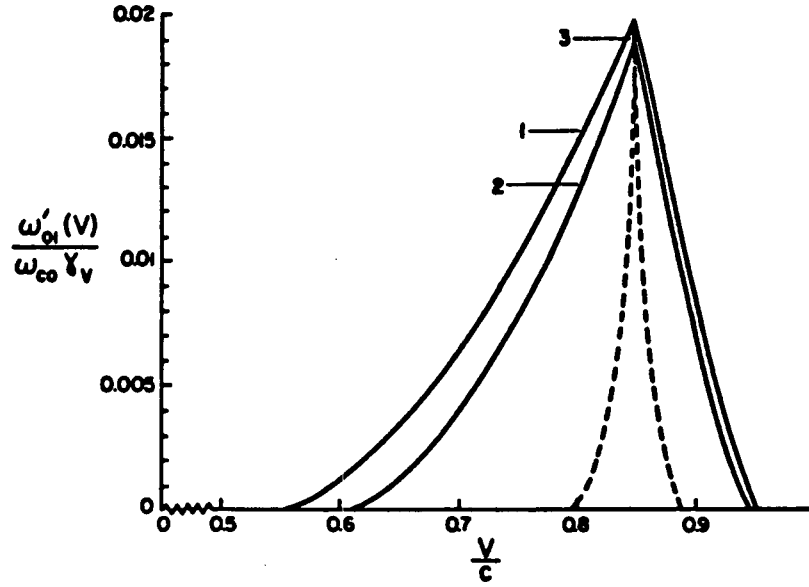


Figure 4. The appropriately normalized pulse shapes for the whistler (1,3) and the relativistic (2) instabilities. The parameters are the same as for Fig. 1 except that $v_1 = 0.85c$. Again, the pinch point corresponding to 3 has been dissolved by 2. The pulse shapes for 1 and 2 are those of a convective instability.

In order to calculate $\Gamma(z_0, t)$, the convective nature of the instabilities requires that the observer be at $z = z_0 > 0$. Furthermore, in contrast to an absolute instability where an observer sees a continuous growth of the signal, for the convective instability an observer will observe the instability for a finite amount of time. This is the case as shown in Figs. 5a and 5b for the whistler and the relativistic instabilities, respectively. The wave packet nature of the convective instability is obvious from these figures.

The power spectrum of the signal in Figs. 5a and 5b is plotted in Figs. 6a and 6b, respectively. The relative broadband nature of the spectrum, as compared to the case when the whistler and relativistic instabilities were absolute, is clearly evident. The power is spread out to harmonics of the electron cyclotron frequency.

Thus, there is a distinct observational difference between absolute and convective instabilities. The emission corresponding to an absolute instability will have a narrow frequency spectrum while a convective instability will correspond to a broadband emission.

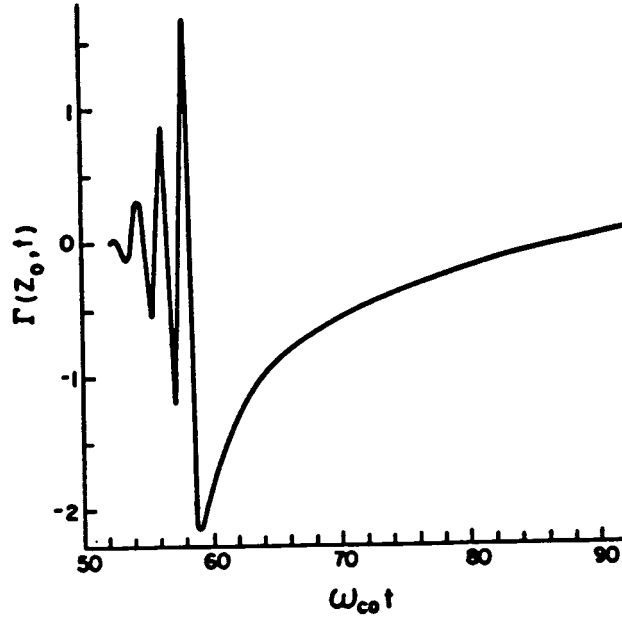


Figure 5a. $\Gamma(z_0, t)$, with $z_0 \omega_{c0}/c = 50$, as a function of the normalized time for the whistler instability (1 in Fig. 4).

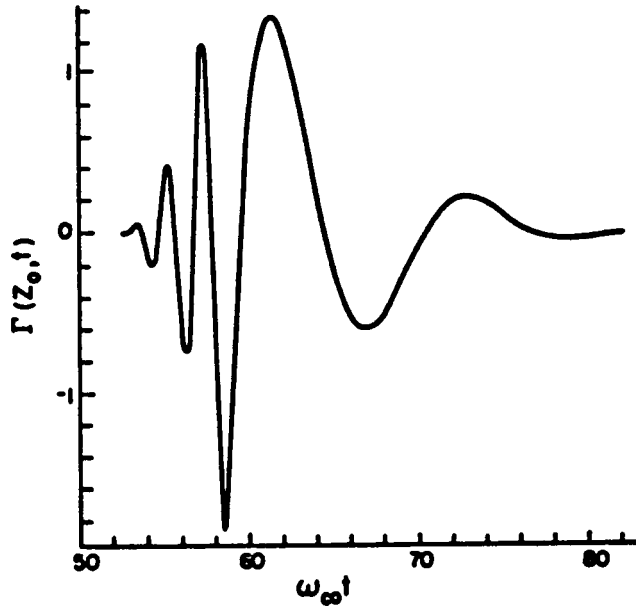


Figure 5b. $\Gamma(z_0, t)$, with $z_0 \omega_{c0}/c = 50$, as a function of the normalized time for the relativistic instability (2 in Fig. 4).

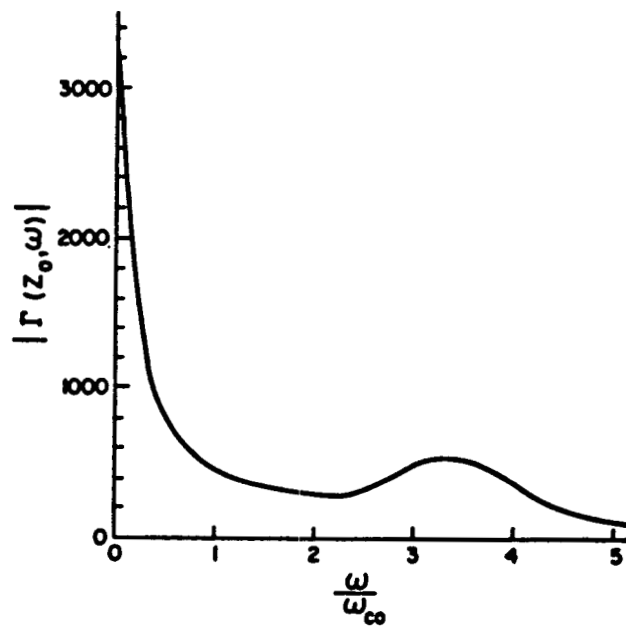


Figure 6a. Frequency spectrum of the $\Gamma(z_0, t)$ shown in Fig. 5a.

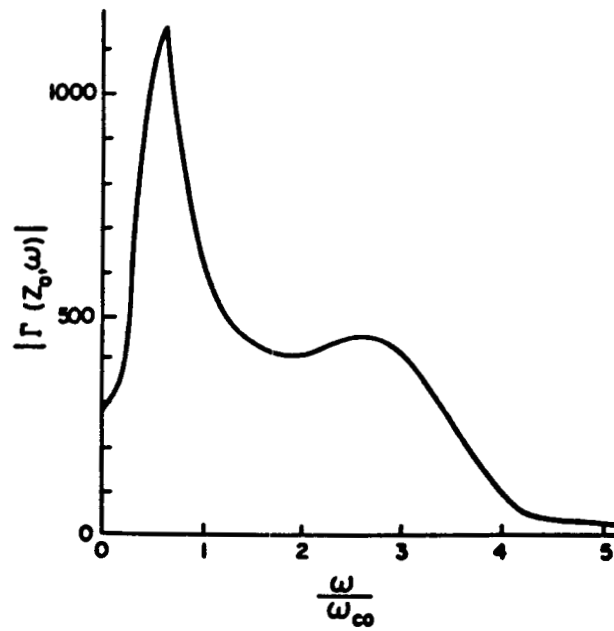


Figure 6b. Frequency spectrum of the $\Gamma(z_0, t)$ shown in Fig. 5b.

We have also done a pinch-point analysis for electromagnetic instabilities propagating across \vec{B}_0 that are generated by a ring distribution function of electrons. We have studied those instabilities whose phase velocities are greater than the speed of light and, thus, are not affected by cyclotron resonance damping. Furthermore, we have restricted ourselves to the case of $\omega_{p0}/\omega_{c0} \ll 1$ (which is an appropriate limit for the conditions that exist in the source regions of the auroral kilometric radiation). Instabilities are generated near the electron cyclotron frequency and its harmonics. We observe an interesting space-time behavior of these instabilities as a function of ω_{p0}/ω_{c0} . For very small densities ($\omega_{p0}/\omega_{c0} \approx 0.05$ with $v_{\parallel} = 0$ and $v_{\perp} = 0.1c$) the instability near the fundamental electron cyclotron frequency is an absolute instability while the instabilities at the harmonics are convective instabilities. As ω_{p0} is increased the instability at the second harmonic also becomes an absolute instability. For further increases in ω_{p0} ($\omega_{p0}/\omega_{c0} \approx 0.25$) the instability at the fundamental cyclotron frequency becomes convective while the instability at the second harmonic remains as an absolute instability. Hence, we have harmonic generation from a completely linear theory. These results should be important in explaining the observed emission at harmonics of the electron cyclotron frequencies in the auroral regions [14]. Details of all the results on the propagation of instabilities across the magnetic field will be published elsewhere.

CONCLUSIONS

A pinch-point, Green's function analysis of electron cyclotron maser instabilities has been shown to yield observationally interesting features about the space-time propagation of such instabilities. An absolute instability is found to have a narrow-band frequency spectrum while a convective instability has a broadband frequency spectrum. This feature should be important in correlating experimental observations with theoretical models.

Although, no mention has been made of the nonlinear saturation mechanisms for these instabilities, it is evident from some previous results [1] that the nonlinearly saturated state of an absolute instability is very different from that of a convective instability. In general, observed emissions are from nonlinearly saturated states of instabilities that have evolved in either an absolute or a convective manner in their linear stage. These nonlinear states can be expected to carry signatures of whether, linearly, the instability was of an absolute type or a convective type. This aspect needs to be accounted for when modeling experimental observations.

ACKNOWLEDGEMENTS

This work was supported by NASA Grant No. NAGW-2048.

REFERENCES

- [1] A. Bers, *Handbook of Plasma Physics*, Vol. 1, M. N. Rosenbluth, and R. Z. Sagdeev, eds. (North-Holland, Amsterdam 1983), Chap. 3.2.
- [2] D. B. Melrose, *Astrophys. J.* **207**, 651 (1976).
- [3] C. S. Wu and L. C. Lee, *Astrophys. J.* **230**, 621 (1979).
- [4] P. M. Morse and H. Feshbach, *Methods of Theoretical Physics* (McGraw-Hill, New York 1953).
- [5] L. D. Landau and I. M. Lifshitz, *Electrodynamics of Continuous Media* (in Russian, GITTL, Moscow 1953); see also their *Fluid Mechanics* (Pergamon Press, London 1959).
- [6] See Ref. [1] above and references therein.
- [7] R. J. Briggs, *Electron-Stream Interaction with Plasmas* (MIT Press, Cambridge, MA 1964).
- [8] A. Bers, A. K. Ram, and G. Francis, *Phys. Rev. Lett.* **53**, 1457 (1984).
- [9] T. E. Oscarsson and K. G. Rönmark, *Geophys. Res. Lett.* **13**, 1384 (1986). A detailed discussion of the misconceptions in this paper will be presented in a forthcoming publication.
- [10] C. S. Wu, *Space Sci. Revs.* **41**, 215 (1985) and references therein.
- [11] V. V. Zhelezniakov, *Izv. Vys. Voch. Zaved. Radiofiz.* **2**, 14 (1959).
- [12] A. Bers, J. K. Hoag, and E. A. Robertson, *Quart. Prog. Reports* No. 77, pp. 149-152; No. 78, pp. 105-110; No. 79, pp. 107-112, *Res. Lab. of Electronics*, MIT, Cambridge, MA (1965).
- [13] A. K. Ram, G. Francis, and A. Bers, *Proceedings of the Fourth International Workshop on Electron Cyclotron Emission and Electron Cyclotron Resonance Heating* (Ufficio Edizioni Scientifiche, Frascati, Rome, Italy 1984); and M.I.T. Plasma Fusion Center Report PFC/CP-84-5, Cambridge, MA (1984).
- [14] R. F. Benson, *J. Geophys. Res.* **90**, 2753 (1985).

APPENDIX B

Space-Time Analysis of Electromagnetic Instabilities With Application to Auroral Kilometric Radiation*

A K Ram and A Bers (Both at: Plasma Fusion Center, MIT,
Cambridge, MA 02139; 617-253-2595) (Sponsor: T Chang)

We present results on the space-time evolution of electromagnetic instabilities in plasmas with anisotropic velocity distributions in a magnetic field. The space-time analysis classifies the propagation of instabilities into one of only two possible categories – absolute or convective.¹ Associated with each category are distinct observable features: an absolute instability has a narrow frequency bandwidth while a convective instability typically has a broad band emission; the propagation and nonlinear saturation of these instabilities are also very different. The instabilities considered are those that propagate either along the magnetic field or across the magnetic field, and are generated by relativistic, highly anisotropic, electron distribution functions. Such distribution functions arise in the auroral regions and are considered to be sources of the observed auroral kilometric radiation.² For instabilities propagating across the magnetic field we consider both the ordinary and the extraordinary (x) modes. The instabilities are generated at the electron cyclotron frequency (ω_{ce}) and its harmonics. For low electron densities, the x-mode is an absolute instability at ω_{ce} and a convective instability at the harmonics. As the density is increased the instability at ω_{ce} becomes convective while that at $2\omega_{ce}$ becomes absolute, thereby, leading to harmonic generation of radiation by a linear mechanism.

*Work supported by NASA Grant No. NAGW-2048.

¹A. Bers in *Handbook of Plasma Physics*, Gen. Eds. M. W. Rosenbluth and R. Z. Sagdeev, North-Holland Publishing Company (1983); A. Bers, A. K. Ram and G. Francis, *Phys. Rev. Lett.* **53**, 1457 (1984).

²C. S. Wu and L. C. Lee, *Astrophys. J.* **230**, 621 (1979).

1. 1990 Fall Meeting
2. 000004341
3. (a) A K Ram
Room 38-256
MIT
Cambridge, MA 02139
(b) 617-253-2595
4. SM
5. (a)
(b) 2704 Auroral Phenomena
2772 Plasma Waves and
Instabilities
- 6.
7. 20% at the 1990 Cambridge
Workshop on Theoretical
Geoplasma Physics, MIT
8. \$50.00 check enclosed
9. C
- 10.
11. No

SPACE-TIME ANALYSIS OF
ELECTROMAGNETIC INSTABILITIES
WITH APPLICATION TO
AURORAL KILOMETRIC RADIATION

ABHAY RAM & ABRAHAM BERS

PLASMA FUSION CENTER
M.I.T.

AGU MEETING
DECEMBER 4, 1990

- PROPAGATION OF A SMALL AMPLITUDE (LINEAR REGIME) UNSTABLE PERTURBATION (GROWING FROM A LOCALIZED, BROAD-BAND NOISE SPECTRA) IN A HOMOGENEOUS PLASMA IS GIVEN BY:

$$G(\vec{r}, t) = \int_L \frac{d\omega}{2\pi} \int_F \frac{d^3k}{(2\pi)^3} \frac{e^{i\vec{k} \cdot \vec{r} - i\omega t}}{D(\vec{k}, \omega)}$$

(RESPONSE TO A NOISE FUNCTION OF THE FORM: $\delta(\vec{r})\delta(t)$)

- TIME ASYMPTOTIC PROPERTIES OF $G(\vec{r}, t)$ ARE DETERMINED BY "PINCH POINTS" (\vec{k}_0, ω_0) :
(REF.: BERS 1983 ; BRIGGS 1964)

$$D(\vec{k}_0, \omega_0) = 0$$

$$\frac{\partial D}{\partial \vec{k}}(\vec{k}_0, \omega_0) = 0$$

AND ARE "PINCHES" FORMED BY THE DEFORMATION OF THE L-CONTOUR

- PINCH POINTS ARE SPECIAL TYPE OF SADDLE POINTS IN THE SIX-DIMENSIONAL COMPLEX - \vec{k} SPACE

- $\lim_{t \rightarrow \infty} G(\vec{r}=0, t) \rightarrow \frac{1}{t^{3/2}} e^{-i\omega_0 t}$

ω is the pinch point frequency.

- IN THE TIME ASYMPTOTIC LIMIT, THE SPATIAL PROFILE OF $G(\vec{r}, t)$ IS OBTAINED BY LORENTZ TRANSFORMING TO INERTIAL FRAMES MOVING WITH RESPECT TO THE LABORATORY FRAME AND DETERMINING THE PINCH-POINTS IN EACH OF THESE FRAMES

- $\lim_{t \rightarrow \infty} G(\vec{r}, t) \rightarrow \left(\frac{\gamma_v}{t}\right)^{3/2} \exp\left\{-i \frac{\omega'_0(\vec{v})}{\gamma_v} t\right\}$

$$\vec{V} \equiv \text{OBSERVER VELOCITY} = \frac{\vec{r}}{t}$$

$$\gamma_v = \frac{1}{\sqrt{1 - v^2/c^2}}$$

• THE PINCH-POINT ANALYSIS DETERMINES :

* ABSOLUTE VERSUS CONVECTIVE
NATURE OF THE INSTABILITY

* GROWTH RATE OF THE INSTABILITY

* VELOCITY OF PROPAGATION OF THE
INSTABILITY

(NOT, IN GENERAL, RELATED TO ANY
GROUP VELOCITY)

(RAY TRACING CANNOT BE DONE IN
AN ABSOLUTELY UNSTABLE MEDIUM)

* IDENTIFIABLE CHARACTERISTICS WHICH
CAN BE DIRECTLY CORRELATED WITH
MEASUREMENTS

NOT ONLY $\vec{E}-\vec{B}$ FIELD POLARIZATIONS
BUT ALSO THE SPECTRUM AND
BANDWIDTH OF THE UNSTABLE
RADIATION

ELECTRON - CYCLOTRON MASER

TYPE OF INSTABILITIES

(REF.: WU & LEE 1979 , MELROSE 1976)

- PLASMA IN AN UNIFORM MAGNETIC FIELD (\vec{B}_0)

- $$f_{oe}(p_{\perp}, p_{\parallel}) = \frac{1}{2\pi p_{0\perp}} \delta(p_{\perp} - p_{0\perp}) \delta(p_{\parallel} - p_{0\parallel})$$

-- electron distribution function (the ion dynamics is ignored)

- RIGHT HAND CIRCULARLY POLARIZED RADIATION PROPAGATING ALONG \vec{B}_0 (1-D)

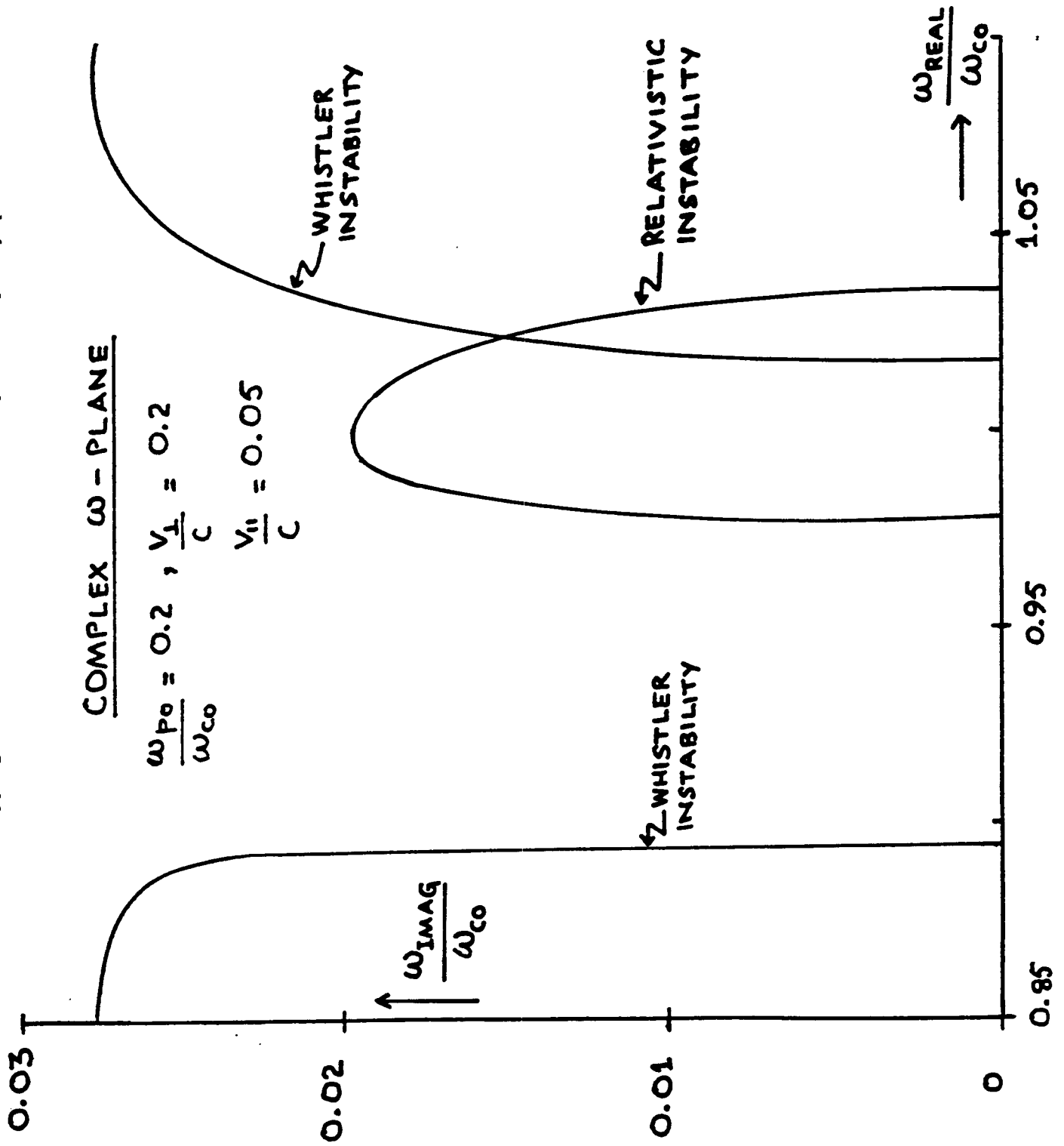
- $$\frac{c^2 k^2}{\omega^2} = 1 - \frac{\omega_{pe}^2}{\omega^2} \left[\frac{\omega - k v_{\parallel}}{\omega - k v_{\parallel} - \omega_{ce}} + \frac{v_{\perp}^2}{2c^2} \frac{c^2 k^2 - \omega^2}{(\omega - k v_{\parallel} - \omega_{ce})^2} \right]$$

$$v_{\parallel} = \frac{p_{0\parallel}}{m_e}, \quad v_{\perp} = \frac{p_{0\perp}}{m_e}, \quad \gamma_0 = \left(1 + \frac{v_{\parallel}^2}{c^2} + \frac{v_{\perp}^2}{c^2} \right)^{-1/2}$$

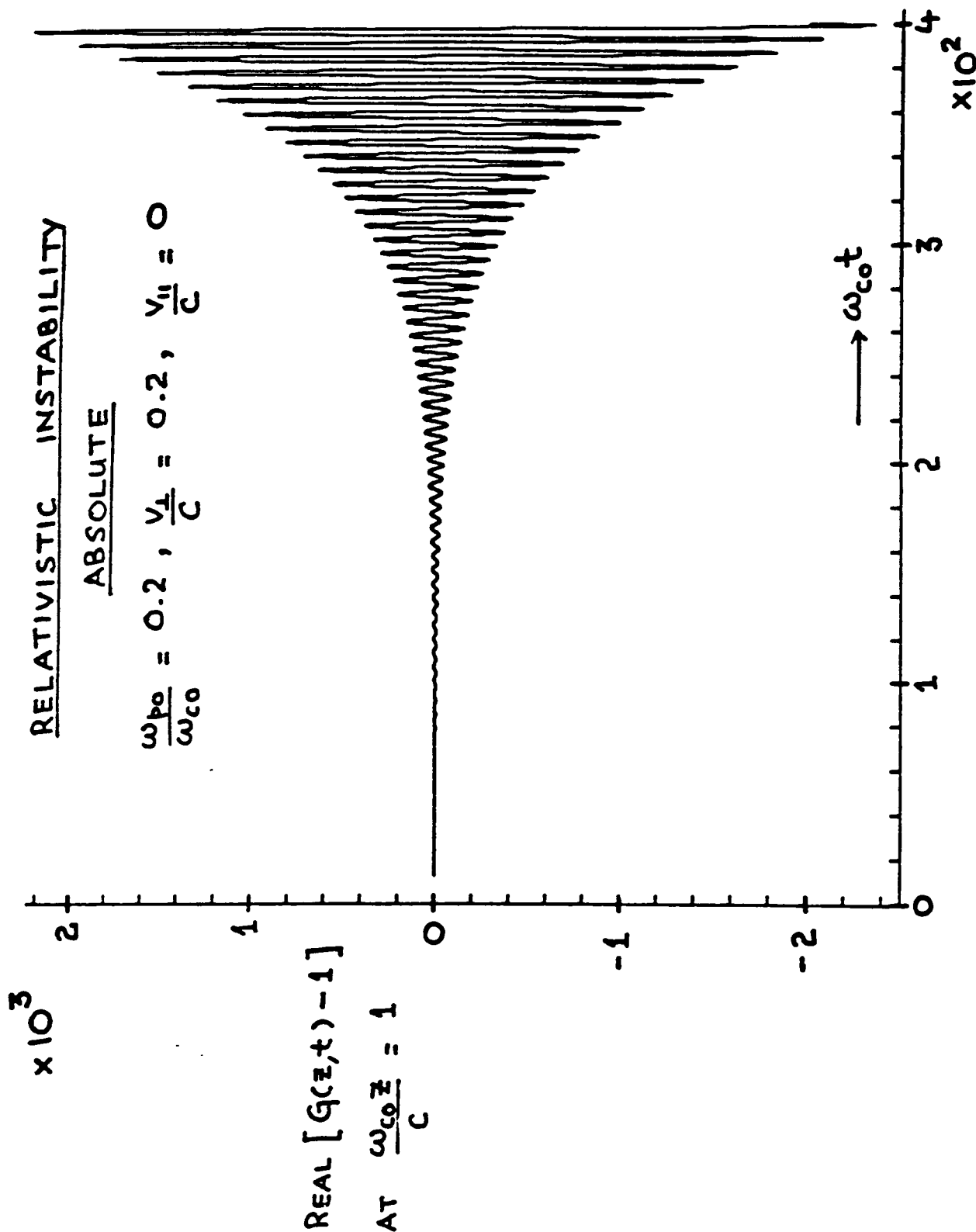
$m_e \equiv$ ELECTRON REST MASS

$$\omega_{pe}^2 = \frac{4\pi n_0 e^2}{\gamma_0 m_e}, \quad \omega_{ce} = \frac{e B_0}{\gamma_0 m_e c}$$

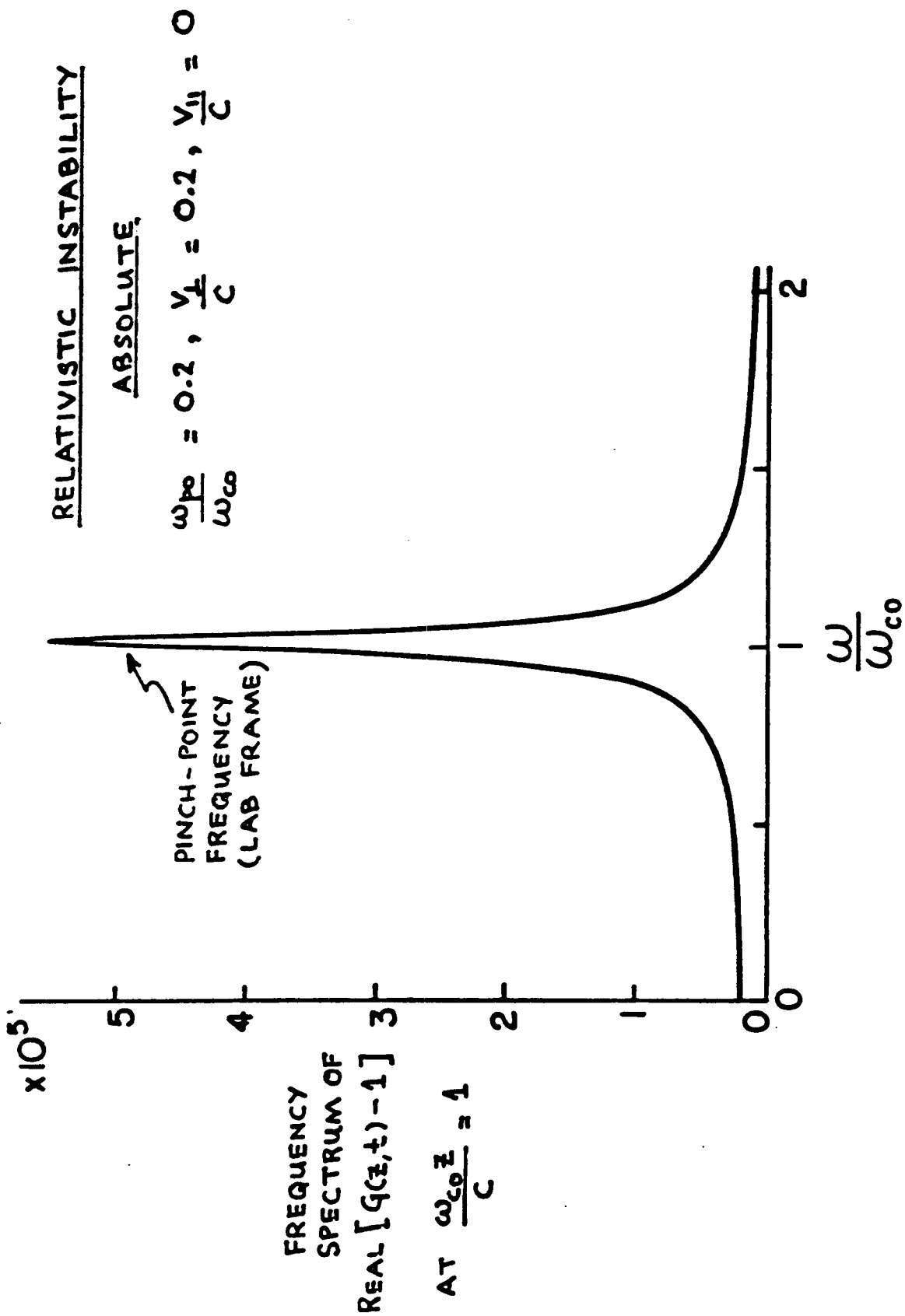
mapping the real k-axis into the complex frequency plane



Green's function response observed at a given position as a function of the normalized time (this is the case when the relativistic instability is an absolute instability)



This is the Fourier transform of the signal given on the previous page

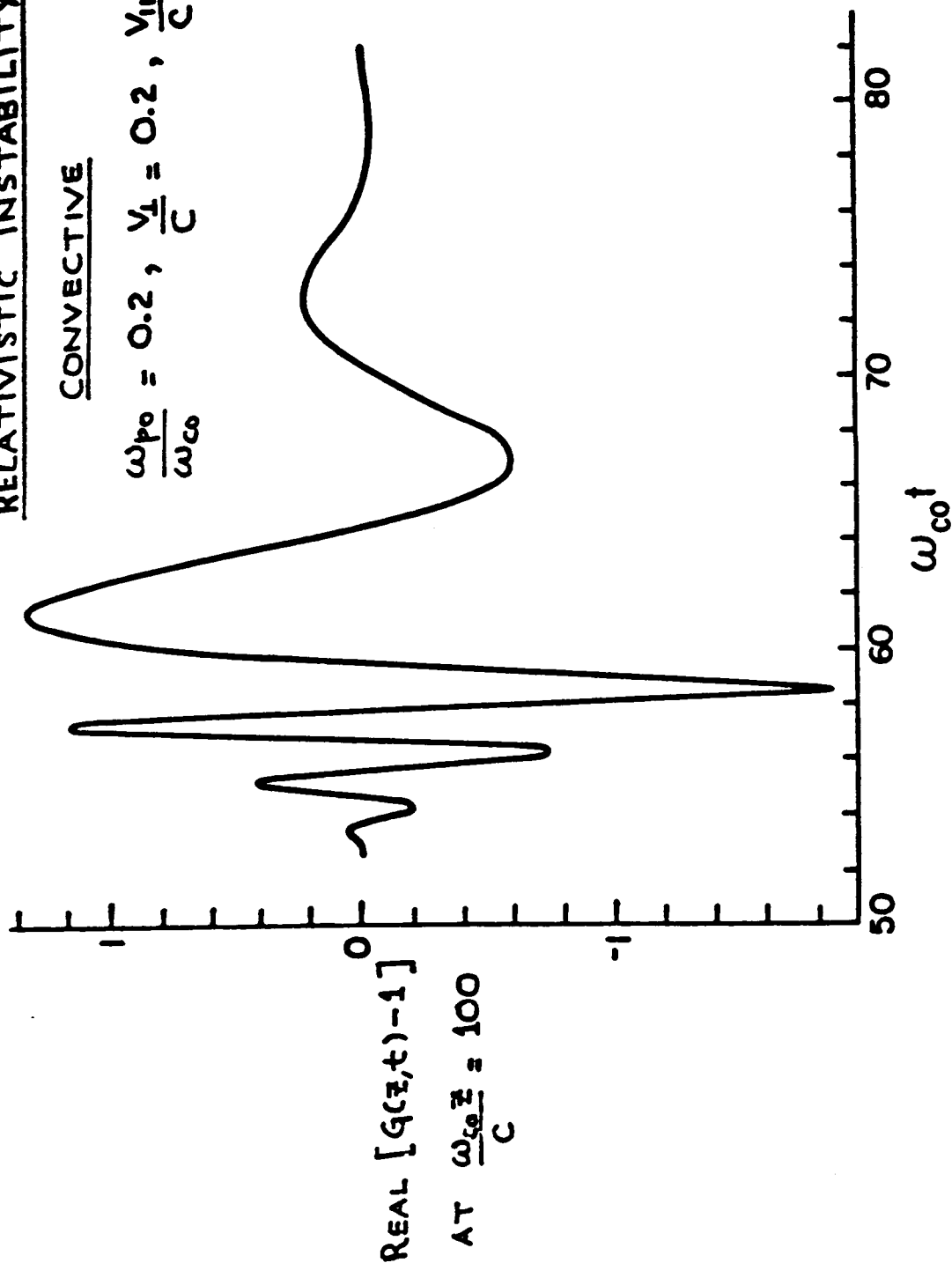


Green's function response observed at a given position as a function of the normalized time (this is the case when the relativistic instability is a convective instability)

RELATIVISTIC INSTABILITY

CONVECTIVE

$$\frac{\omega_{p0}}{\omega_{c0}} = 0.2, \quad \frac{v_1}{c} = 0.2, \quad \frac{v_{II}}{c} = 0.85$$



This is a Fourier transform of the signal on the previous page.

RELATIVISTIC INSTABILITY

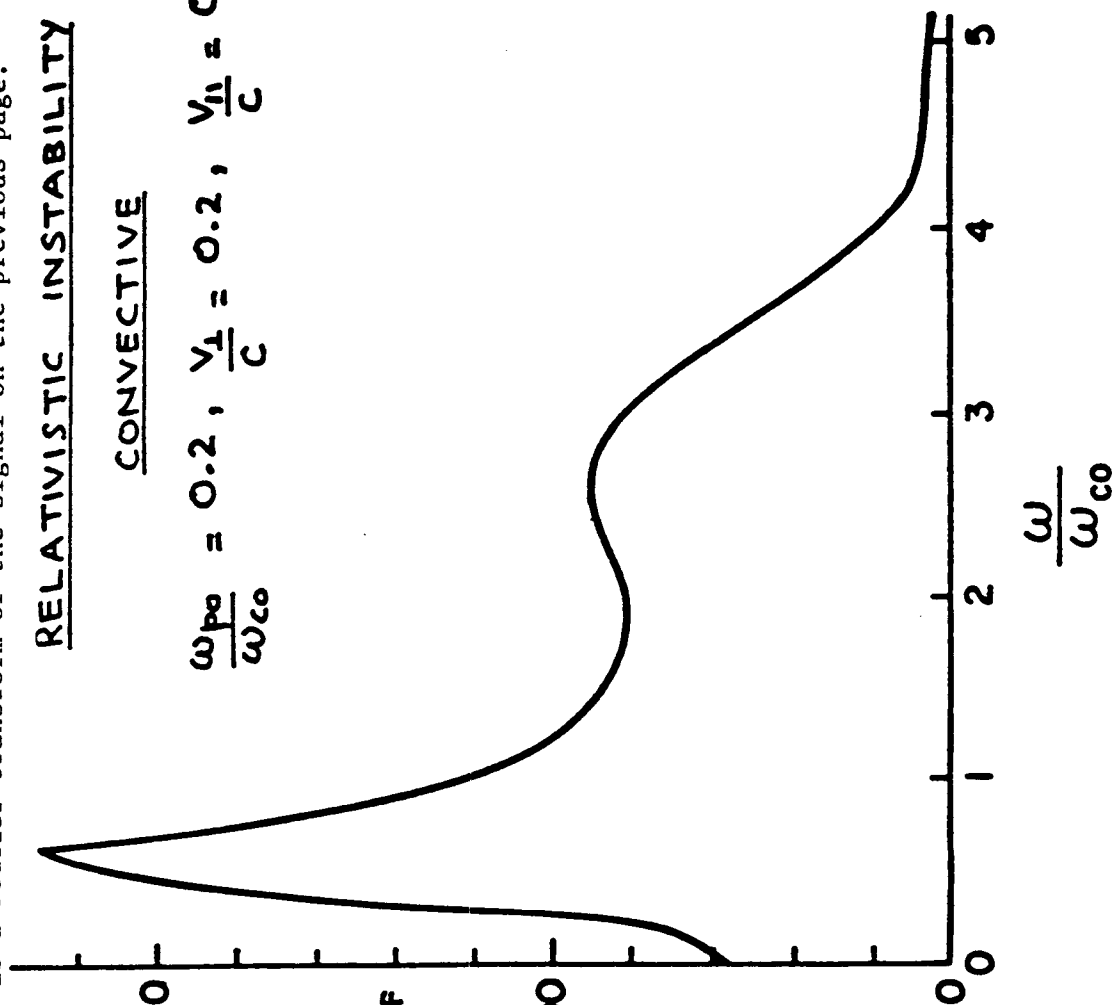
CONVECTIVE

$$\frac{\omega_{pe}}{\omega_{ce}} = 0.2, \quad \frac{v_1}{c} = 0.2, \quad \frac{v_{th}}{c} = 0.85$$

FREQUENCY
SPECTRUM OF

$\text{REAL} [g(z,t) - 1]$

AT $\frac{\omega_{ce} z}{c} = 100 \quad 500$



CONCLUSIONS

- SPACE-TIME ANALYSIS OF THE PROPAGATION OF INSTABILITIES GIVES INTERESTING AND OBSERVATIONALLY IMPORTANT FEATURES (CAN BE USED TO CHECK THEORIES)
- THE PULSE RESPONSE OF AN ABSOLUTELY UNSTABLE MEDIUM WILL HAVE A NARROW BAND EMISSION ASSOCIATED WITH IT (PINCH-POINT FREQUENCY IN THE LAB FRAME)
- THE PULSE RESPONSE OF A CONVECTIVELY UNSTABLE MEDIUM WILL HAVE A BROAD BAND EMISSION ASSOCIATED WITH IT (SPECTRA CAN EXTEND TO HARMONICS)
- THE SPECTRA OF EMISSION IS NOT GIVEN BY $\text{REAL}(\omega)$ WITH $\text{IMAGINARY}(\omega) > 0$ for some real- k .

COMMENTS ON ABSOLUTE AND CONVECTIVE INSTABILITIES

A. K. Ram and A. Bers

Plasma Fusion Center and Research Laboratory of Electronics, Massachusetts Institute of Technology

Abstract. We point out the misconceptions in the arguments put forth by Oscarsson and Rönnmark [1986] that question the validity and usefulness of the well-known theory of absolute and convective instabilities. The solid basis of the well-known theory is clarified.

Introduction

Absolute or convective evolutions of instabilities can produce very different signatures of observed radiation from unstable plasmas. This is particularly useful in space plasmas when correlating experimentally observed emissions with theoretical models describing the source regions [Ram and Bers, 1991]. A letter [Oscarsson and Rönnmark, 1986] has questioned the basis and usefulness of the theory of absolute and convective instabilities by using some singular examples. The arguments put forth by these authors, based upon their singular examples, are misleading. Furthermore, the notion of a time-asymptotic limit is treated in an imprecise manner by these authors.

The theory of absolute and convective instabilities [Briggs, 1964; Bers, 1983] describes the linear evolution of instabilities from an initially localized source in an infinitely homogeneous medium. In this paper we clarify the conditions for the validity of the theory of absolute and convective instabilities, and, furthermore, show that the examples discussed in the aforementioned letter are not generic for continuous media and do not invalidate the theory of absolute and convective instabilities.

In what follows, we shall consider the case of evolution of instabilities in time and in one spatial dimension. The generalization to higher spatial dimensions is more complicated but can be carried out in a straightforward manner.

Space-Time Evolution of Instabilities

The theory of absolute and convective instabilities is based on a Green's function analysis of equations describing the space-time dynamics of a small-amplitude perturbation in a spatially homogeneous and a time-invariant medium. The equation for the Green's function, $G(z, t)$, is given by:

$$\tilde{L} G(z, t) = \delta(z) \delta(t) \quad (1)$$

where \tilde{L} is, in general, a linear integro-partial-differential operator with constant coefficients. Using complex Fourier-Laplace transforms, the solution to (1) can be

written as:

$$G(z, t) = \int_L \frac{d\omega}{2\pi} \int_F \frac{dk}{2\pi} \frac{1}{D(k, \omega)} \exp(ikz - i\omega t) \quad (2)$$

where $D(k, \omega)$ is the dispersion function for the system – directly related to the transforms of \tilde{L} , and L and F are the appropriate Laplace and Fourier contours, respectively, chosen to satisfy causality [Bers, 1983].

The time-asymptotic evolution of $G(z, t)$ can belong to one of only two possible categories [Landau and Lifshitz, 1953; Bers, 1983 and references therein]:

- (a) an absolute instability, where the response grows in time and encompasses more and more of the space as a function of time – the response always including the spatial location of the initial perturbation; thus, every spatial point eventually becoming unstable, i.e. having temporally growing fields;
- (b) a convective instability, where the initial response grows in time but propagates away from its point of origin; thus, any spatial point eventually becoming stable, i.e. having temporally decaying (or oscillatory) fields.

As shown by Bers and Briggs [Briggs, 1964; Bers, 1983], for an unstable medium [an unstable medium is one for which $D(k_r, \omega) = 0$ (k_r being the real- k) gives at least one branch, $\omega(k_r)$, that has a positive imaginary part, $\omega_i(k_r) > 0$, for some k_r], this distinction in the time-asymptotic behavior of (2) is obtained by determining the pinch-point saddles in k (at $k = k_0$), and the associated branch points in ω (at $\omega = \omega_0$) given by:

$$D(k_0, \omega_0) = 0, \quad \frac{\partial D(k_0, \omega_0)}{\partial k} = 0 \quad (3)$$

The time asymptotic Green's function is dominated by the pinch point associated with the largest value of ω_{0i} (ω_{0i} being the imaginary part of ω_0). If that ω_{0i} is positive then the instability evolves as an absolute instability. If ω_{0i} is negative for all the pinch points then the instability will evolve as a convective instability.

Discussion of the Examples used in Oscarsson and Rönnmark [1986]

Before we consider the examples in Oscarsson and Rönnmark [1986], two remarks are in order. First, the notion of time-asymptotics should not be considered, trivially, as simply $t \rightarrow \infty$; in this limit any linear instability will have long violated the, ab-initio, assumption of small-amplitude fields. A time-asymptotic state is established as soon as the contribution from the pinch point with the largest ω_{0i} dominates over the contribution of

the pinch point with the next largest ω_0 ; this gives a time-asymptotic time scale which is quite finite. The importance of nonlinear effects over such time scales of evolution must, of course, be assessed separately; this notwithstanding, the linear theory of absolute and convective instabilities has important applications in its own right. The nonlinearly saturated state can depend crucially on whether an instability evolves as an absolute or as a convective instability during its linear stage [Bers, 1983].

Second, the evolution of an arbitrary initial perturbation, $\psi_0(z)$ at $t = 0$, is obtained by convolving the Green's function with $\psi_0(z)$ [Morse and Feshbach, 1953]. Clearly, if $\psi_0(z)$ is spatially localized, $\psi(z, t)$ will evolve in a manner determined by the Green's function. Thus, if the Green's function analysis indicates the medium is absolutely (convectively) unstable, $\psi(z, t)$ will evolve as an absolute (convective) instability. However, if $\psi_0(z)$ extends all the way to $\pm\infty$ then $\psi(z, t)$ may not, in general, evolve in a manner indicated by the Green's function.

We now consider the examples treated in Oscarsson and Rönnmark [1986] and show that they are not characteristic of space-time evolution of instabilities; they describe an instability that evolves essentially in time only and, thus, are singular examples. The dispersion function of Oscarsson and Rönnmark [1986] is:

$$D(k, \omega) = \omega - kv_0 - i\gamma \quad (4)$$

where v_0 and γ are constants. The corresponding equation describing the evolution of the electric field, $E(z, t)$, is of the form:

$$\frac{\partial E(z, t)}{\partial z} + \frac{1}{v_0} \frac{\partial E(z, t)}{\partial t} - \frac{\gamma}{v_0} E(z, t) = 0 \quad (5)$$

This is a hyperbolic partial differential equation with its characteristics given by $z - v_0 t = \text{constant}$. It is easy to realize that (5) is a singular equation which is not generic of space-time evolution. If we replace z and t by $\xi = z - v_0 t$ and $\tau = t$, respectively, then (5) becomes:

$$\frac{\partial E(\xi, \tau)}{\partial \tau} - \gamma E(\xi, \tau) = 0 \quad (6)$$

Obviously, this equation describes the evolution of E in time and has nothing to do with space-time. So the concept of an absolute or convective evolution of an instability, which defines the space-time response of a medium, is not defined for such an equation. The solution to (6) is:

$$E(\xi, \tau) = e^{\gamma(\tau - \tau_0)} E_0(\xi, \tau_0) \theta(\tau - \tau_0) \quad (7)$$

where E_0 is the initial prescribed value of the field at $\tau = \tau_0$, and θ is the Heaviside function needed to satisfy causality. Thus, the solution to (5) is:

$$E(z, t) = e^{\gamma(t - t_0)} E_0(z - v_0 t, t_0) \theta(t - t_0) \quad (8)$$

This equation implies that the field at a point z at time t has grown uniformly in time (at the rate given by γ)

from the value of the field at position $z - v_0 t$ at time t_0 . There is only a trivial spatial evolution of the field along the characteristics.

The Green's function for (5) is:

$$G(z, t) = \begin{cases} v_0 e^{\gamma t} \delta(z - v_0 t) \theta(t), & v_0 \neq 0 \\ e^{\gamma t} \delta(z) \theta(t), & v_0 = 0 \end{cases} \quad (9)$$

For $v_0 \neq 0$, this shows that the instability convects away from its initial point of origin. However, in a reference frame moving with velocity v_0 , the instability just grows in time without any spatial evolution. The case when $v_0 = 0$ does not represent any space-time evolution; thus, there is no pinch point to speak of and it is irrelevant to speak of absolute or convective instability. This, again, points out the singular nature of the dispersion function in (4). This is not a restriction on the applicability of the theory of absolute and convective instabilities. Rather, the point is that when a simplified dynamic description ignores space-time evolution there is no reason for distinguishing between absolute and convective instabilities. For example, the ion-acoustic wave instability, when treated properly, has a well-defined space-time evolution [Francis et al., 1986]; its simplified representation by a dispersion relation such as given by (4) would not describe its space-time evolution.

It is important to realize that, for the dispersion function of (4) with $v_0 \neq 0$, the spatial width of any instability does not change with time. For plasmas described by non-singular dispersion relations, this is not the case for either absolute or convective instabilities. Any arbitrary perturbation, in general, will spread spatially beyond its original spatial width. By choosing initial perturbations that extend all the way to $\pm\infty$, Oscarsson and Rönnmark [1986] have attempted to create the impression that the perturbations evolved spatially (instead of just temporally). We highlight that aspect by considering in detail one of the examples they used.

By using the Green's function given above, the time evolution of an initial perturbation:

$$E(z, 0) = \exp(-z^2/d^2) \exp(-ik_0 z) \quad (10)$$

is given by [Morse and Feshbach, 1953]:

$$E(z, t) = \exp\left\{-\frac{(z - v_0 t)^2}{d^2}\right\} \exp(\gamma t) \times \exp\{-ik_0(z - v_0 t)\} \quad (11)$$

All points in space, in the coordinate system moving with velocity v_0 , grow at the same rate. This can be further emphasized by choosing $E(z, 0)$ to be initially localized:

$$E(z, 0) = \exp(-z^2/d^2) \exp(-ik_0 z) \times \frac{1}{2} \{\theta(z - l) + \theta(z + l)\} \quad (12)$$

where l can be chosen to be as large as one wants. Then it is easy to show that at any time $t > 0$ the field will be confined to a spatial width of $2l$ and will not extend beyond that width.

Acknowledgements. This work was supported by NASA Grant No. NAGW-2048 and NSF Grant No. ECS-88-2475.

References

- Bers, A., Space-time evolution of plasma instabilities – absolute and convective, in Handbook of Plasma Physics, Vol. 1, edited by M. N. Rosenbluth, and R. Z. Sagdeev, pp. 451-517, North-Holland, Amsterdam, 1983.
- Briggs, R. J., Electron-Stream Interaction with Plasmas, 187 pp., MIT Press, Cambridge, 1964.
- Francis, G., A. K. Ram, and A. Bers, Finite temperature effects on the space-time evolution of two-stream instabilities, Phys. Fluids, **29**, 255-261, 1986.
- Landau, L D., and I. M. Lifshitz, Electrodynamics of Continuous Media (in Russian), 417 pp., GITTL, Moscow, 1953; see also their Fluid Mechanics, 536pp., Pergamon Press, London, 1959.
- Morse, P. M., and H. Feshbach, Methods of Theoretical Physics, 997 pp., McGraw-Hill, New York, 1953.
- Oscarsson, T. E., and K. G. Rönmark, Comments on the theory of absolute and convective instabilities, Geophys. Res. Lett., **13**, 1384-1386, 1986.
- Ram, A. K., and A. Bers, Absolute versus convective analysis of instabilities in space plasmas, in Physics of Space Plasmas (1990), SPI Conference Proceedings and Reprint Series, Number 10, edited by T. Chang, G. B. Crew, and J. R. Jasperse, pp. 351-365, Scientific Publishers, Cambridge, 1991; also, Plasma Fusion Center Report PFC/JA-91-4, 15 pp., Massachusetts Institute of Technology, Cambridge, 1991.
- A. Bers and A. K. Ram, Plasma Fusion Center and Research Laboratory of Electronics, Massachusetts Institute of Technology, Cambridge, MA 02139.

(Received April 8, 1991;
revised July 22, 1991;
accepted November 15, 1991.)

APPENDIX D

Space-Time Propagation of Electromagnetic Instabilities Across the Magnetic Field in Auroral Regions*

A K Ram and A Bers (Both at: Plasma Fusion Center, MIT,
Cambridge, MA 02139; 617-253-2595)
(Sponsor: AGU Member)

We have shown that the space-time analysis of instabilities leads to distinctly observable features that can identify whether an instability is absolute or convective.¹ An absolute instability has a narrow frequency bandwidth while a convective instability typically has a broad band emission. We consider instabilities that propagate across an ambient, steady-state magnetic field, and are generated by relativistic, highly anisotropic, electron distribution functions. Such distribution functions arise in the auroral regions and are considered to be sources of the observed auroral kilometric radiation.² We study the propagation of the ordinary and the extraordinary (x) modes. The instabilities are generated at the electron cyclotron frequency (ω_{ce}) and its harmonics. For low electron densities, the x-mode is an absolute instability at ω_{ce} and a convective instability at the harmonics. As the density is increased the instability at ω_{ce} becomes convective while that at $2\omega_{ce}$ becomes absolute, thereby, leading to harmonic generation of radiation by a linear mechanism. Detailed results for these instabilities and the effect of a cold background plasma on the propagation of these instabilities will be presented.

*Work supported by NASA Grant No. NAGW-2048.

¹A. K. Ram and A. Bers in *Physics of Space Plasmas (1990)*, Proceedings of the 1990 Cambridge Workshop in Geoplasma Physics, Eds. T. Chang, G. B. Crew, and J. R. Jasperse (Scientific Publishers, MA).

²C. S. Wu and L. C. Lee, *Astrophys. J.* **230**, 621 (1979).

SPACE-TIME PROPAGATION OF
ELECTROMAGNETIC INSTABILITIES ACROSS
THE MAGNETIC FIELD IN AURORAL REGIONS

A. K. RAM & A. BERS

M.I.T.

AGU MEETING
DECEMBER 10, 1991

- WHAT IS THE SIZE OF THE SOURCE REGION
REQUIRED FOR AURORAL KILOMETRIC RADIATION
TO ACHIEVE SUBSTANTIAL AMPLITUDES ?
(INHOMOGENEITY SCALE LENGTH)
- WHAT ARE THE CONDITIONS FOR THE GENERATION
OF HARMONIC AURORAL KILOMETRIC RADIATION ?
(BENSON - 1982)

GREEN'S FUNCTION ANALYSIS (ONE SPATIAL DIMENSION)

- LINEAR RESPONSE TO A LOCALIZED BROADBAND $[\delta(z)\delta(t)]$ NOISE SPECTRA IN A HOMOGENEOUS MEDIUM :

$$G(z,t) = \int_L \frac{d\omega}{2\pi} \int_F \frac{dk}{2\pi} \frac{e^{ikz-i\omega t}}{D(k,\omega)}$$

- TIME ASYMPTOTIC PROPERTIES OF $G(z,t)$ ARE DETERMINED BY "PINCH POINTS" (k'_0, ω'_0) :
(BERS - 1983 ; BRIGGS - 1964)

$$\bar{D}(k'_0, \omega'_0) = 0 \quad ; \quad \frac{\partial \bar{D}}{\partial k'}(k'_0, \omega'_0) = 0$$

$$\bar{D}(k', \omega') = D(k(k', \omega'), \omega(k', \omega'))$$

$$k = \gamma(k' + \omega' \frac{v}{c^2}) \quad ; \quad \omega = \gamma(\omega' + k'v)$$

$$v = \frac{z}{t} \quad ; \quad \gamma = \left(1 - \frac{v^2}{c^2}\right)^{-1/2}$$

- $\lim_{t \rightarrow \infty} G(z, t) \longrightarrow \left(\frac{\gamma}{t} \right)^{3/2} \exp \left\{ -i \frac{\omega'_0(v)t}{\gamma} \right\}$

- THE ENVELOPE OF THE GREEN'S FUNCTION IS GIVEN BY :

$$\lim_{t \rightarrow \infty} \ln |G(z, t)| \longrightarrow \underbrace{\frac{\omega'_{0i}(v)}{\gamma} t}_{\Gamma(v)}$$

- PULSE SHAPE : $\Gamma(v)$ VERSUS v
- SELF - SIMILAR EVOLUTION :

$$\underbrace{\Gamma(v) t}_{\text{AMPLITUDE}} \longleftrightarrow \underbrace{vt}_{\text{SPATIAL EXTENT}}$$

ELECTRON CYCLOTRON MASER TYPE OF INSTABILITIES

- SUCH INSTABILITIES MAYBE THE SOURCE OF AURORAL KILOMETRIC RADIATION
(WU & LEE - 1979 ; MELROSE - 1976)
- WE CONSIDER MASER TYPE OF INSTABILITIES GENERATED BY ANISOTROPIC ELECTRON (RING - TYPE) DISTRIBUTION FUNCTIONS ($\omega \gg \omega_{ci}$ - IGNORE ION DYNAMICS)

$$f_{0e} = \frac{1}{2\pi p_{0\perp}} \delta(p_{\perp} - p_{0\perp}) \delta(p_{\parallel} - p_{0\parallel})$$

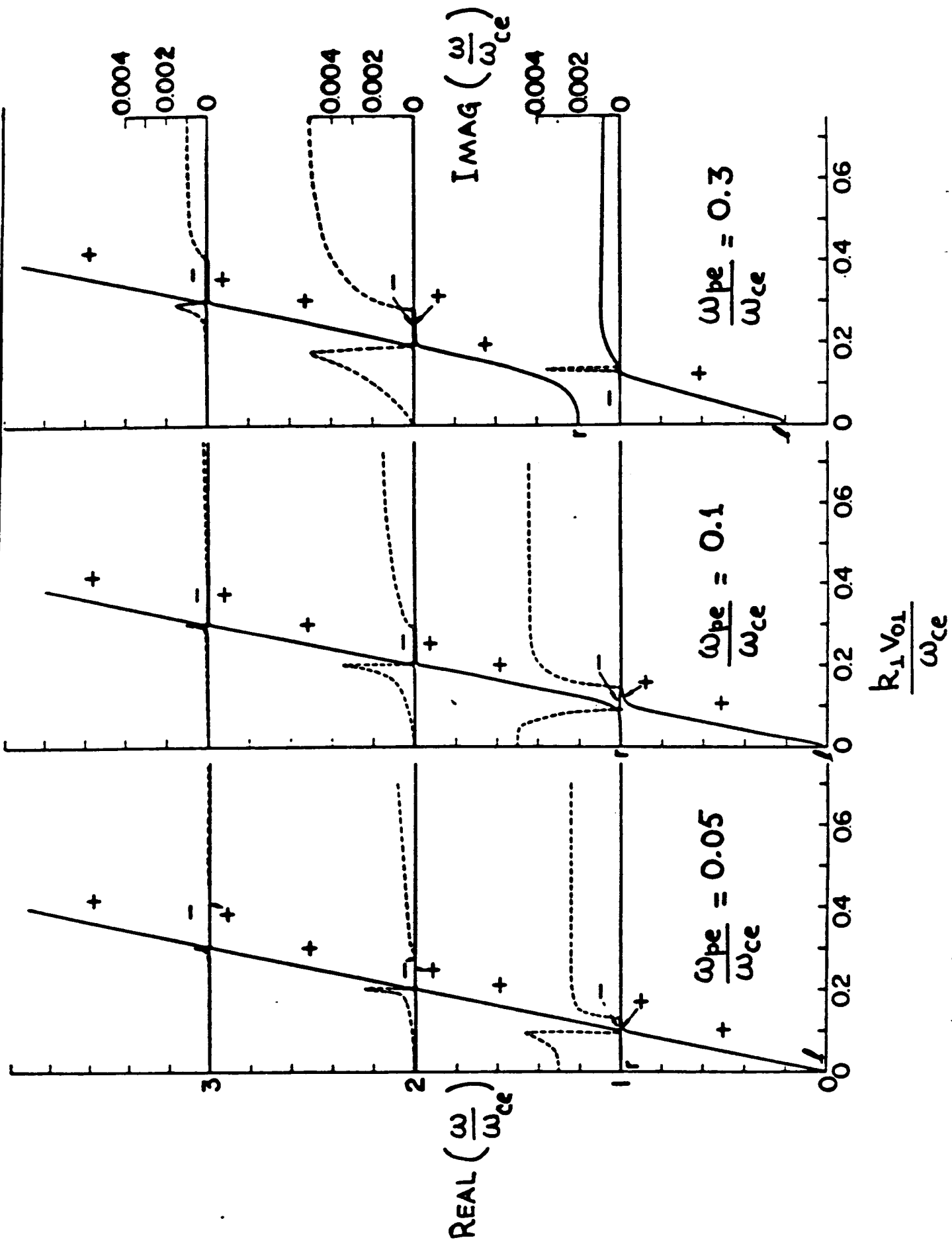
- PLASMA IN A UNIFORM MAGNETIC FIELD (\vec{B}_0).
- CONSIDER EXTRAORDINARY ELECTROMAGNETIC MODE PROPAGATING ACROSS \vec{B}_0 ($k_{\parallel} = 0$)
- DISPERSION RELATION DERIVED FROM FULLY RELATIVISTIC VLASOV EQUATION + MAXWELL'S EQUATIONS

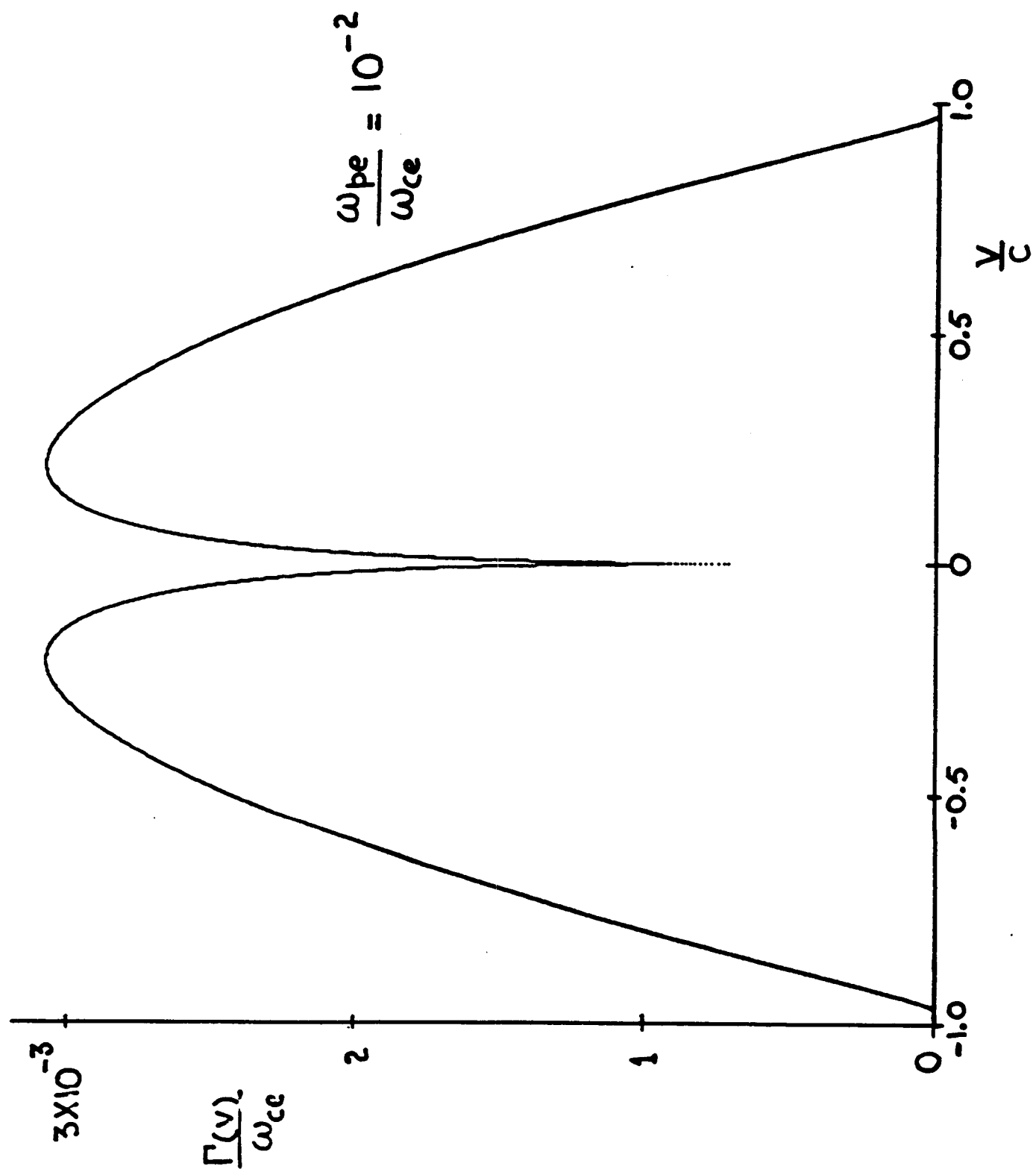
$$\bullet \quad v_{0\perp} = \frac{p_{0\perp}}{\gamma_0 m_e} \quad v_{0\parallel} = \frac{p_{0\parallel}}{\gamma_0 m_e}$$

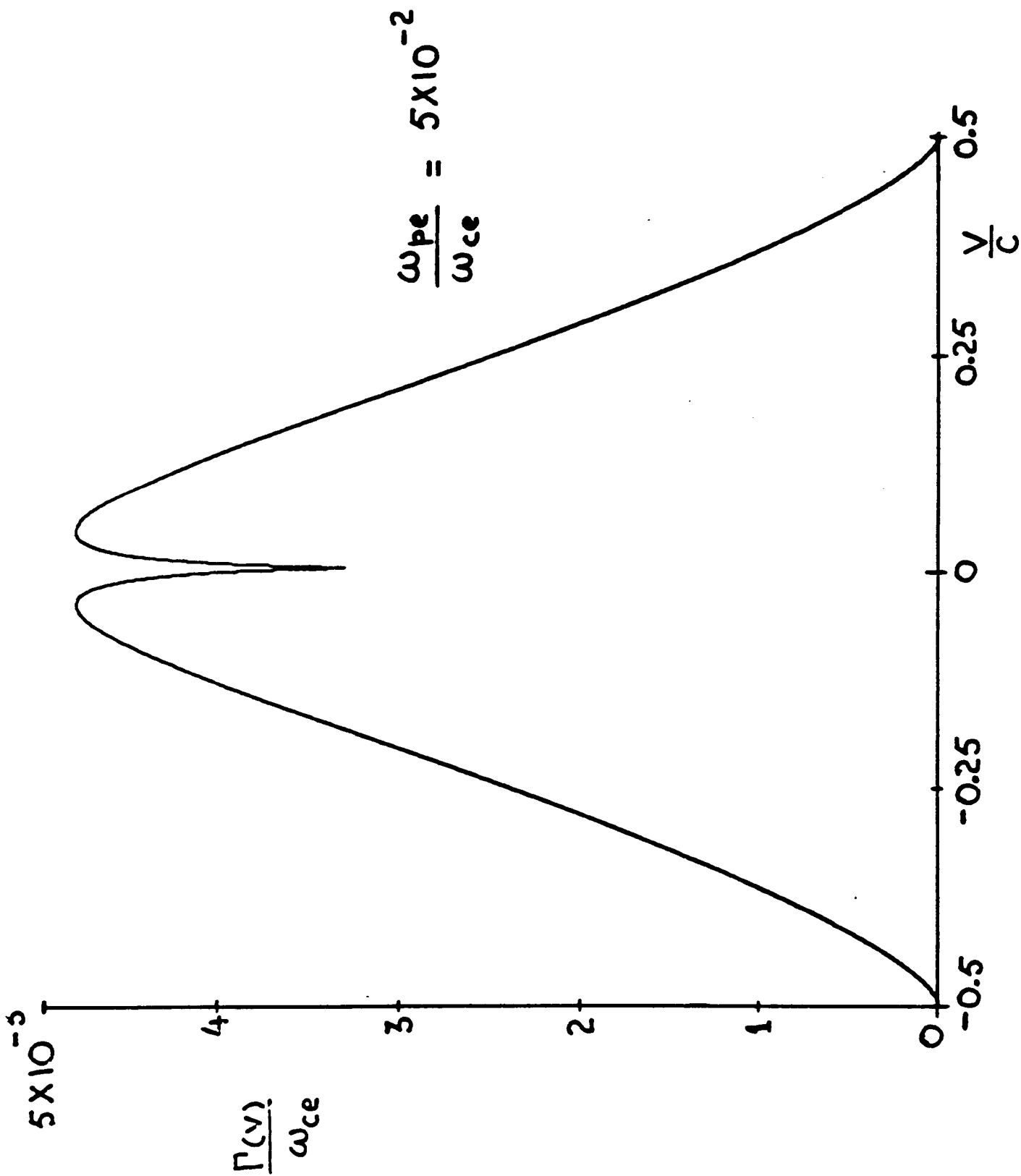
$$\gamma_0 = \left[1 + \frac{p_{0\parallel}^2}{m_e^2 c^2} + \frac{p_{0\perp}^2}{m_e^2 c^2} \right]^{1/2}$$

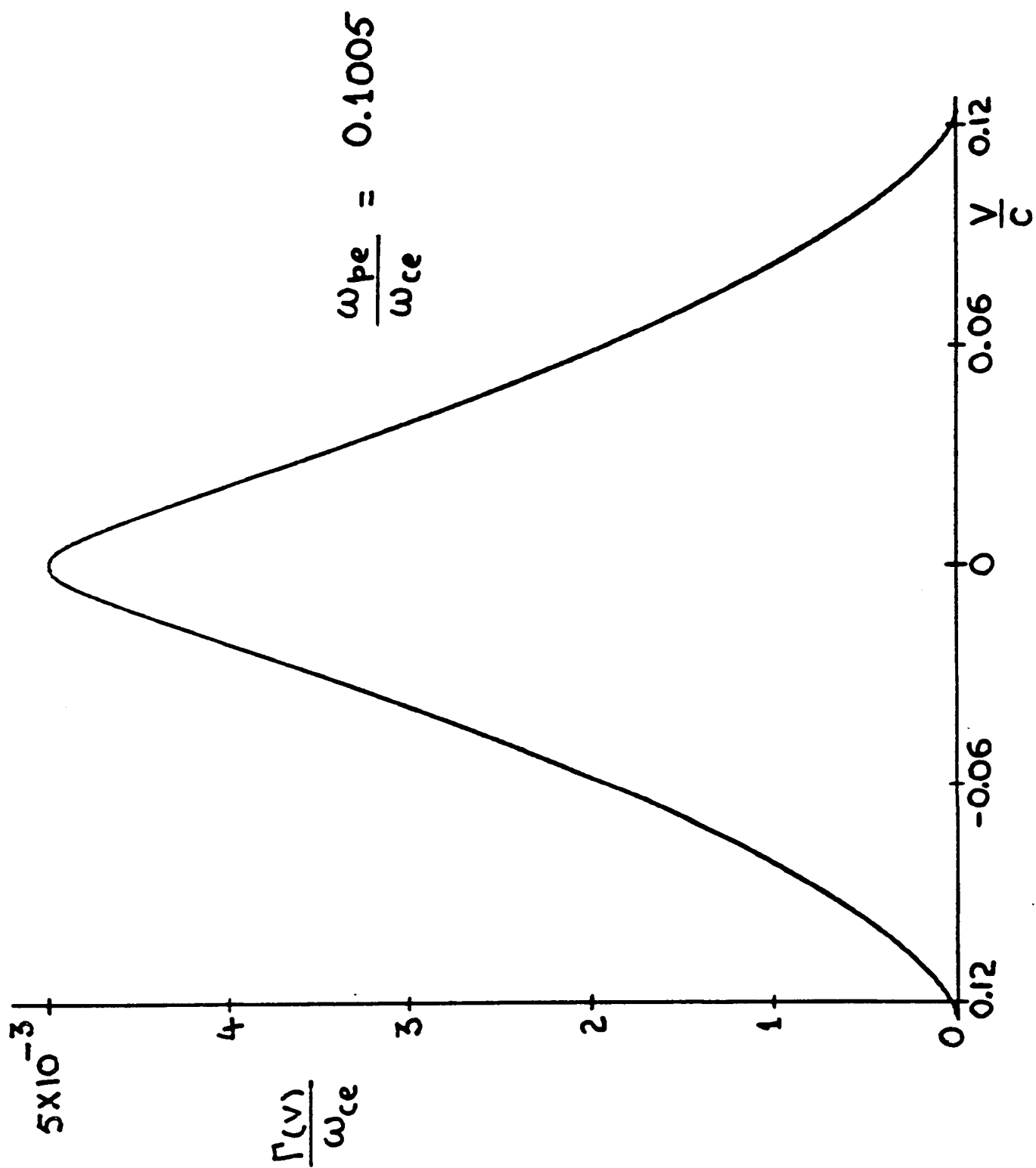
$$\bullet \quad \frac{v_{0\perp}}{c} = 0.1 \quad \frac{v_{0\parallel}}{c} = 0$$

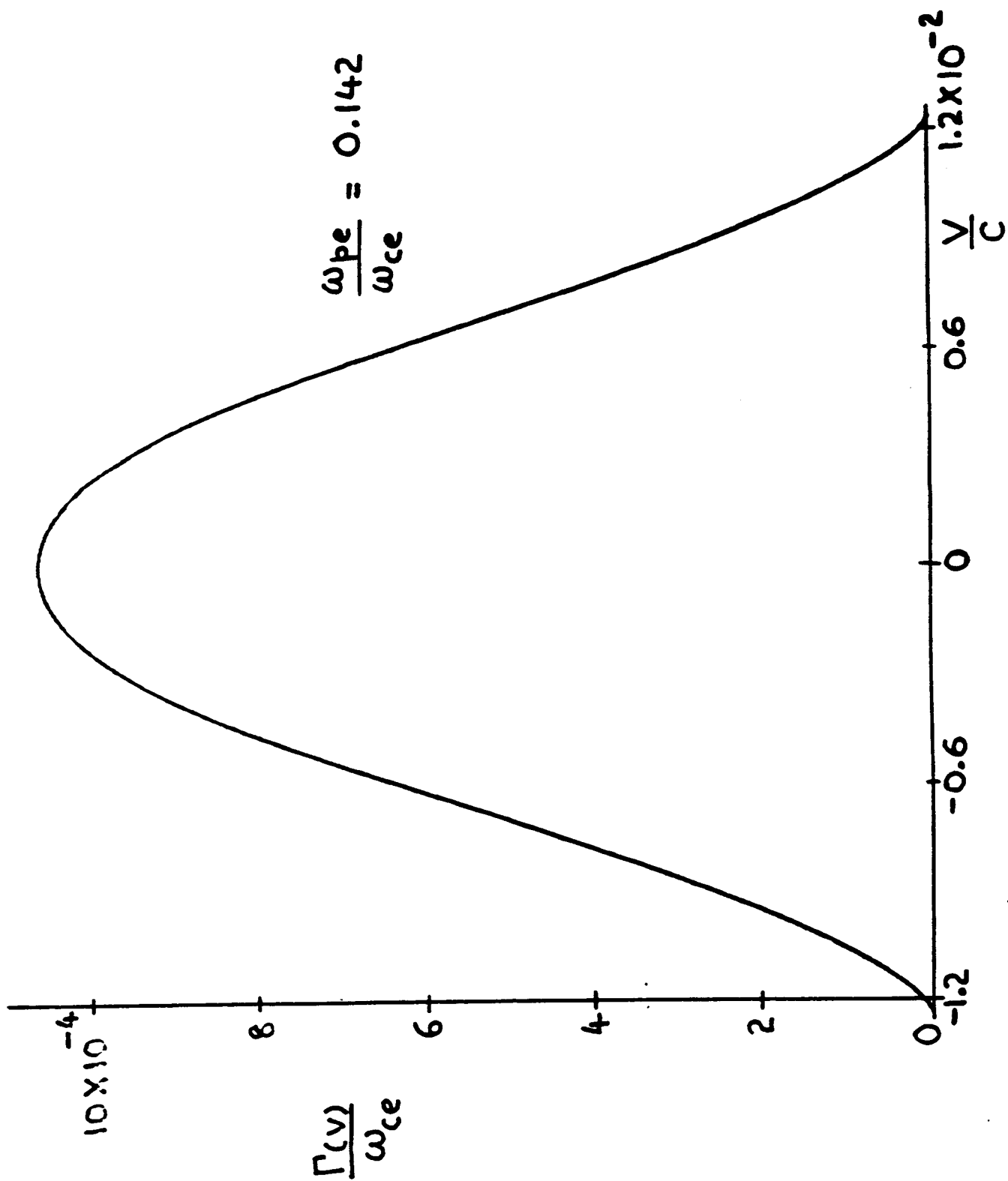
EXTRAORDINARY MODE (PROPAGATION ACROSS \vec{B}_0)







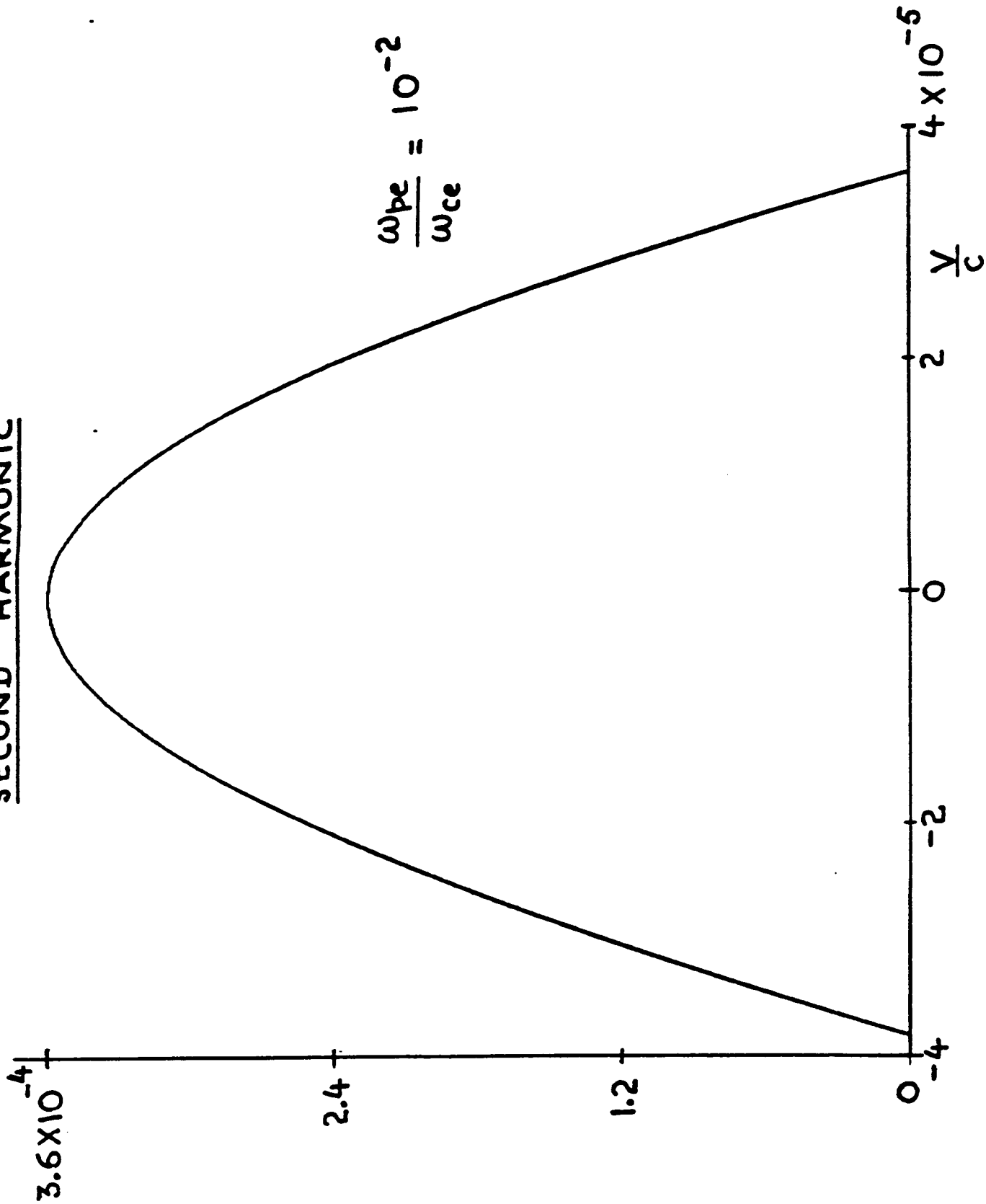




$\frac{\omega_{pe}}{\omega_{ce}}$	$\left. \frac{\Gamma(v)}{\omega_{ce}} \right _{\text{MAX}}$	$\frac{\text{EDGE VELOCITY}}{c}$	SCALE LENGTH (km.)
0.01	3.1×10^{-3}	1	123
0.05	4.8×10^{-3}	0.5	39
0.1005	5.0×10^{-3}	0.12	9
0.142	1.1×10^{-3}	0.012	4

$\nu_{ce} = 500 \text{ kHz}$
 FOR LINEAR GROWTH TO 4 e - FOLDINGS

SECOND HARMONIC



- $\frac{\omega_{pe}}{\omega_{ce}} = 0.01$

$$\frac{\Gamma(v)}{\omega_{ce}} = 3.6 \times 10^{-4}$$

$$\text{EDGE VELOCITY} = 4 \times 10^{-5} c$$

$$\text{SCALE LENGTH} = 42 \text{ m.}$$

$$\text{FOR } \nu_{ce} = 500 \text{ kHz}$$

AND FOR LINEAR GROWTH TO 4 e-FOLDINGS

- SLOW WAVE ($v_{\text{PHASE}} < c$)

CAN UNDERGO CYCLOTRON RESONANCE

DAMPING FOR SMALL k_{\parallel}

CONCLUSIONS

- EMISSION AT THE FUNDAMENTAL ELECTRON CYCLOTRON FREQUENCY IS AN ABSOLUTE INSTABILITY FOR THE FAST WAVE
 - * SCALE LENGTH FOR GROWTH DECREASES WITH INCREASING DENSITY UNTIL THE MODE STABILIZES
 - * CANNOT UNDERGO LANDAU DAMPING
 - * PERSISTS AT ANY ANGLE TO \vec{B}_0 .
- EMISSION AT SECOND HARMONIC IS A CONVECTIVE INSTABILITY FOR THE FAST WAVE
- EMISSION AT SECOND HARMONIC IS AN ABSOLUTE INSTABILITY FOR THE SLOW WAVE
 - * SCALE LENGTHS FOR GROWTH ARE VERY SMALL
 - * PERSISTS FOR A WIDE RANGE OF DENSITIES
 - * WILL CYCLOTRON RESONANCE DAMP FOR SMALL $k_{||}$.

APPENDIX E

SPI CONFERENCE PROCEEDINGS AND REPRINT SERIES

Series Editor: T. S. Chang

Number 11

Physics of Space Plasmas (1991)

*Proceedings of the
1991 Cambridge Workshop in Geoplasma Physics on
Nonlinear Phenomena and Active Experiments
1991 MIT Winter Symposium on the
Physics of Space Plasmas*

EDITORS

T. Chang, G. B. Crew and J. R. Jasperse



Scientific Publishers, Inc.

THE THREE WAVE INTERACTION AND SPATIOTEMPORAL CHAOS

Carson C. Chow, A. Bers and A.K. Ram
Plasma Fusion Center and Research Laboratory for Electronics
Massachusetts Institute of Technology
Cambridge, MA 02139

ABSTRACT

A tutorial account of spatiotemporal chaos (STC) in the nonlinear three wave interaction (3WI) is presented. The concept of STC is discussed and the 3WI is used as a paradigm for STC. Previous results of the 3WI, including time only solutions, low dimensional chaos, spacetime parametric interactions, solitons and the inverse scattering transform will be reviewed. These results will then provide the foundation to understanding STC in the 3WI.

I. INTRODUCTION

In the recent past the area of nonlinear dynamics has witnessed two major discoveries—dynamical chaos and the inverse scattering transform (IST). Chaos is customarily defined to mean randomness in deterministic systems due to extreme sensitivity of initial conditions; considerable attention has been given to mostly low dimensional or few degree of freedoms dynamical systems [1, 2]. Although the ground work for chaos was laid out by Poincaré, it was the advent of computer simulations that led to the explosion of results and excitement in the last decade. The IST is a method to integrate certain special nonlinear partial differential and difference equations. These equations are usually associated with exhibiting solitons, nonlinear structures that preserve their form and collide elastically. Soliton solutions can be explicitly calculated with IST. The IST was first used by Gardner, Greene, Kruskal and Miura [3] to solve the Korteweg-deVries equation. It was later discovered that their method was applicable to other PDE's [4, 5] and in the ensuing years the growth of the field has been prodigious.

With these two discoveries some natural questions come to mind: (1) What happens when more dimensions or degrees of freedom are added to a low dimensional chaotic system? (2) What happens when a spatially extended system, integrable by IST is perturbed slightly to break the integrability? Both of these questions will be addressed in this paper. The 3WI is a system that can be used to answer these questions. The conservative

form of the 3WI in space and time is integrable by IST, and the nonconservative form in time only (spatially uniform) is chaotic. The dynamics of a nonconservative, nonintegrable spatially extended form of the 3WI was recently studied by us. The result is what has come to be called spatiotemporal chaos (STC). The term STC specifically refers to the chaotic evolution of patterns or coherent structures at a specific length scale in a spatially extended system [6–9]. This is in contrast to fully developed turbulence where there is a cascade to smaller scales. The study of turbulence has been around for many decades and a variety of approaches have had only limited success in its description. It was once thought that chaos may have finally provided an answer. It is now believed that this is not the case [10]. Turbulent flow is full of coherent structures at all scales and is much more complicated than low dimensional chaotic dynamics can address. STC lies in a regime between the two extremes and is an interesting dynamical state in its own right.

The paper is organized as follows. The 3WI is introduced in section II and discussed in some detail. This is followed by the spatially uniform or time only dynamics in section III; both the integrable and chaotic situations are reviewed. Section IV is devoted to the spatiotemporal 3WI; the linearized parametric instability and the IST solutions of the nonlinear equations are reviewed. Finally in section V, a discussion of STC in general and its manifestation in the 3WI is presented.

II. THE NONLINEAR THREE WAVE INTERACTION

The nonlinear 3WI appears in many contexts within the fields of plasma physics, nonlinear optics and hydrodynamics. Ref. 11 provides an excellent review of its applications. It can occur whenever: (1) a weakly nonlinear medium supports a set of discrete waves

$$\omega_l = \omega_l(k) \quad (1)$$

(2) The nonlinearity is manifested as a coupling of slowly varying linear field amplitudes, (3) The lowest order nonlinearity is quadratic in the field amplitudes, and (4) the three coupled waves satisfy the resonance conditions

$$\omega_i = \omega_j + \omega_k \quad (2)$$

$$k_i = k_j + k_k. \quad (3)$$

These last two conditions are akin to conservation of energy and momentum. If these conditions are satisfied and the nonlinear coupling is conservative then a slowly varying amplitude or wave packet expansion will yield

the conservative and integrable nonlinear 3WI [12, 13]

$$(\partial_t + \mathbf{v}_i \cdot \nabla) a_i = -K a_j a_k \quad (4)$$

$$(\partial_t + \mathbf{v}_j \cdot \nabla) a_j = K^* a_i a_k^* \quad (5)$$

$$(\partial_t + \mathbf{v}_k \cdot \nabla) a_k = K^* a_i a_j^* \quad (6)$$

where the a 's are the slowly varying complex wave envelopes, K is a coupling coefficient and the \mathbf{v} 's are the group velocities. The above form of the 3WI is integrable by IST. Wave a_i will be referred to as the parent and the other two waves are the daughters. The solution will be discussed in section IV.

In many physical situations there will not be exact integrability. For instance the linear waves may have some growth or damping associated with them

$$\omega_l = \omega_l(k_l) + i\gamma_l(k_l) \quad (7)$$

There may also be the situation where the resonance is not exact so that

$$\omega_j + \omega_k - \omega_i = \delta \neq 0 \quad (8)$$

This results in a dephased interaction. From these considerations a non-conservative form of the 3WI can be derived [12, 14, 15]:

$$\partial_t a_i + \mathbf{v}_i \cdot \nabla a_i = -K a_j a_k \exp(-i\delta t) + \gamma_i a_i + D \nabla^2 a_i \quad (9)$$

$$\partial_t a_j + \mathbf{v}_j \cdot \nabla a_j = K^* a_i a_k^* \exp(i\delta t) - \gamma_j a_j \quad (10)$$

$$\partial_t a_k + \mathbf{v}_k \cdot \nabla a_k = K^* a_i a_j^* \exp(i\delta t) - \gamma_k a_k \quad (11)$$

Here the γ 's are growth or dissipation coefficients and D is a diffusion coefficient. This last term in Eq. (9) is usually not included in the 3WI; as will be detailed in section IV its presence is essential for nonlinear saturation and the long time behavior of the equations. It arises if the growth of the parent is assumed to have a slow spatial variation. It then gives the simplest reflection invariant cutoff in wavenumber of the growth.

These equations ignore wave particle 'quasilinear' interactions whose lowest order effect is also second order in the field amplitudes. The particles are assumed to be nonresonant with the waves. In a generalized amplitude expansion the 3WI is the lowest order nonlinear effect and so the 3WI will dominate other nonlinear effects if the resonance conditions (2) and (3) can be satisfied. For instance the celebrated nonlinear Schrödinger equation would come in at a higher order. Only one spatial dimension will be considered in the paper.

III. TIME ONLY EVOLUTION

The 3WI in time only has the form:

$$\dot{a}_i = \gamma_i a_i - K a_j a_k e^{-i\delta t} \quad (12)$$

$$\dot{a}_j = -\gamma_j a_j + K^* a_i a_k^* e^{i\delta t} \quad (13)$$

$$\dot{a}_k = -\gamma_k a_k + K^* a_i a_j^* e^{i\delta t} \quad (14)$$

The conservative, resonant interactions ($\gamma_i = 0, \delta = 0$) are easily solved in terms of Jacobi elliptic functions [16–18]. The solutions are oscillatory with a period

$$T \simeq \frac{1}{2K|a_i(0)|} \ln \frac{|a_i(0)|}{|a_j(0)|} \quad (15)$$

With the addition of the nonconservative terms closed form solutions do not exist. However, we can consider an initial situation where the daughter wave amplitudes are small. Then the equations can be linearized. This is known as a *parametric interaction*. Linearizing (12) yields

$$a_i(t) = a_i(0)e^{\gamma_i t} \quad (16)$$

The other two equations become

$$\dot{a}_j + \gamma_j a_j = K^* a_i(t) a_k^* \quad (17)$$

$$\dot{a}_k^* + \gamma_k a_k^* = K a_i(t)^* a_j \quad (18)$$

Now assume that $a_i(t)$ is very slowly varying and substitute in the following

$$a_j = A_j e^{pt}, \quad a_k^* = A_k^* e^{pt}, \quad \gamma = |K a_i(t)| \quad (19)$$

This then yields the dispersion relation

$$(p + \gamma_j)(p + \gamma_k) - \gamma^2 = 0. \quad (20)$$

The threshold for instability is given by $\gamma^2 > \gamma_j \gamma_k$. So for a slowly growing high-frequency mode a_i there will always be a parametric interaction instability. The question is what happens nonlinearly.

This question was studied in references [19–21]. It was shown that there is no nonlinear saturation unless the interaction is off resonance (i.e. $\delta \neq 0$). In those works the damping rates of the two daughters were chosen equal. The essential parameters governing the dynamics were the dephasing δ and the ratio of the dissipation to the growth γ_j/γ_i . Depending on the

values of these parameters they observed regions of no saturation, stable equilibrium, period doubling route to chaos, and intermittency.

IV. SPACETIME EVOLUTION

The spacetime conservative 3WI is integrable by Inverse Scattering Transforms (IST) [11, 22–24]. Ref. 11 provides a complete review of the solution. IST is a transform technique to solve certain classes of nonlinear partial differential equations, and difference equations. Other equations integrable by IST include the Korteweg-de Vries, sine-Gordon, and nonlinear Schrödinger equations. One notable feature of IST theory is the ability to explicitly calculate soliton solutions.

In the 3WI the order of the group velocities gives different behavior. The case where parent wave has the middle group velocity is known as the Soliton Decay Instability. The IST solutions for the conservative case on the infinite domain show that solitons exist but they do not necessarily belong uniquely to a particular envelope [11, 22, 24]. Solitons in the parent wave tend to deplete to solitons in the daughters which propagate away. The simplest soliton solution for decay shows that a soliton of the form $|a_i| = 2\eta \text{sech} 2\eta x$, will decay into solitons in the daughters of the form $|a_j| = \sqrt{2}\eta \text{sech} \eta(x + v_j t)$, where η is the IST spectral parameter for the Zakharov-Manakov [23] scattering problem. The spectral parameter is also the eigenvalue for a bound state in the Zakharov-Shabat [5] scattering problem with the parent pulse as the potential function. In the WKB limit η is related to the area of the parent pulse through the Bohr quantization condition [5, 11, 14]

$$\int_a^b |a_i^2 - \eta^2|^{1/2} dx = \pi/2 \quad (21)$$

where $[a, b]$ are turning points for a local pulse. A collision between a daughter pulse and a parent soliton is necessary to induce the decay of the parent [11, 24]. For arbitrary shaped parent pulses that exceed the area threshold, the soliton content will be transferred to the daughters leaving the radiation behind. Collisions between daughter solitons are elastic. The depletion of the parent into solitons is the nonlinear saturation of an absolute instability. The case where the parent wave has the highest (or lowest) group velocity is known as Stimulated Back Scatter. In this case the daughters can possess solitons but they are not transferred between the envelopes.

The inclusion of growth and dissipation breaks the integrability of the 3WI just as it did in the time only case. However, the linearized parametric instability where the daughters are initially small can be studied as in the time only case [12]. Transform to the frame of the parent wave ($v_i = 0$)

and consider $a_i(t) = \text{const} \gg a_j, a_k$ so Eqs. (10), (11) can be linearized [25]:

$$(\partial_t + v_j \partial_x - \gamma_j) a_j = \gamma a_k^* \quad (22)$$

$$(\partial_t + v_k \partial_x - \gamma_k) a_k = \gamma a_j^* \quad (23)$$

where $\gamma = |K^* a_i|$ and only one spatial dimension is considered. The dispersion relation is simply

$$D = (\omega - kv_j + i\gamma_j)(\omega - kv_k + i\gamma_k) + \gamma^2 = 0 \quad (24)$$

There is a threshold of instability

$$\gamma^2 > \gamma_j \gamma_k \equiv \gamma_c^2 \quad (25)$$

For $v_j v_k > 0$ this is a convective instability. For $v_j v_k < 0$ (parent has middle group velocity) there is an additional threshold for an absolute instability [25]:

$$\frac{\gamma}{|v_j v_k|^{1/2}} \equiv \alpha > \frac{1}{2}(|\alpha_j| + |\alpha_k|) \quad (26)$$

where $\alpha_l = \gamma_l / v_l$.

If the parent is spatially varying then one must solve a boundary value problem. For $v_j v_k < 0$ the condition for an absolute instability is the existence of a growing normal mode. The WKB condition is given by [25]:

$$\left(n - \frac{1}{2}\right) \pi \leq \int_a^b [\alpha^2 - (|\alpha_j| + |\alpha_k|)^2 / 4]^{1/2} dx \leq \left(n + \frac{1}{2}\right) \pi \quad (27)$$

where a and b are turning points. Notice that for no damping this condition is identical to the condition for soliton possession.

V. SPATIOTEMPORAL CHAOS

A. Definition

The term spatiotemporal chaos has acquired a more specific meaning than simply chaos in space and time. Although there is no official definition, STC has come to refer to the chaotic behavior of coherent structures or patterns. This is in contrast to the more familiar low dimensional chaos and fully developed turbulence. The distinction can be made on the basis of length scales. Following Hohenberg and Shraiman [6], for any chaotic dynamical system there exist certain length scales. There is: (a) the excitation length l_E , the length scale at which energy is put into the system;

(b) the dissipation length l_D , the scale at which energy is dissipated; (c) the system size L ; and (d) the coherence length ξ . Systems where energy is created and destroyed at the same length scale, $L \sim l_E \sim l_D$, $\xi > L$, correspond to low dimensional chaos. The system is completely spatially correlated. On the other extreme, in fully developed turbulence energy is usually injected at some large scale and dissipated at a small length scale, $L > l_E \gg l_D$, and the so called inertial range lies between the length scales. Also in fully developed turbulence, coherent structures exist at all scale lengths and the correlation length is not well defined. However systems where energy is injected and dissipated at the same length scale and the correlation length is much smaller than the system size, $L > l_E \sim l_D$, $\xi \ll L$, corresponds to the regime of STC. In STC there is no inertial range yet spatial degrees of freedom are very important. The clean separation of scales also allows a statistical description in that correlation functions are well defined.

B. STC in the 3WI

This finally leads us to STC in the 3WI. We studied the dynamics of the 3WI in one spatial dimension x and time t . For weakly growing and damped waves without dephasing the nonconservative form of the 3WI Eqs. (9–11) is

$$\partial_t a_i - D \partial_{xx} a_i - \gamma_i a_i = -a_j a_k \quad (28)$$

$$\partial_t a_j - \partial_x a_j + \gamma_j a_j = a_i a_k^* \quad (29)$$

$$\partial_t a_k + \partial_x a_k + \gamma_k a_k = a_i a_j^* \quad (30)$$

where the a 's are complex wave envelopes, the γ 's are growth or damping coefficients, and D is a diffusion coefficient. We have transformed to the frame of the parent wave and normalized the magnitude of the daughter group velocities to one. We will consider the case where the daughter waves have equal damping (i.e. $\gamma_j = \gamma_k$). The length and time can then be rescaled so that the damping coefficient is unity [26].

The group velocities satisfy the condition $v_k > v_i > v_j$ (i.e. the highest frequency parent wave has the middle group velocity, see [27]). In the absence of growth, damping and diffusion ($\gamma_i = D = 0$) the IST solutions for this group velocity ordering is described by soliton exchange between wavepackets [11, 22–24].

We numerically simulated the system on the domain $x \in [0, L]$ with periodic boundary conditions. We began with random real initial conditions and evolved until the transients died away before the system was analysed. It can be shown that for real valued initial conditions the envelopes remain real for all time [11, 15]. We were interested in the large system, long

time limit. We considered the case with parameters $D = 0.001$, $\gamma_i = 0.1$, $\gamma_j = \gamma_k = 1$, and $L = 20$. These parameters were chosen because they exhibit STC and fall into a regime where perturbation theory is possible. However, the system is extremely rich and different parameters do lead to vastly different behaviour. Aspects of these different regimes will be touched upon later and details are given in [15]. We measured the correlation function, $S_l(x, t) = \langle a_l(x - x', t - t') a_l(x', t') \rangle$, where the angled brackets denote time averages.

A sample of the spatiotemporal evolution profiles in the STC regime of the parent and daughter envelopes is given in Fig. 1. The length shown is one half the system size and $t = 0$ is an arbitrary time well after the transients have decayed. The profile of the parent wave is irregular but spatial and temporal scales can be observed. There are coherent structures of a definite length scale that can be seen to grow, deplete and collide with one another. The profile of the daughter wave shows a sea of structures convecting to the left. We only show one daughter, the other will be similar but with structures convecting to the right. The correlation functions for both the parent and the daughter waves are given in Fig. 2. The parent correlation function shows a gradual decay in time. Spatially, there is a definite length scale seen in Fig. 1. The daughter function is calculated along the characteristic. It has a fast decay followed by a slow decay in both time and space. The approach to zero in correlations in both space and time indicates STC. Fig. 3 shows the spectrum of static fluctuations $S_l(t = 0, q)$. For the parent wave there is a cutoff near $q \simeq 10$ and a range of modes show up as a prominent hump. The cutoff reflects the length scale seen in the spacetime profile. For q below the hump the spectrum is flat. The daughter spectrum has a cutoff around $q \simeq 6$ again indicating a length scale. Fig. 4 shows the local power spectrum $S_l(\omega, x = 0)$. The spectrum for the parent clearly shows two time scales. The spectrum bends over near $\omega \simeq 0.02$ which gives a long time scale and a shoulder at $\omega \simeq 0.3$ gives a short time scale. Longer runs with these parameters hint that there may be a very slow power law rise of undetermined exponent for frequencies below the low ω bend similar to that observed in the Kuramoto-Sivashinsky equation [6]. The short time scale appears as the growth and depletion cycle observed in the spatiotemporal profile. The daughter power spectrum has two peaks at high ω . One is where the shoulder of the parent spectrum is and the other is at twice this frequency. The spectrum begins to bend over and flatten out at $\omega \simeq 0.007$. This bend is more pronounced in longer runs. It is not known whether the spectrum becomes flat or has a power law rise like the parent for frequencies below the bend.

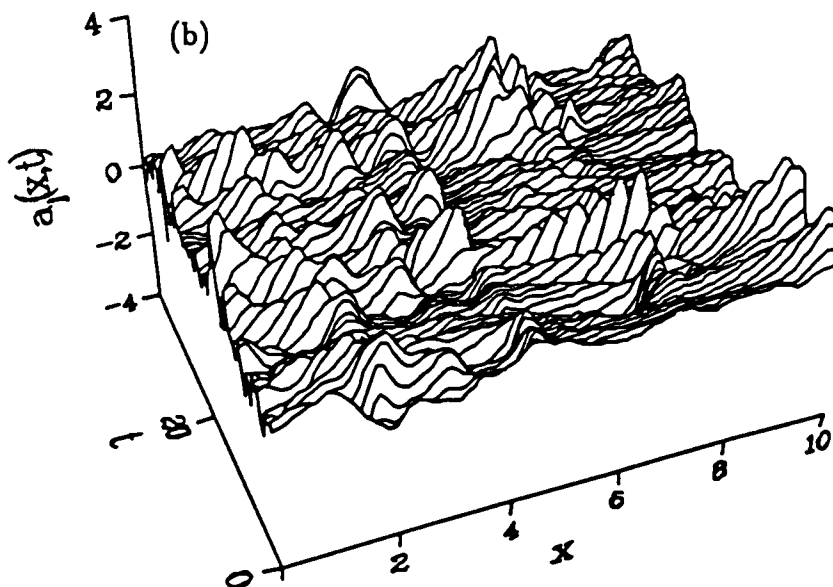
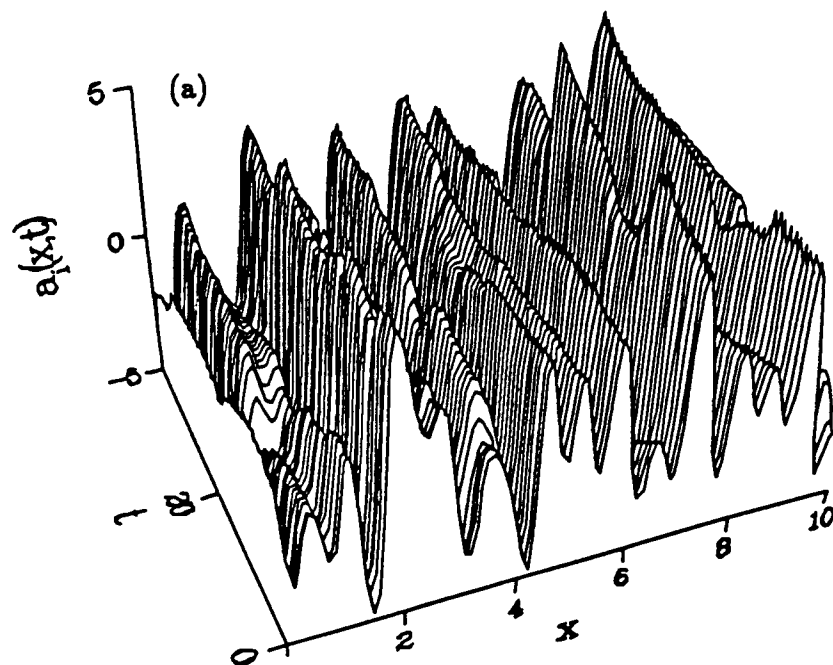


Figure 1. Spatiotemporal profiles of (a) the parent wave $a_i(x, t)$ and (b) the daughter wave $a_j(x, t)$.

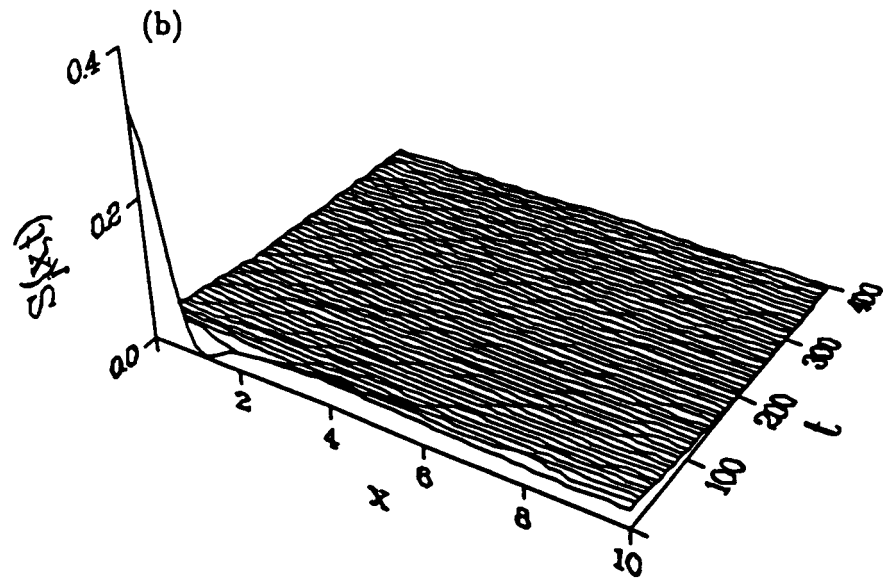
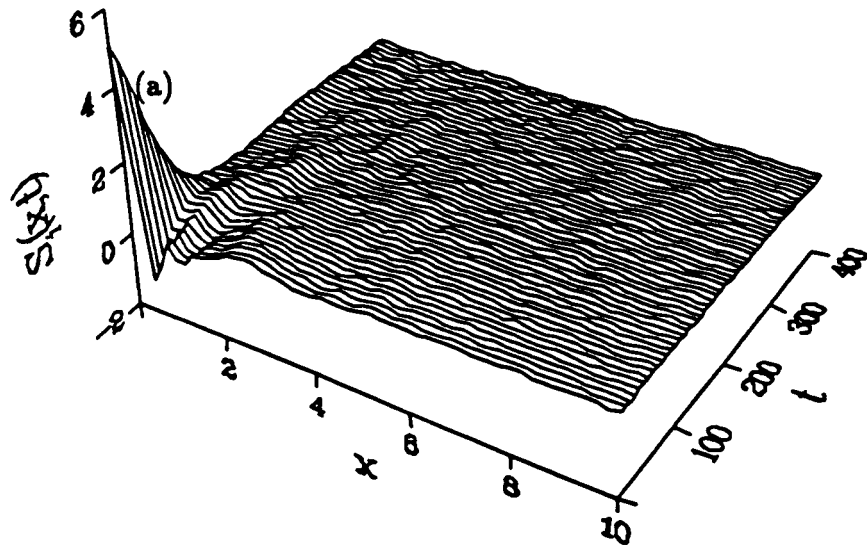


Figure 2. Correlation function $S_1(x, t)$ of (a) the parent wave and (b) the daughter wave.

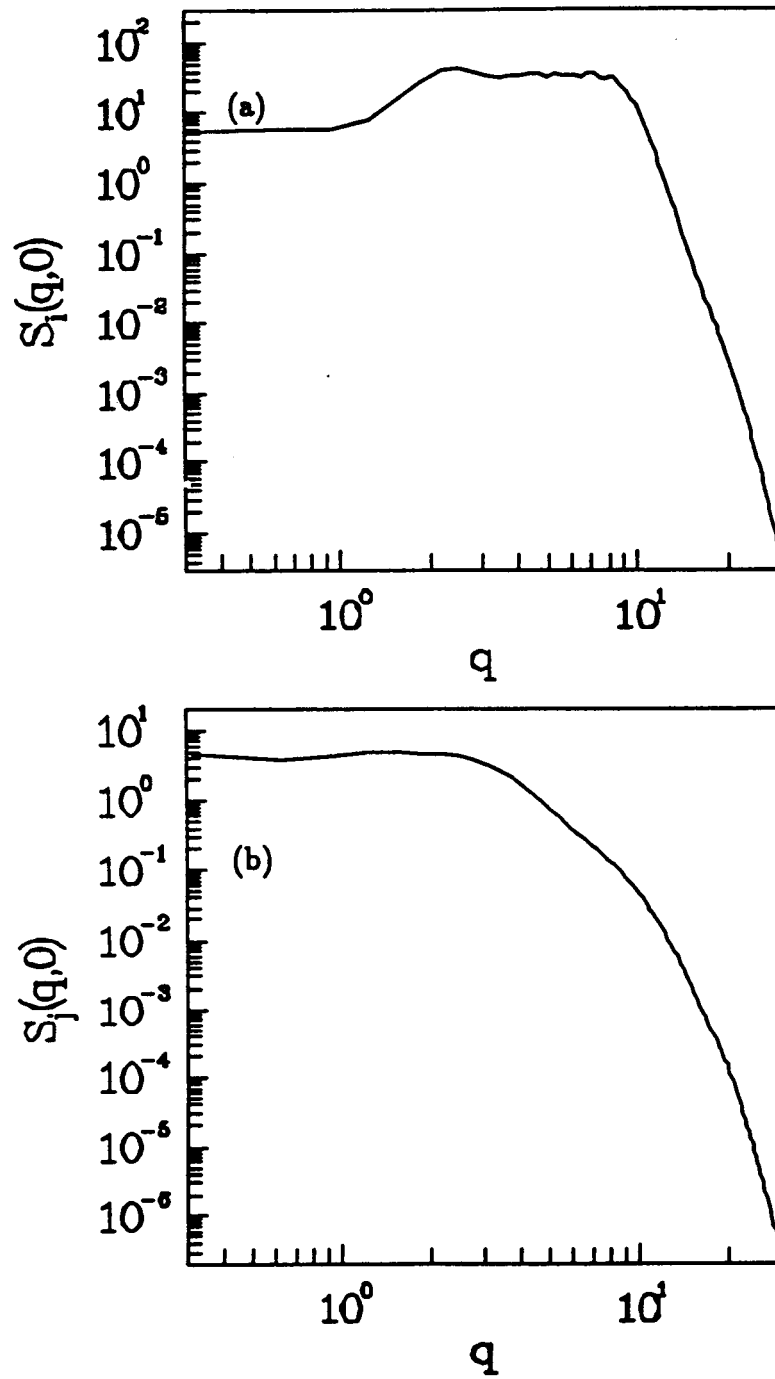


Figure 3. Spectrum of static fluctuations $S_i(q, t = 0)$ of (a) the parent wave and (b) the daughter wave.

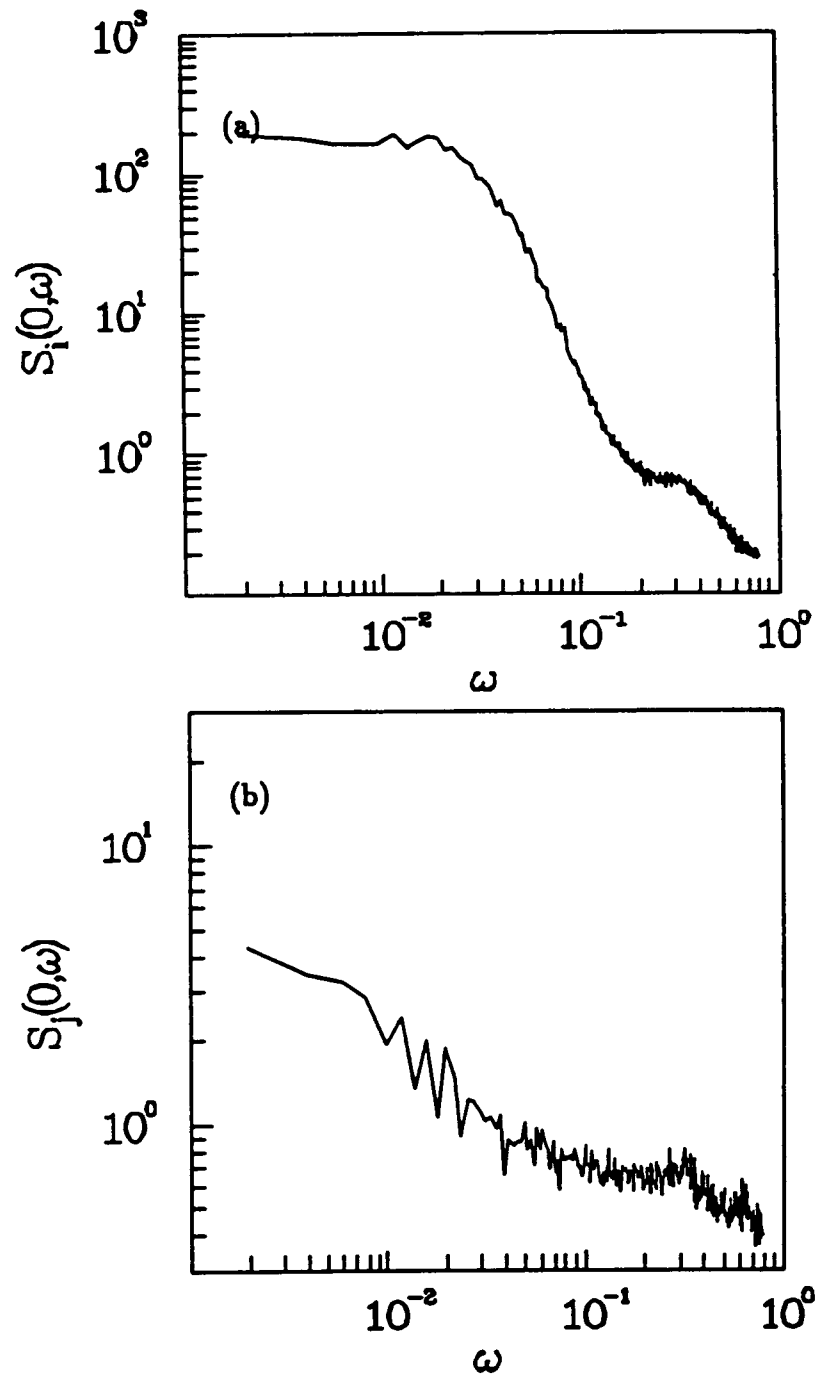


Figure 4. Local power spectrum $S_i(x = 0, \omega)$ of (a) the parent wave and (b) the daughter wave.

The main features of the behaviour can be understood if we consider the growth and dissipation as perturbations about the conservative 3WI, as discussed in Sec. IV. With the addition of weak growth and dissipation, parent pulses deplete provided they satisfy the WKB threshold condition (27). In the normalization of Eqs. (28–30) this condition is [14, 25]:

$$\int_a^b |a_i^2 - \gamma_j^2|^{1/2} dx > \pi/2 \quad (31)$$

The decay products in the daughters are quasi-solitons; they damp as they propagate away and do not collide elastically. The soliton content of the parent is not completely transferred to the daughters. The parent wave with some initial local eigenvalue η will deplete and be left with some remaining area. This area is due to the conversion of soliton content into radiation by the perturbations. This left over area can be represented by an effective “eigenvalue” η' . This remaining part of the parent will then grow until it exceeds the threshold for decay. This time denoted by t_c is given by

$$t_c \simeq \frac{1}{\gamma_i} \ln \frac{\eta}{\eta'} \quad (32)$$

The cycling time observed in the spacetime profiles is this time plus the time required to deplete. The depletion time from IST theory is on the order $1/2\eta$ and for $\gamma_i \ll 2\eta$ this can be neglected and t_c gives the cycling time. By treating the damping and growth as a slow time scale perturbation of the IST soliton decay solution described above and ignoring the effects of diffusion on this short time scale, a multiple-time scale perturbation analysis about the IST soliton solution was used to estimate η' . In this calculation the ordering $\gamma_i \ll \gamma_j \ll 2\eta$ was chosen. The small parameter is $\gamma_j/2\eta$ but by simply rescaling in time and space either γ_j or η can be scaled to $O(1)$. To leading order this yields [15]:

$$\eta' \simeq \gamma_j. \quad (33)$$

The derivation assumes that the decay time for a soliton is very much faster than the growth and damping time. Simulations for parent soliton initial conditions verify Eq. (33) [15]. In order to complete the calculation for the cycling time t_c it is necessary to estimate the threshold local η required for decay. By comparing the Bohr quantization condition (21) with the WKB condition for decay with damping (31) we know that $\eta > \gamma_j$. Using the IST scattering space perturbation theory developed by Kaup [11, 28, 29] and recently reviewed in Ref. 30, we constructed the time dependence of the IST scattering data due to the perturbation. The same ordering as the

multiple scale calculation was chosen. From this we were able to estimate η to leading order to be [15]:

$$\eta \simeq 2\gamma_j + 4\xi_p\gamma_i \quad (34)$$

where ξ_p is the parent correlation length and will be defined later. Eq. (34) is sensitive to the amplitudes of the colliding daughter amplitude that induces the decay. The calculation assumes the decay is induced by collisions with quasi-solitons with the same phase from each daughter generated two correlation lengths away. The relative phases of the colliding daughters is very important. Consider real amplitudes for the moment, Eq. (28) shows that two daughter quasi-solitons with opposite signs (phase) actually reinforce the parent rather than make it deplete. Thus expression (34) should be considered more of a lower bound. In the simulation, radiation and diffusive effects will be relevant and may also further delay the decay of the parent. From η we are able to estimate the daughter correlation length. This is given by the quasi-soliton width $\xi_d \simeq 2/\eta$.

The long time behaviour is governed by the diffusion. The trivial fixed point of Eqs. (28–30) is given by:

$$\partial_{zz}a_i + q_0^2a_i = 0, \quad a_j = a_k = 0 \quad (35)$$

where $q_0 = \sqrt{\gamma_i/D}$. Modes with $q > q_0$ will damp and those with $q < q_0$ will grow. Thus the fixed point is always unstable to long wave length fluctuations. However, when a local area between two turning points of the parent wave contains a bound state with eigenvalue η it will deplete. In the depletion process broad parent pulses will be decimated. The growth in the $q < q_0$ modes are thus saturated nonlinearly. This results in long wavelength distortions beyond lengths $2\pi/q_0$. The principal mode q_0 was observed as the cutoff in the spectrum of static fluctuations (Fig. 3a). The mode q_0 defines the correlation length for the parent, $\xi_p \simeq 2\pi/q_0$. If $D = 0$ there will not be any nonlinear saturation of the instability because q_0 would become infinite and so would the amplitude required to fulfill the area threshold (31).

The long time scale for the parent τ_p is given by the diffusion time across a length ξ_p giving $\tau_p \simeq (2\pi)^2/\gamma_i$. This is the time scale in which the local parent structures will shift position, collide with other structures or diffuse away. The long correlation time observed in the daughters is associated with the interaction of the daughter quasi-solitons with the parent structures. Whenever quasi-solitons collide with the parent structures they may induce a decay and create a new quasi-soliton where the collision occurred. This would lead to a long correlation time for the daughters. As the parent structures drift so would the creation location of new quasi-solitons.

However because the quasi-solitons have a different width than the parent structures, the long time scale for the daughters would be given by the diffusion time across a quasi-soliton width yielding $\tau_d \simeq 4/(\eta^2 D)$. The newly created quasi-soliton damps while it continues to propagate along the characteristic. However when it collides with another parent structure it could induce a decay and repeat the process. The parent structures act as amplifiers regenerating damped quasi-solitons that collide with them.

Using the above analysis for the parameters of the simulation we obtain the following estimates: $\tau_p \simeq 400$, $q_0 = 10$, $\xi_p \simeq 0.6$, $\eta' \simeq 1$, $\eta \simeq 2.2$, $t_c \simeq 8$, $\xi_d \simeq 0.9$, $\tau_d \simeq 800$. These estimates corroborate fairly well with the simulation. The estimate for t_c is a bit low compared to the shoulder in the parent power spectra at $\omega \sim 0.3$ corresponding to $t \simeq 20$. However the spacetime profiles in Fig. 1 do show some of the parent structures cycling near the predicted time scale, so the calculation does predict a lower bound.

A word should be said about the system size. It is clear with the very long correlation times for the daughters that they cycle the box many times before correlations decay away. Thus for long times, the temporal correlation function along the characteristic or at a single spatial location would be the same. This was borne out in the simulation. It is unknown what the precise boundary effects are since it would be impossible to numerically test a system large compared to this long time scale. However with other runs of varying length, it was found that the above time scales seem to be unaffected by the box size as long as the box is much larger than ξ_p . The power law rise for the parent power spectrum below $2\pi/\tau_p$, seems to decrease in exponent as the system increases.

We chose parameters where perturbation theory about the IST solutions could be applied to try to understand the dynamics. However the behavior does dramatically change for different parameter regimes [15]. For strong growth rates, the long time scales observed tend to disappear and only the growth and depletion cycling time is evident. The parent grows strongly and depletes violently preventing the structures to become established. The larger the growth rate the larger the amplitudes of the quasi-solitons [15]. Another regime is when the diffusion is large so the parent structures are much broader than the damping length of the daughters. In this situation the daughters grow and damp within the confines of a parent pulse. Spatial exchange of information between these pulses is very slow. These and other regimes are reported in Ref. [15]. It is quite clear that the 3WI in spacetime is an extremely rich system. For weak growth and dissipation, it exhibits STC and perturbation theory is able to estimate the length and time scales.

ACKNOWLEDGEMENTS

One of us (C.C.) wishes to thank T. Hwa and D. Kaup for fruitful and interesting discussions. This work was supported in part by NSF Grant No. ECS-88-2475 and NASA Grant No. NAGW-2048.

REFERENCES

- [1] P. Bergé, Y. Pomeau, C. Vidal, *Order within Chaos*, (Hermann, Paris, 1984).
- [2] R. L. Devaney, *An Introduction to Chaotic Dynamical Systems*, (Addison-Wesley, Reading, Massachusetts, 1989).
- [3] C. S. Gardner, J. M. Greene, M. D. Kruskal and R. M. Miura, *Phys. Rev. Lett.* **19**, 1095 (1967).
- [4] M. J. Ablowitz, D. J. Kaup, A. C. Newell and H. Segur, *Stud. Appl. Math.* **53**, 249 (1974).
- [5] V. E. Zakharov and A. B. Shabat, *Zh. Eksp. Teor. Fiz.* **61**, 118 (1971) [*Sov. Phys. - JETP* **34**, 62 (1971)].
- [6] P. C. Hohenberg and B. I. Shraiman, *Physica D* **37**, 109 (1989) and references therein.
- [7] P. Coullet, C. Elphick, and D. Repaux, *Phys. Rev. Lett.* **58**, 431 (1987).
- [8] F. T. Arrechi, G. Giacomelli, P. L. Ramazza, and S. Residori, *Phys. Rev. Lett.* **65**, 2531 (1990).
- [9] S. Ciliberto and M. Caponeri, *Phys. Rev. Lett.* **64**, 2775 (1990).
- [10] R. Kraichnan, *Physica D* **37**, 160 (1989).
- [11] D. J. Kaup, A. Reiman, and A. Bers, *Rev. Mod. Phys.* **51**, 915 (1979) and references therein.
- [12] A. Bers, in *Plasma Physics - Les Houches 1972*, C. DeWitt and J. Peyraud, eds. (Gordon and Breach, New York, 1975).
- [13] D. J. Benney and A. C. Newell, *J. Math. Phys.* **46**, 133 (1967).
- [14] C. C. Chow, A. Bers, A. K. Ram, in *Research Trends in Chaotic Dynamics and Transport in Fluids and Plasmas* conference proceedings, LaJolla, CA, AIP 1991, in press.
- [15] Carson C. Chow, Ph.D. Thesis, M.I.T., 1991.
- [16] N. Bloembergen, *Nonlinear Optics*, (Bengamin, New York, 1965).
- [17] R. Z. Sagdeev and A. A. Galeev, *Nonlinear Plasma Theory*, (Benjamin, New York, 1969),
- [18] R. C. Davidson, *Methods in Nonlinear Plasma Theory*, (Academic, New York, 1972),
- [19] S. Y. Vyshkind and M. I. Rabinovich, *Zh. Eksp. Teor. Fiz* **71**, 557 (1976) [*Sov. Phys. - JETP* **44**, 292 (1976)].

- [20] J. Wersinger, J. Finn, and E. Ott, *Phys. Fluids* **23**, 1142 (1980).
- [21] C. Meunier, M. Bussac and G. Laval, *Physica* **4D**, 236 (1982).
- [22] D. J. Kaup, *Stud. Appl. Math.* **55**, 9 (1976).
- [23] V. E. Zakharov and S. V. Manakov, *Zh. Eksp. Teor. Fiz. Pis'ma Red.* **18**, 413 (1973) [*Sov. Phys. - JETP Lett.* **18**, 243 (1973)].
- [24] A. Bers, D. J. Kaup, and A. H. Reiman, *Phys. Rev. Lett.* **37**, 182 (1976).
- [25] A. Bers, in *Handbook of Plasma Physics*, M. N. Rosenbluth and R. Z. Sagdeev, eds. (North Holland, Amsterdam, 1983), Vol. 1, Chap. 3.2.
- [26] An equivalent set of 3WI equations can be written in two spatial dimensions (*e.g.* x and y) for nonlinear interactions in the steady state [11]; the equations are of the same form as Eqs. (28–30) where t is y and, in each equation, all other terms are divided by the y -component of the group velocity of the wave. Thus the solutions we describe (x, t) apply also to (x, y) with appropriate boundary conditions.
- [27] In the two-dimensional steady-state, see Ref. 26 above, this condition involves only the ratios of group velocity components.
- [28] D. J. Kaup, *SIAM J. Appl. Math.* **31**, 121 (1976).
- [29] D. J. Kaup and A. C. Newell, *Proc. R. Soc. Lond. A.* **361**, 413 (1978).
- [30] Y. S. Kivshar and B. A. Malomed, *Rev. Mod. Phys.* **61**, 763 (1989).

APPENDIX F

SPATIOTEMPORAL CHAOS IN THREE WAVE INTERACTIONS

C. C. CHOW, A. BERS AND A. K. RAM

Plasma Fusion Center and Research Laboratory of Electronics
 Massachusetts Institute of Technology, Cambridge, MA 02139 USA

ABSTRACT

It is shown that the saturated state of an unstable wave nonlinearly coupled to two lower frequency damped waves exhibits spatiotemporal chaos. The results can be understood by perturbation analysis on the conservative nonlinear three-wave interaction which is integrable.

KEYWORDS

Nonlinear wave interactions; unstable wave saturation; chaos in space-time

INTRODUCTION

The nonlinear three wave interaction (3WI) in spacetime has numerous applications to plasma physics (Bers, 1975; Kaup *et al.*, 1979). The linear evolution of this interaction describes parametric instabilities, both absolute and convective, as well as the stable coupling of waves. We consider the case of the nonlinear saturation of a linearly unstable parent wave by coupling to two damped daughter waves (Chow, 1991; Chow *et al.*, 1992a; Chow *et al.*, 1992b). This system exhibits spatiotemporal chaos (STC). The term STC specifically refers to the chaotic dynamics of coherent structures or spatial patterns (Hohenberg and Shraiman, 1989; Couillet *et al.*, 1987; Arrechi *et al.*, 1990; Ciliberto and Caponeri, 1990). This is contrasted with fully developed turbulence where there is a cascade to small scales, and is different from low dimensional chaos where spatial degrees of freedom are not involved. The conservative form of the 3WI is integrable by inverse scattering transforms (IST) and may have soliton solutions (Kaup *et al.*, 1979; Kaup, 1976a; Zakharov and Manakov, 1973). We consider the nearly integrable limit of the 3WI and use numerical simulations and perturbation theory about the IST solutions to gain some understanding of the dynamics.

The 3WI is a ubiquitous interaction that can occur whenever three linear waves are in resonance in a weakly nonlinear medium (Benney and Newell, 1967; Bers, 1975; Kaup, 1979; Chow, 1991). We studied the dynamics of a nonconservative 3WI in one spatial dimension x and time t . For weakly growing and damped waves this 3WI has the form (Chow, 1991; Chow *et al.*, 1992a)

$$\partial_t a_i - D \partial_{xx} a_i - \gamma_i a_i = -a_j a_k \quad (1)$$

$$\partial_t a_j + v_j \partial_x a_j + \gamma_j a_j = a_i a_k^* \quad (2)$$

$$\partial_t a_k + v_k \partial_x a_k + \gamma_k a_k = a_i a_j^*, \quad (3)$$

where the a 's are complex wave envelopes, the γ 's are growth or damping coefficients, v 's are group velocities (the interaction is described in the frame of the wave packets), the nonlinear coupling is taken as unity and D is a diffusion coefficient. The diffusion term is usually not included in the 3WI.

This term arises if we assume that the growth of the linear wave has a slow spatial variation. It is then the lowest order reflection invariant term that provides a cutoff in wave number of the growth. Without this term the problem is not well posed. It will become apparent later that this term is essential for nonlinear saturation and is very important in determining the long time behavior.¹ The subscript i denotes the high frequency unstable parent wave. The other two waves are referred to as the daughters. We will consider the case where the daughter waves have equal damping (i.e. $\gamma_j = \gamma_k$). The length and time can then be rescaled so that the damping coefficient is unity.

The order of the group velocities determines the behavior of the conservative ($\gamma = D = 0$) nonlinear interactions (Kaup *et al.*, 1979). If the high frequency wave has the middle group velocity then solitons are transferred from the parent to the daughter waves. This case is known as the soliton decay interaction (SDI). As an example, this situation may occur in the decay of lower hybrid waves. This also corresponds to the nonlinear saturation of an absolute parametric instability in the parent wave frame. If the parent wave has the highest or lowest group velocity then soliton exchange is no longer possible and the collisions between wave packets become important. This case is physically most common. It is the nonlinear saturation of a convective parametric instability in the parent frame. This situation applies for example to the Langmuir decay interaction (LDI) and may have implications in the saturation of stimulated Raman scattering (SRS) observed in intense laser-plasma interactions (Batha *et al.*, 1991). In the nonconservative nonlinear interaction described by (1)-(3) both SDI and LDI exhibit STC. The first is described in Section 2 and the second in Section 3.

SOLITON DECAY INTERACTION

For SDI the group velocities satisfy the condition $v_k > 0 > v_j$ (i.e., the highest frequency parent wave has the middle group velocity²). In the absence of growth, damping and diffusion ($\gamma_i = D = 0$) the IST solutions for this group velocity ordering is described by soliton exchange between wavepackets (Kaup *et al.*, 1979; Kaup, 1976a; Bers *et al.*, 1976).

We numerically simulated the system Eqs. (1)-(3) on the domain $x \in [0, L]$ with periodic boundary conditions. We began with random real initial conditions and evolved until the transients died away before the system was analyzed. It can be shown that for real valued initial conditions the envelopes remain real for all time (Kaup *et al.*, 1979; Chow, 1991). We were interested in the large system, long time limit. We considered the case with parameters $D = 0.001$, $\gamma_i = 0.1$, $\gamma_j = \gamma_k = 1$, and $L = 20$. These parameters were chosen because they exhibit STC and fall into a regime where the results can be understood by perturbation theory on the conservative solution. However, the system is extremely rich and different parameters do lead to vastly different behavior. Aspects of these different regimes will be touched upon later and details are given in (Chow, 1991). We measured the correlation function, $S_i(x, t) = \langle a_i(x - x', t - t') a_i(x', t') \rangle$, where the angled brackets denote spacetime averages.

A sample of the spatiotemporal evolution profiles in the STC regime of the parent and daughter envelopes is given in Fig. 1. The length shown is one half the system size and $t = 0$ is an arbitrary time well after the transients have decayed. The profile of the parent wave is irregular but spatial and temporal scales can be observed. There are coherent structures of a definite length scale that can be seen to grow, deplete and collide with one another. The profile of the daughter wave shows a sea of structures convecting to the left. We only show one daughter, the other will be similar but with structures convecting to the right. Figure 2 shows the spectrum of static fluctuations $S_i(t = 0, q)$. For the parent wave there is a cutoff near $q \simeq 10$ and a range of modes show up as

¹An equivalent set of 3WI equations can be written in two spatial dimensions (e.g. x and y) for nonlinear interactions in the steady state (Kaup *et al.*, 1979); the equations are of the same form where t is y and, in each equation, all other terms are divided by the y -component of the group velocity of the wave. Thus the solutions we describe (x, t) apply also to (x, y) with appropriate boundary conditions.

²In the two-dimensional steady-state, see (Kaup *et al.*, 1979) and (Benney and Newell, 1967), this condition involves only the ratios of group velocity components.

a prominent hump. The cutoff reflects the length scale seen in the spacetime profile. For q below the hump the spectrum is flat. The daughter spectrum has a cutoff around $q \simeq 6$ again indicating a length scale. Figure 3 shows the local power spectrum $S_i(\omega, x = 0)$. The spectrum for the parent clearly shows two time scales. The spectrum bends over near $\omega \simeq 0.02$ which gives a long time scale and a shoulder at $\omega \simeq 0.3$ gives a short time scale. The short time scale appears as the growth and depletion cycle observed in the spatiotemporal profile. The daughter power spectrum has two peaks at high ω . One is where the shoulder of the parent spectrum is and the other is at twice this frequency. The spectrum begins to bend over and flatten out at $\omega \simeq 0.007$.

The main features of the behavior can be understood if we consider the growth and dissipation as perturbations about the conservative 3WI. The IST solutions for the conservative case on the infinite domain show that solitons exist but they do not necessarily belong uniquely to a particular envelope. Solitons in the parent wave tend to deplete to solitons in the daughters which propagate away. The simplest soliton solution for decay shows that a soliton of the form $|a_i| = 2\eta \text{sech} 2\eta x$, will decay into solitons in the daughters of the form $|a_j| = \sqrt{2}\eta \text{sech} \eta(x + v_j t)$, where η is the IST spectral parameter for the Zakharov-Manakov (Zakharov and Manakov, 1973) scattering problem. The spectral parameter is also the eigenvalue for a bound state in the Zakharov-Shabat (Zakharov and Shabat, 1971) scattering problem with the parent pulse as the potential function. In the WKB limit η is related to the area of the parent pulse through the Bohr quantization condition

$$\int_a^b |a_i^2 - \eta^2|^{1/2} dx = \pi/2, \quad (4)$$

where $[a, b]$ are turning points for a local pulse. A collision between a daughter pulse and a parent soliton is necessary to induce the decay of the parent (Bers *et al.*, 1976; Kaup *et al.*, 1979). For arbitrary shaped parent pulses that exceed the area threshold, the soliton content will be transferred to the daughters leaving the radiation behind in the parent pulse. Collisions between daughter solitons are elastic.

With the addition of weak growth and dissipation, parent pulses deplete provided they satisfy the WKB threshold condition (Chow *et al.*, 1992a; Bers, 1983).

$$\int_a^b |a_i^2 - \gamma_j^2|^{1/2} dx > \pi/2. \quad (5)$$

The decay products in the daughters are quasi-solitons; they damp as they propagate away and do not collide elastically. The soliton content of the parent is not completely transferred to the daughters. The parent wave with some initial local eigenvalue η will deplete and be left with some remaining area. This area is due to the conversion of soliton content into radiation by the perturbations. This left over area can be represented by an effective 'eigenvalue' η' . This remaining part of the parent will then grow until it exceeds the threshold for decay. This time denoted by t_c is given by

$$t_c \simeq \frac{1}{\gamma_i} \ln \frac{\eta}{\eta'}. \quad (6)$$

The cycling time observed in the spacetime profiles is this time plus the time required to deplete. The depletion time from IST theory is on the order $1/2\eta$ and for $\gamma_i \ll 2\eta$ this can be neglected and t_c gives the cycling time. By treating the damping and growth as a slow time scale perturbation of the IST soliton decay solution described above and ignoring the effects of diffusion on this short time scale, a multiple-time scale perturbation analysis about the IST soliton solution was used to estimate η' . In this calculation the ordering $\gamma_i \ll \gamma_j \ll 2\eta$ was chosen. The small parameter is $\gamma_j/2\eta$ but by simply rescaling in time and space either γ_j or η can be scaled to $O(1)$. To leading order this yields (Chow, 1991)

$$\eta' \simeq \gamma_j. \quad (7)$$

The derivation assumes that the depletion time for a soliton is very much faster than the growth and damping time. Simulations for parent soliton initial conditions verify Eq. (7) (Chow, 1991). In order to complete the calculation for the cycling time t_c , it is necessary to estimate the threshold local η required for decay. By comparing the Bohr quantization condition (4) with the WKB condition for

decay with damping (5) we know that $\eta > \gamma_j$. Using the IST scattering space perturbation theory developed by Kaup (Kaup *et al.*, 1979; Kaup, 1976b; Kaup and Newell, 1978) and recently reviewed in Kivshar and Malomed (1989), we constructed the time dependence of the IST scattering data due to the perturbation. The same ordering as the multiple scale calculation was chosen. From this we were able to estimate η to leading order to be (Chow, 1991)

$$\eta \simeq 2\gamma_j + 4\xi_p\gamma_i, \quad (8)$$

where ξ_p is the parent correlation length and will be defined later. Equation (8) is sensitive to the amplitudes of the colliding daughter waves that induce the decay. The calculation assumes the decay is induced by collisions with quasi-solitons with the same phase from each daughter generated two correlation lengths away. The relative phases of the colliding daughters is very important. Consider real amplitudes for the moment, Eq. (1) shows that two daughter quasi-solitons with opposite signs (phase) actually reinforce the parent rather than make it deplete. Because of other effects, expression (8) should be considered more of a lower bound. In the simulation, radiation and diffusive effects will be relevant and may also further delay the decay of the parent. From η we are able to estimate the daughter correlation length. This is given by the quasi-soliton width $\xi_d \simeq 2/\eta$.

The long time behavior is governed by the diffusion. The trivial fixed point of Eq. (1) is given by

$$\partial_{xx}a_i + q_0^2a_i = 0, \quad a_j = a_k = 0, \quad (9)$$

where $q_0 = \sqrt{\gamma_i/D}$. Modes with $q > q_0$ will damp and those with $q < q_0$ will grow. Thus the fixed point is always unstable to long wave length fluctuations. However, when a local area between two turning points of the parent wave contains a bound state with eigenvalue η it will deplete. In the depletion process broad parent pulses will be decimated. The growth in the $q < q_0$ modes are thus saturated nonlinearly. This results in long wavelength distortions beyond lengths $2\pi/q_0$. The principal mode q_0 was observed as the cutoff in the spectrum of static fluctuations (Fig. 2a). The mode q_0 defines the correlation length for the parent, $\xi_p \simeq 2\pi/q_0$. If $D = 0$ there will not be any nonlinear saturation of the instability because q_0 would become infinite and so would the amplitude required to fulfill the area threshold (5).

The long time scale for the parent τ_p is given by the diffusion time across a length ξ_p giving $\tau_p \simeq (2\pi)^2/\gamma_i$. This is the time scale in which the local parent structures will shift position, collide with other structures or diffuse away. The long correlation time observed in the daughters is associated with the interaction of the daughter quasi-solitons with the parent structures. Whenever quasi-solitons collide with the parent structures they may induce a decay and create a new quasi-soliton where the collision occurred. This would lead to a long correlation time for the daughters. As the parent structures drift so would the creation location of new quasi-solitons. However because the quasi-solitons have a larger width than the parent structures, the long time scale for the daughters would be given by the diffusion time across a quasi-soliton width yielding $\tau_d \simeq 4/(\eta^2 D)$. The newly created quasi-soliton damps while it continues to propagate along the characteristic. However when it collides with another parent structure it could induce a decay and repeat the process. The parent structures act as amplifiers regenerating damped quasi-solitons that collide with them.

Using the above analysis for the parameters of the simulation we obtain the following estimates: $\tau_p \simeq 400$, $q_0 = 10$, $\xi_p \simeq 0.6$, $\eta' \simeq 1$, $\eta \simeq 2.2$, $t_c \simeq 8$, $\xi_d \simeq 0.9$, $\tau_d \simeq 800$. These estimates corroborate fairly well with the simulation. The estimate for t_c is a bit low compared to the shoulder in the parent power spectra at $\omega \sim 0.3$ corresponding to $t \simeq 20$. This is because many effects due to radiation, diffusion and strong overlap of the envelopes were not accounted for. However the spacetime profiles in Fig. 1 do show some of the parent structures cycling near the predicted time scale, so the calculation does predict a lower bound.

A word should be said about the system size. It is clear with the very long correlation times for the daughters that they cycle the box many times before correlations decay away. Thus for long times, the temporal correlation function along the characteristic or at a single spatial location would be the same. This was born out in the simulation. It is unknown what the precise boundary effects

are since it would be impossible to numerically test a system large compared to this long time scale. However with other runs of varying length, it was found that the above time scales seem to be unaffected by the box size as long as the box is much larger than ξ_p . The power law rise for the parent power spectrum below $2\pi/\tau_p$, seems to decrease in exponent as the system increases.

We chose parameters where perturbation theory about the IST solutions could be applied to try to understand the dynamics. However the behavior does dramatically change for different parameter regimes (Chow, 1991). For growth rates not small compared to the damping rates, the long time scales observed tend to disappear and only the growth and depletion cycling time is evident. The parent grows strongly and depletes violently preventing the structures to become established. The larger the growth rate the larger the amplitudes of the quasi-solitons (Chow, 1991). Another regime is when the diffusion is comparable to the damping so the parent structures are much broader than the damping length of the daughters. In this situation the daughters grow and damp within the confines of a parent pulse. Spatial exchange of information between these pulses is very slow. These and other regimes are reported in Chow (1991).

LANGMUIR DECAY INTERACTION

In LDI the group velocities satisfy, without loss of generality, $v_k < v_j < 0$. For the simulation the values $v_j = -1, v_k = -2$ were chosen. Using laser plasma terminology, wave a_i is referred to as the pump wave (PW), wave a_j is the acoustic wave (AW) and wave a_k is the backscattered wave (BW). The Eqs. (1)-(3) were simulated on the domain $x \in [0, L]$ with periodic boundary conditions. The long time, large system limit was of interest. Simulations were started with random real initial conditions. As in the SDI case the envelopes remain real for all time. The spacetime history was recorded for all the envelopes. In the saturated regime the correlation functions $S_i(x, t) = \langle a_i(x - x', t - t') a_i(x', t') \rangle$ were computed. As in SDI the parameter set is given by (D, γ_i) .

Several different parameter sets were used in the simulations. In the first example the parameters were: $\gamma_i = 0.1$, $D = 0.004$ and $L = 20$. As will be seen later the length plays an important role in the dynamics. The spatiotemporal profile of the PW is shown in Fig. 4a. Again furrowed, ridgelike 'coherent' structures are observed, as in the SDI but with a definite drift towards the right. There appear to be length and time scales where things are correlated, but beyond which the dynamics becomes chaotic. The correlation function for the PW is shown in Fig. 4b. The function approaches zero in space and time indicating STC but a nonlinearly induced mode with a definite phase velocity is clearly observed. This effect was observed in the spacetime profiles as the drifting coherent structures. The correlation function shows that these structures are very long lived.

The local power spectrum $S_i(x = 0, \omega)$ is shown in Fig. 5a. A definite peak at $\omega \simeq .1$ is observed; the spectrum then flattens out at around $\omega \simeq 0.007$ defining a correlation time. The spectrum of static fluctuations $S_i(q, t = 0)$ is shown in Fig. 5b. A box-like function, as expected, is observed with a cutoff at approximately $q \simeq 5$, translating to a correlation length of $\xi_p \simeq 1.3$.

The spacetime profile of the AW is shown in Fig. 6a. Ridgelike coherent structures are seen to drift towards the left. For large scales the dynamics are chaotic. The correlation function measured along the characteristic $x = -t$ is given in Fig. 6b. There is strong decay in space and time confirming STC. However there is a hump located at $S(x \simeq 10, t \simeq 10)$, and another at $S(x \simeq 1, t \simeq 20)$. The latter is due to the collision of the AW coherent structure after one transit around the box. Because the PW is drifting the bump is located away from $x = 0$. The former bump comes from the interaction of the BW with the PW generating the AW. Since the BW travels at twice the AW velocity this event occurs at half the time the AW requires to traverse the box. Note that the correlation function shown is over the entire length of the system, and the periodicity of the system is seen for $t = 0$. The power spectrum is shown in Fig. 7a. The correlation time corresponds to a frequency of $\omega \simeq 0.3$. The spectrum of static fluctuations is shown in Fig. 7b. There is a cutoff at $q \simeq 9$ corresponding to a correlation length of $\xi_a \simeq 0.7$.

The spacetime profile of the BW is shown in Fig. 8a. Again irregular yet distinct structures are seen to drift towards the left. The correlation function measured along the characteristic $x = -2t$ is shown in Fig. 8b. Correlations approach zero in space and time indicating STC. A nonlinear mode similar to the parent is also observed. The propagating mode implies that the structures found in Fig. 8a are not aligned along the characteristic curve but are actually moving faster. The measured phase velocity in the moving frame $v \simeq 0.1$ indicates that the shift away from the characteristic velocity is not very great. Correlations in the direction of the coherent structures are fairly long compared to the damping times. The power spectrum along the characteristic in Fig. 9a shows a cutoff around $\omega \simeq 0.4$. The spectrum of static fluctuations in Fig. 9b shows a cutoff around $q \simeq 5$ giving a correlation length of $\xi_b \simeq 1.3$.

The simulation results can be understood with the aid of linear analysis and the IST solutions. The linearized equation for the PW is exactly the same as that for the parent wave in SDI. The trivial fixed point Eq. (9) gives a principal mode for the PW at $q_0 = \sqrt{\gamma_i/D}$. Higher modes are damped and lower modes are growing. As in SDI there is a competition between linear growth and nonlinear saturation. Instead of depletion to quasi-solitons seen in SDI, the saturation mechanism is due to the collisions between the envelopes. The balance between the competing effects is also responsible for the propagating mode as will be shown.

The IST solutions which apply to the conservative form of LDI show solitons are not involved (Kaup *et al.*, 1979). The interesting dynamics are due to collisional radiation effects. A collision between the AW and the PW generates the BW and decimates all the waves (Kaup *et al.*, 1979; Chow, 1991). Similar behavior occurs when the BW collides with the PW. The decimation of the parent wave is always on the side opposite to that of the collision. This is seen in the IST solutions and can be understood from the nonlinear saturation of the corresponding parametric instability. When the AW collides with the PW, the BW and AW grow from the colliding edge as a convective instability. This is because both of their group velocities are in the same direction. When the two envelopes attain a significant amplitude the PW begins to saturate. However the two daughter waves will continue to grow and continue to take energy from the PW. The energy of the PW will be reduced. The depleting pump cuts off the growth of the two daughter waves and they saturate and begin to damp as well. If the original amplitude of the PW is large enough or the growth rate γ_i high enough, the reduction in area continues until the PW becomes negative. The negative part of the PW can again be a source for a convective instability and the same process ensues. In this way the envelopes are spatially decimated into the oscillatory structures seen in the simulation. The decimation is always on the side of the PW away from the colliding edge. The low q 's are converted to high q 's by this process. Modes higher than q_0 get damped, so the PW will settle into structures of size $\xi_p \simeq 2\pi/q_0$. The values $q_0 = 5$ and $\xi_p \simeq 1.3$, obtained for the simulation parameter set, agree well with the simulation.

The PW equation Eq. (1) has the form of a growing diffusion equation. Thus any localized pulse will spread and grow. The propagating PW mode is a result of the combination of this spreading effect and the decimation effect. The wavepackets decimate nonlinearly on one side and they spread and grow linearly on the other side. A pulse moves like a sandbar near an ocean shore, building on one side and receding on the other. A parabolic equation does not have a well defined phase velocity, but a 'spreading' velocity can be defined by considering the trajectory of a point of constant amplitude on a localized pulse. The phase velocity of the sandbar mode, as it will be referred to, will then be given by this velocity which can be shown to be proportional to $\sqrt{D\gamma_i}$ (Chow, 1991). From the simulations of several different cases it was discovered that the phase velocity behaves as $v_p \simeq \sqrt{D\gamma_i}$.

The peak in the PW power spectrum is given by the frequency of the sandbar mode. Using the relation $\omega = v_p q_0$ the frequency is found to be $\omega \simeq \gamma_i = .1$. This is precisely what was observed in Fig. 5a. As seen in the correlation function in Fig. 4b, the structures remain coherent for very long times. The power spectrum in Fig. 5a was taken along the time axis. The long time scale

observed was actually given by the transit time of the sandbar mode around the box $\tau_P \simeq L/v_P$. It is unknown what the decorrelation mechanism for the PW coherent structures actually is. They persist much longer than the diffusion time across a correlation length.

The saturation energy of the PW can be understood as follows. The competition between the nonlinear and linear effects leads to coherent structures of size $2\pi/q_0$. The IST solutions show for the conservative case that structures of this size are generated in collisions when the PW has a height of $a_i \simeq q_0$. For taller structures, the collisions with the BW and AW will generate structures with smaller wavelengths. The simulations seemed to indicate that these results of the integrable case carry over to the nonintegrable regime. Then as the PW grows, it gets depleted as it constantly collides with the other waves. If it grows higher than $a_i \simeq q_0$ the generated structures damp away. Thus $a_i \simeq q_0$ will be an upper bound to the height of the PW. For these parameters $q_0 \simeq 5$ and the tallest structures in the spacetime profile are of this order. Given the upper bound for the PW height, the saturated energy density can be estimated by considering the PW to be composed of coherent structures locally resembling a sine wave with average amplitude of $q_0/2$. This then gives an average energy density of $S_i(0,0) \simeq q_0^2/4 \simeq 6$. The simulation shows a value of $S_i(0,0) \simeq 5$. Considering the assumptions used in the estimate this is remarkably good.

It is significant that the correlation length for the AW is one half the correlation length of the BW. This is due to the fact that its group velocity is half of the BW. As discussed above the PW settles into coherent structures of size ξ_p , and this fixes the size of the BW structures. The AW gets generated wherever the BW collides with the PW. In the time direction, along a PW coherent structure, the BW and AW will tend to have the same number of coherent structures. This can be seen by comparing Fig. 6a with Fig. 8a. However since the AW has a group velocity half that of the BW, if it has the same number of structures in the time direction, it must have twice as many in the spatial direction. In other words the coherent structures of the AW are half the size of the BW. This was observed in the simulation. In the saturated state, a lattice-like structure will become established. Of course it is only for special cases that a regular lattice can be formed. In most cases the lattice will be frustrated. This leads to the lack of regularity and STC observed. It would be very useful in the future to measure the cross correlation function between the waves to better understand these effects.

The propagating mode of the BW seen in the correlation function can also be inferred from the IST solution. The correlation function showed that the propagation velocity of the coherent structures was slightly slower than the characteristic velocity. During a collision between the BW with the PW, the two waves will interact nonlinearly and this process retards the transmission of the BW, slowing the velocity.

The AW spacetime profile in Fig. 6a shows a furrowed structure moving to the left like the BW, but the correlation function in Fig. 8a does not show the long correlations and evidence of a nonlinear mode like the BW and PW. Correlations are quickly damped out compared to the other waves. This is likely due in part to the fact that since the group velocity is half that of the BW, it experiences twice as much damping between collisions. It may also be that the wave collisions affect the AW more than the other waves. The humps observed in the AW correlation function are due to collisions of the AW with the PW and BW waves. The one at $(x \simeq 1, t \simeq 20)$, is due to repeated collisions of the AW with a particular PW structure. The correlation times of the PW structures are very long. Each time the AW circles the simulation box it will collide with the PW structure. The hump is slightly off from the characteristic. This is due to the fact that the PW structure is drifting. The hump at $(x \simeq 10, t \simeq 10)$ is due to collisions between a given BW structure and the PW structure. Whenever these two waves collide they generate the AW in the process. The BW has group velocity twice that of the AW and so transits the box in a time $t = 10$. In the frame of the AW the hump gets shifted in x as well.

It would seem that the behavior observed for LDI should persist as the PW growth rate increases or the diffusion decreases. The PW structures would reduce in width and this would lead to an increase in their amplitude. The ratio of the PW energy to the daughters would approach unity. However in the weak growth limit the ratio of the PW energy to the daughter energies would be large. The PW structures would become wider and their amplitudes smaller. The daughter waves would damp more between collisions. The coherence times would likely become longer as in the SDI case. The energies of the daughter waves would also get smaller in comparison to the PW's and the nonlinearity would become less important. Differences in the ratios of the velocity would change the ratio of the sizes of the AW and BW. Differences in the damping rates on the daughters would change the saturation energies. If the disparity were large than the wave with the lower damping would dominate the nonlinear collision processes. These effects were seen in preliminary simulations. A detailed analysis remains to be done.

The spectral broadening and amplitude saturation of the unstable wave occurs for almost all parameters. As an application we have considered the saturation of SRS due to decay of the electron plasma wave (epw) (Chow, 1991). The unstable epw in SRS can decay rapidly to another epw and ion-acoustic wave. The ensuing STC broadens the spectrum and saturates this epw which, for a fixed input laser power, leads to the saturation of the scattered wave in SRS. Further details will be given in an upcoming publication.

One of us (C.C.) wishes to thank T. Hwa and D. Kaup for fruitful and interesting discussions. This work was supported in part by NSF Grant No. ECS-88-2475, LLNL subcontract B160456, DOE Grant No. DE-FG02-91ER-54109, and NASA Grant No. NAGW-2048.

REFERENCES

- Arrechi, F. T., G. Giacomelli, P. L. Ramazza, and S. Residori (1990). *Phys. Rev. Lett.*, **65**, 2531.
- Batha, S. H., D. S. Montgomery, K. S. Bradley, R. P. Drake, K. Estabrook, and B. A. Remington (1991). *Phys. Rev. Lett.*, **66**, 2324.
- Benney D. J. and A. C. Newell (1967). *J. Math. Phys.*, **46**, 133.
- Bers, A. (1975). In: *Plasma Physics-Les Houches 1972*, eds. C. De Witt and J. Peyraud (Gordon and Breach, New York).
- Bers, A. (1983). In: *Handbook of Plasma Physics*, eds. M. N. Rosenbluth and R. Z. Sagdeev (North Holland, Amsterdam, 1983), Vol. 1, Chap. 3.2.
- Bers, A., D. J. Kaup, and A. H. Reiman (1976). *Phys. Rev. Lett.*, **37**, 182.
- Chow, C. C. (1991). Ph.D. Thesis, Department of Physics, Massachusetts Institute of Technology, Cambridge, Mass., USA.
- Chow, C. C., A. Bers, and A. K. Ram (1992). in *Research Trends in Physics: Chaotic Dynamics and Transport in Fluids and Plasmas* eds. I. Prigogine et al. (American Institute of Physics, New York).
- Chow, C. C., A. Bers, and A. K. Ram (1992). *Phys. Rev. Lett.*, **68**, 3379.
- Ciliberto, S. and M. Caponeri (1990). *Phys. Rev. Lett.*, **64**, 2775.
- Coullet, P., C. Elphick, and D. Repaux (1987). *Phys. Rev. Lett.*, **58**, 431.
- Hohenberg, P. C. and B. I. Shraiman (1989). *Physica D*, **37**, 109 and references therein.
- Kaup, D. J. (1976). *Stud. Appl. Math.*, **55**, 9.
- Kaup, D. J. (1976). *SIAM J. Appl. Math.*, **31**, 121.
- Kaup, D. J., A. Reiman, and A. Bers (1979). *Rev. Mod. Phys.*, **51**, 915 and references therein.
- Kaup, D. J. and A. C. Newell (1978). *Proc. R. Soc. Lond. A.*, **361**, 413.
- Kivshar, Y. S. and B. A. Malomed (1989). *Rev. Mod. Phys.*, **61**, 763.
- Remington, B. A. (1991). *Phys. Rev. Lett.*, **66**, 2324.
- Zakharov, V. E. and S. V. Manakov (1973). *Zh. Eksp. Teor. Fiz. Pis'ma Red.* **18**, 413 [*Sov. Phys.,—JETP Lett.*, **18**, 243].
- Zakharov, V. E. and A. B. Shabat (1971). *Zh. Eksp. Teor. Fiz.*, **61**, 118 [*Sov. Phys.,—JETP* **34**, 62].

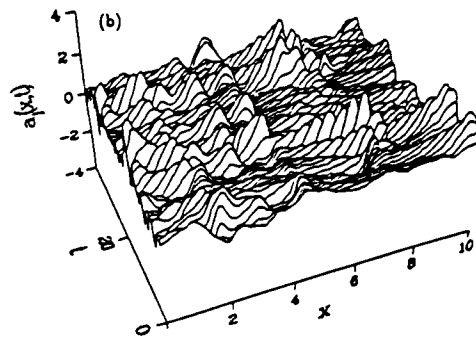
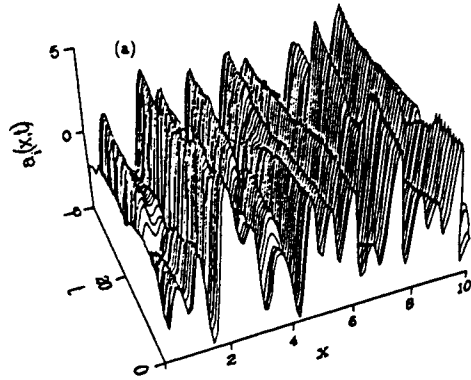


Fig. 1. Spatiotemporal profiles of the parent wave a) and daughter wave b) for SDI.

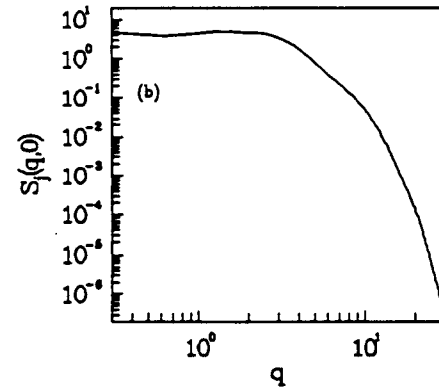
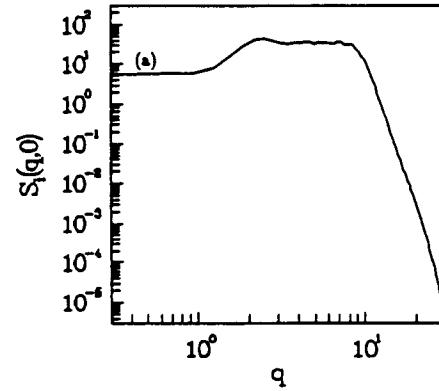


Fig. 2. Spectrum of static fluctuations $S_l(q, t = 0)$ of the parent wave a) and daughter wave b) for SDI.

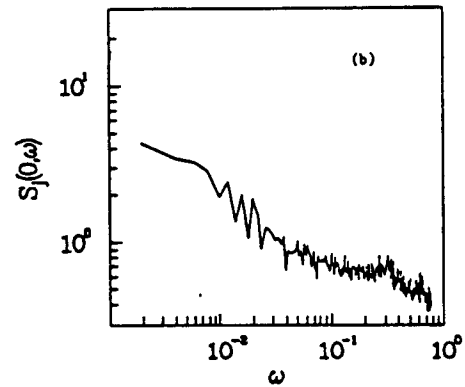
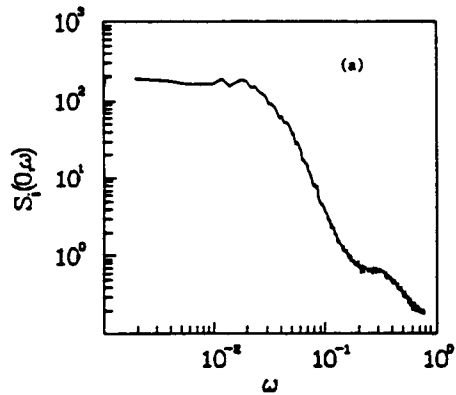


Fig. 3. Local power spectrum $S_l(x = 0, \omega)$ of the parent wave a) and daughter wave b) for SDI.

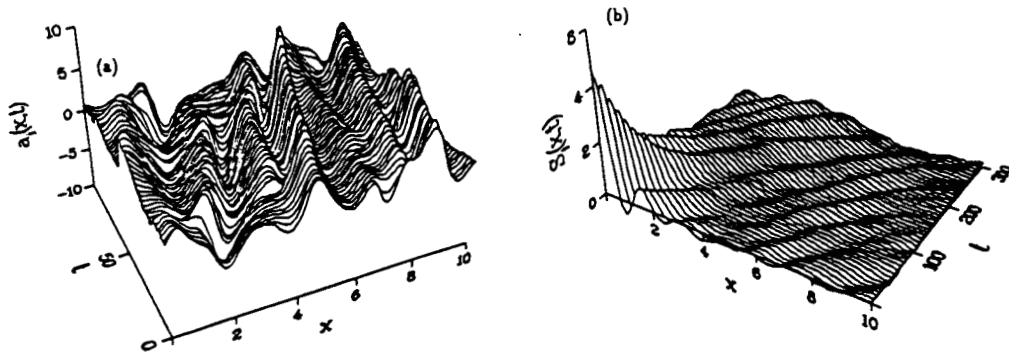


Fig. 4. Spatiotemporal profile a) and correlation function b) of the PW for LDI.

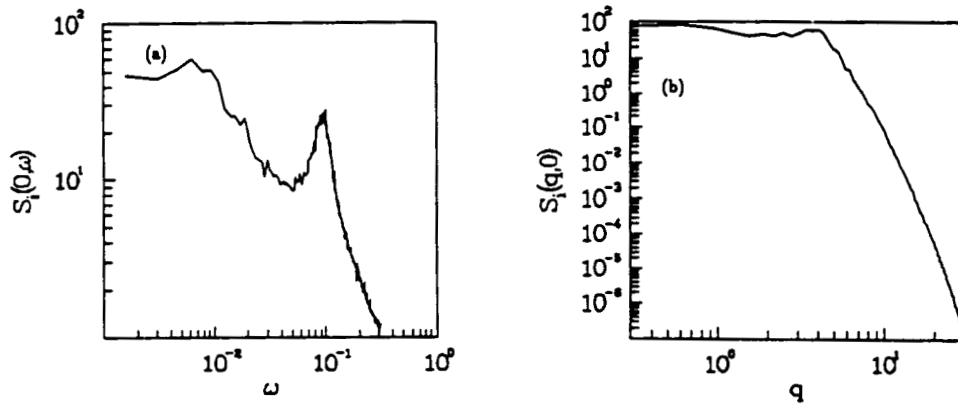


Fig. 5. Local power spectrum a) and spectrum of static fluctuations b) for the PW for LDI.

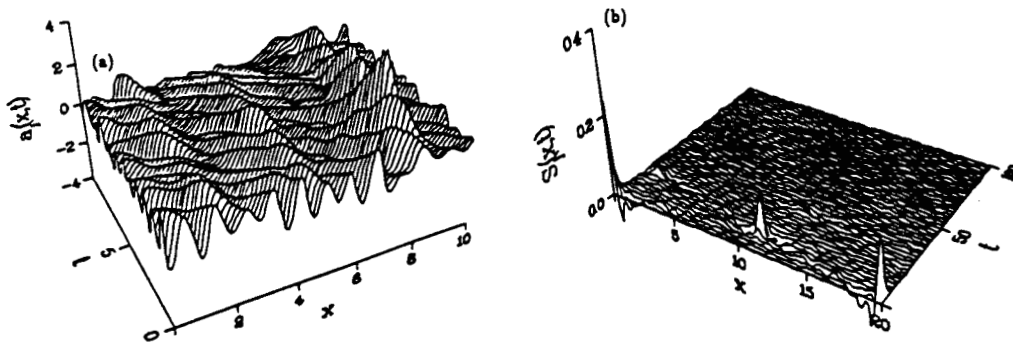


Fig. 6. Spatiotemporal profile a) and correlation function b) of the AW for LDI.

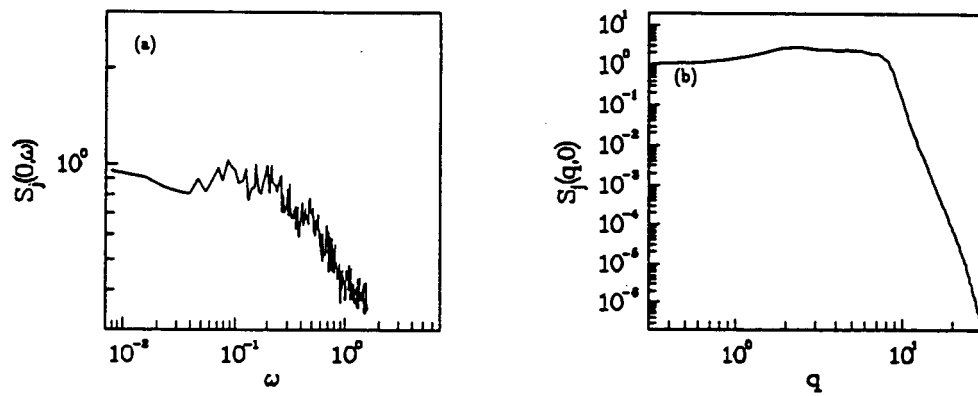


Fig. 7. Local power spectrum a) and spectrum of static fluctuations b) for the AW for LDI.

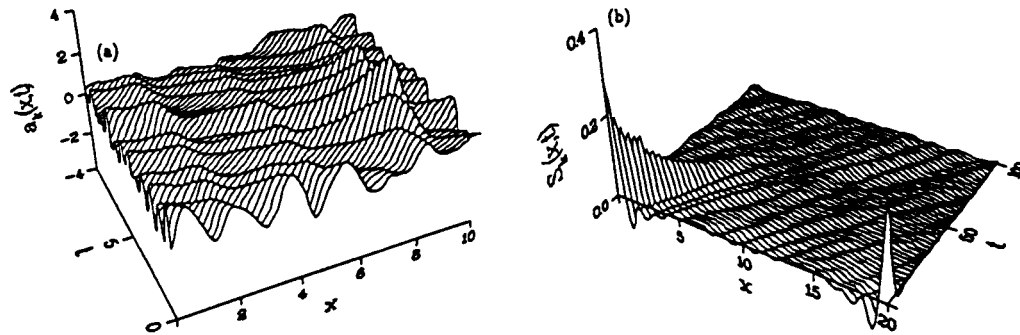


Fig. 8. Spatiotemporal profile a) and correlation function b) of the BW for LDI.

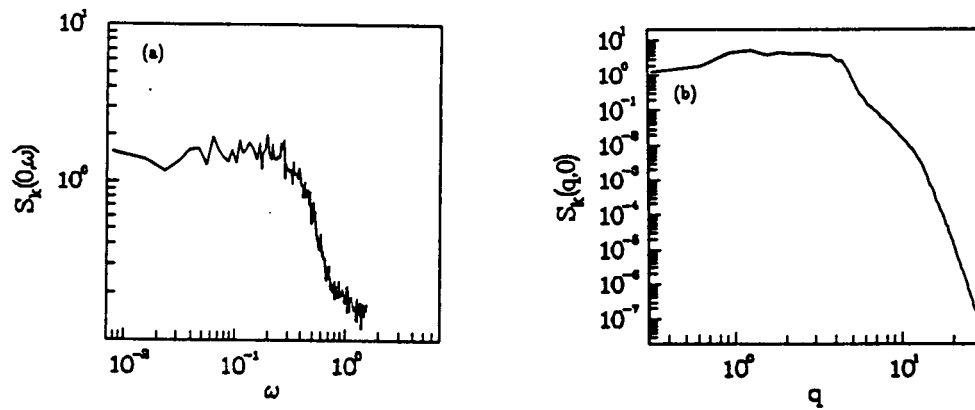


Fig. 9. Local power spectrum a) and spectrum of static fluctuations b) for the BW for LDI.

Series Editor: T. S. Chang

APPENDIX G

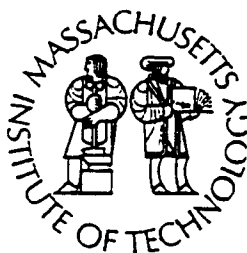
PHYSICS OF SPACE PLASMAS *(1993)*

*Proceedings of the
1993 Cambridge Workshop in Geoplasma Physics and
1993 MIT Symposium on the Physics of Space Plasmas
"Chaos, Stochasticity, and Strong Turbulence"*

—NUMBER 13—

EDITORS

T. Chang and J. R. Jasperse



MIT Center For Theoretical
Geo/Cosmo Plasma Physics

HAMILTONIAN CHAOS IN WAVE-PARTICLE INTERACTIONS

Abhay K. Ram, Abraham Bers
Plasma Fusion Center and Research Laboratory of Electronics
Massachusetts Institute of Technology
Cambridge, MA 02139 U.S.A.

ABSTRACT

Wave-particle interactions are an integral part of plasma dynamics in space and laboratory plasmas. In this tutorial we discuss the motion of charged particles under the influence of waves when the particle dynamics is assumed to be dissipation-free so that it can be described by a Hamiltonian. Distinguishing features between chaotic and coherent particle motion are illustrated pictorially using paradigmatic models describing the interaction of particles with prescribed waves.

INTRODUCTION

The microdynamics of high temperature plasmas are generally described by wave-particle interactions on time-scales for which collisions can be neglected. The waves may be internally generated by some plasma instability or can be coupled into the plasma from an external electromagnetic source. In the case of a plasma microinstability, one saturation mechanism for the instability arises from the resonant interaction of its unstable fields with the charged particles in the plasma: the particles gain energy and/or momentum from these fields and, as a consequence, their distribution functions are modified. In the case of externally coupled waves, as occurs for heating plasmas or driving currents in plasmas, charged particles interacting resonantly with these waves similarly remove energy and/or momentum from the wave and in this process their distribution functions are also modified. It is well-known that the interaction of plasma particles with randomly phased waves can lead to irreversible changes in the particle's distribution function (quasilinear dynamics in the random phase approximation). The importance of Hamiltonian chaos is that the interaction of coherent waves with plasma particles can also lead to an essentially irreversible change in the distribution function of the particles. In general, a modification to the distribution function of the particles may lead to changes in the wave propagation properties of the plasma, thereby requiring a self-consistent treatment of wave-particle interactions. However, in numerous situations of physical interest the waves interact with a small number of energetic particles so that the bulk of the distribution function, which determines the wave propagation properties, is essentially unaffected.

In this tutorial we describe some characteristic nonlinear aspects of wave-particle interactions in which the waves are assumed to be coherent and completely prescribed *ab initio*, and the particle motion is described by a Hamiltonian (*i.e.* collisionless dynamics).

The motion of charged particles interacting with coherent electromagnetic waves in a plasma can exhibit a rich and interesting behavior. In particular, for appropriate conditions, the motion of a particle can become chaotic. In this tutorial we describe important characteristics of this chaotic motion and compare them with the case when the particle motion is not chaotic, *i.e.* when it is predictable. In assuming that the waves are prescribed, their amplitude, frequency, and wavelengths are given and do not evolve with time. The interaction between the charged particles and the waves is taken to be dissipation-free so that there are no other sinks or sources of energy or momentum. Thus, the interaction is conservative and the motion of a particle can be described by a Hamiltonian. A very important aspect of such systems is that volume elements in phase space are conserved, *i.e.* the flow in phase space is incompressible. This is a consequence of Liouville's theorem. Hence, there do not exist any phase-space attractors – strange or otherwise – and one is forced to study the entire phase space spanned by the Hamiltonian system. While this may seem like a daunting task there exist criteria which determine regions of phase space where, for instance, the motion of particles becomes chaotic.

In the description of particle dynamics that follows, we have tried to avoid getting involved in detailed mathematical analysis. Rather, we illustrate properties of Hamiltonian dynamics pictorially, based on the computations of actual particle orbits, and outline some of the mathematical aspects that help in understanding these nonlinear dynamics. We have chosen the so-called standard map as a paradigm to illustrate in detail properties of chaotic dynamics. In addition, we discuss the motion of particles in a magnetic field being acted upon by an electrostatic wave propagating transverse to the magnetic field. This is of relevance to a large variety of laboratory and space plasmas. While we are not aware of any prior work which has the detailed pictorial illustrations given in this tutorial, there do exist two excellent publications [1-3] to which we refer the reader for more mathematical details.

I. MOTION OF A CHARGED PARTICLE IN AN ELECTROSTATIC WAVE

The one-dimensional motion of a charged particle of mass m and charge e in a plane electrostatic travelling wave of amplitude E , wave number k and frequency ω is given by the Lorentz equation:

$$\frac{dx}{dt} = v \tag{1a}$$

$$\frac{dv}{dt} = \frac{eE}{m} \sin(kx - \omega t) \quad (1b)$$

where x and v are the position and velocity of the particle, respectively, and t is time. In the frame moving with the phase velocity of the wave, ω/k , the above equations become:

$$\frac{dq}{d\tau} = p \quad (2a)$$

$$\frac{dp}{d\tau} = \alpha \sin(q) \quad (2b)$$

where $\tau = \omega t$ is the normalized time, $p = kv/\omega - 1$ is the particle velocity in the wave frame normalized to the phase velocity, $q = kx - \omega t$ is the position of the particle in the wave frame normalized to the wave number, and $\alpha = eEk/(m\omega^2)$ is the normalized amplitude of the wave (the square of the particle's bounce frequency near the bottom of the potential well of the wave divided by the square of the wave frequency). These equations of motion are identical to those of a nonlinear oscillator whose solutions are well-known [Appendix A]. From (2a) and (2b) it can be easily shown that the energy $H(q, p) = p^2/2 + \alpha \cos(q)$ (which is the Hamiltonian for the above equations of motion) is a constant of the motion. Thus, for a given initial condition, the motion of a particle will lie on a surface of constant $H(q, p)$ with the constant being determined by the initial conditions. The projection of such surfaces onto the $q - p$ plane are shown in Fig. 1. The phase space for the motion of the particles can be divided into two regions: $|H| \leq \alpha$, and $H > \alpha$. The surface $H = \alpha$ dividing the two regions is known as the "separatrix". The phase-space region given by $|H| \leq \alpha$ corresponds to particles trapped in the wave potential, while the region given by $H > \alpha$ corresponds to untrapped, or passing, particles (Fig. 1). The trapping width $\Delta p_{tr} = 2\sqrt{\alpha}$ gives half the extent in velocity space of the trapped particle region (Fig. 1).

For a particle that is initially at $p_0 = 0$ and $q_0 = \pi$, we see from Eqs. (2a, 2b), that it is unaffected by the wave. This is a particle at the bottom of the wave potential. This point in phase space is known as a "fixed" point. Consider a particle in the vicinity of this fixed point with $q = \pi + \bar{q}$, $p = \bar{p}$, where $|\bar{q}|$, $|\bar{p}| \ll 1$. Then the constant energy surface on which this particle moves is given by:

$$\frac{\bar{p}^2}{2\alpha} + \frac{\bar{q}^2}{2} = \text{constant} \quad (3)$$

where the constant on the right hand side is given by the initial conditions. The above equation describes an ellipse in phase space and, consequently,

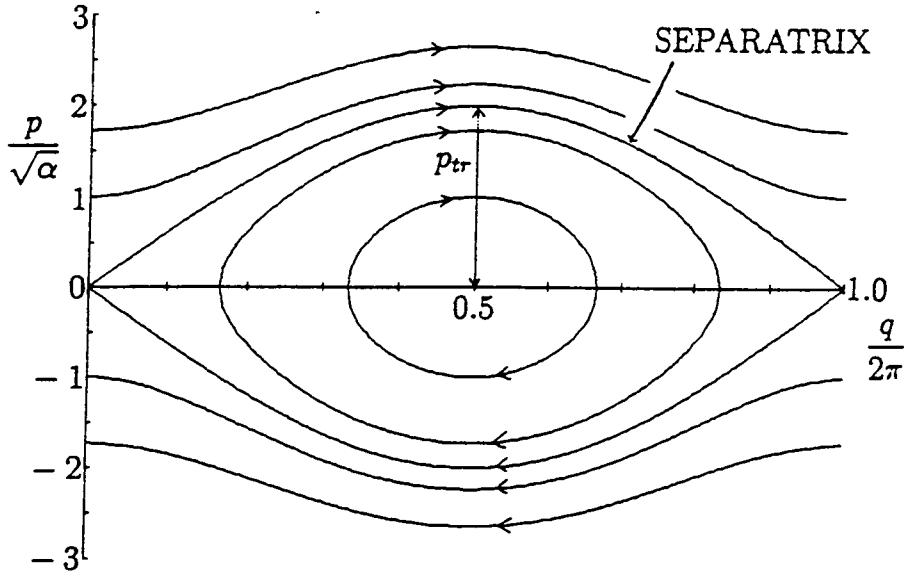


Figure 1. Surfaces of constant energy for the nonlinear oscillator showing the trapping width, p_{tr} , trapped motion, untrapped motion, and the separatrix.

the fixed (q_0, p_0) is known as an "elliptic" fixed point. Solving Eqs. (2a, 2b) in the vicinity of the fixed point (q_0, p_0) shows that motion is oscillatory with a frequency of $\sqrt{\alpha}$. Thus, a particle in the vicinity of this fixed point will remain in its vicinity for subsequent times. This is apparent from Fig. 1.

From Eqs. (2a, 2b) we find that a particle that is initially at $p_1 = 0$ and $q_1 = 0$ will also not be affected by the wave for subsequent times. Hence, this is also a fixed point. Consider a particle in the vicinity of this fixed point with $q = \bar{q}$, $p = \bar{p}$, where $|\bar{q}|, |\bar{p}| \ll 1$. Then the constant energy surface on which this particle moves is given by:

$$\frac{\bar{p}^2}{2\alpha} - \frac{\bar{q}^2}{2} = \text{constant} \quad (4)$$

where the constant on the right hand side is given by the initial conditions. This is an equation for a hyperbola and, consequently, the fixed point at $(q, p) = (0, 0)$ is known as a "hyperbolic" fixed point. The asymptotes of this hyperbola are: $\bar{p}/\sqrt{\alpha} = \pm \bar{q}$. Solving Eqs. (2a, 2b) in the vicinity of the hyperbolic fixed point give:

$$\bar{q} = c_0 e^{\sqrt{\alpha}t} + c_1 e^{-\sqrt{\alpha}t} \quad (5a)$$

$$\bar{p} = c_0 \sqrt{\alpha} e^{\sqrt{\alpha}t} + c_1 \sqrt{\alpha} e^{-\sqrt{\alpha}t} \quad (5b)$$

where c_0 and c_1 are constants determined by the initial conditions. These results show that, for small displacements of a particle away from the hyperbolic fixed point, along the asymptote $\bar{p}/\sqrt{\alpha} = \bar{q}$ the particle moves at an initially exponential rate away from the hyperbolic fixed point. This asymptote is known as the “unstable manifold”. For small displacements of a particle away from the hyperbolic fixed point along the asymptote $\bar{p}/\sqrt{\alpha} = -\bar{q}$, the particle approaches the hyperbolic fixed point at an exponentially slow rate. This asymptote is known as the “stable manifold”. The motion of a particle in the vicinity of the hyperbolic fixed point and the existence of the two manifolds is apparent from Fig. 1. Furthermore, Fig. 1 also shows that the stable and unstable manifolds overlap completely.

For periodic systems of the type discussed above, it is useful to define another set of coordinates — the action (I)-angle (θ) coordinates [4], where $0 \leq \theta < 2\pi$. For the nonlinear oscillator these coordinates are given in Appendix B. The advantage of this new coordinate system is that the Hamiltonian can then be expressed as a function of action only, $H = H(I)$, while the frequency of the nonlinear oscillations Ω is given by the time derivative of the angle, *i.e.* $d\theta/dt = \Omega$. If we define a phase-space cylinder whose radius is I , azimuthal coordinate is θ , and axial coordinate is time, then the orbit of a particle with action I winds helically along the surface of this cylinder. The orbits of different particles with different actions will lie on surfaces of concentric cylinders. The time taken by the particle to execute one azimuthal rotation is $2\pi/\Omega$, so that the oscillation frequency of the particle is the azimuthal frequency of the motion. If we assume that time is periodic, with period T , then it is convenient to define a phase-space torus whose minor radius is I , poloidal angle is θ , and toroidal angle is $\phi = 2\pi t/T$. The particle's orbit then winds along the surface of this torus. If we consider the intersection of this torus with a plane at fixed ϕ , then the orbit of the particle will intersect this plane every time it completes a toroidal cycle around the torus. If for a given particle $\Omega T/(2\pi) = r/s$ where r and s are any integers, *i.e.* the ratio of the particle's poloidal frequency to the toroidal frequency is a rational number, then the change in θ per toroidal orbit is $2\pi r/s$. Thus, after s toroidal orbits the particle will return to the same value of θ . The particle will then intersect with the plane at fixed ϕ at only s number of points. Such tori are known as rational tori. The ratio of the two frequencies is known as the winding number. If the winding number is an irrational number, the intersection of the particle's orbit with the constant ϕ plane will eventually form a closed curve (a circle). Such tori are known as irrational tori. The set of discrete points formed on the constant ϕ surface whenever the particle's orbit intersects it forms the so-called Poincaré surface-of-section. The study of this two-dimensional

phase-space surface is equivalent to studying the motion of a particle in the full three-dimensional phase space [1]. Generalization of these ideas to higher dimensional periodic systems can be easily done [1].

II. CHIRIKOV-TAYLOR MAP OR THE STANDARD MAP

The one-dimensional motion of a charged particle in an infinite set of plane electrostatic waves, where all the waves have the same wave number and wave amplitude but whose frequencies are integer multiples of a fundamental frequency, is given by:

$$\frac{dx}{dt} = v \quad (6a)$$

$$\frac{dv}{dt} = \frac{eE}{m} \sum_{n=-\infty}^{\infty} \sin(kx - n\omega t) \quad (6b)$$

The corresponding Hamiltonian:

$$H(x, v, t) = \frac{v^2}{2} + \frac{eE}{mk} \sum_{n=-\infty}^{\infty} \cos(kx - n\omega t) \quad (7)$$

is periodic in time with period $T = 2\pi/\omega$. By using Fourier series analysis, it is easy to show that Eq. (6b) can be re-expressed as:

$$\frac{dv}{dt} = \frac{eE}{m} T \sin(kx) \sum_{n=-\infty}^{\infty} \delta(t - nT) \quad (8)$$

where δ is the Dirac delta function. Eq. (8) shows that in this interaction the particle receives a periodic kick in time, with period T , and with the strength of the kick being a function of its position. Using the new variables (θ, I, τ) where $\theta = kx$ ($0 \leq \theta < 2\pi$) is the angle, $I = kTv$ is the action, and $\tau = t/T$ is the normalized time, Eqs. (6a) and (8) become:

$$\frac{d\theta}{d\tau} = I \quad (9a)$$

$$\frac{dI}{d\tau} = K \sin(\theta) \sum_{n=-\infty}^{\infty} \delta(\tau - n) \quad (9b)$$

where $K = kT^2(eE/m)$ is the normalized amplitude. The periodic nature of the interaction leads to the following mapping equations [Appendix C]:

$$\theta_{n+1} = \theta_n + I_n + K \sin(\theta_n) \pmod{2\pi} \quad (10a)$$

$$I_{n+1} = I_n + K \sin(\theta_n) \quad (10b)$$

where (θ_n, I_n) are the angle and the action of the particle just before it receives its n -th kick (*i.e.* just before time nT). The mapping equations (10a) and (10b) are known as the Chirikov-Taylor map [5, 6] or, more commonly, the standard map. This map is a paradigm for twist maps and has been studied extensively in the literature [7]. The mapping equations produce a Poincaré surface-of-section [1, 2] of the motion of the particle so that the motion, which occurs in three phase-space dimensions (namely, θ , I , and τ , with τ assumed to be periodic with period 1), can be analyzed and viewed in two phase-space dimensions (θ, I) . The mapping equations give a set of discrete points formed by the intersection of the particle's orbit with a constant τ plane. Moreover, the mapping equations are much easier to set up and evolve accurately on a computer than the differential equations from which they are derived.

For unperturbed motion, *i.e.* $K = 0$, a particle's orbit lies on a torus of minor radius I (constant of the motion), poloidal angle θ , and toroidal angle $\phi = 2\pi\tau$. From Eq. (9a) the time taken by the particle to go one poloidal cycle is $2\pi/I$, so that the poloidal frequency of the particle's orbit is I . The toroidal frequency, in our normalized units, is 2π (which is the same as the normalized frequency of the kicks). Thus, the ratio of the poloidal to the toroidal frequency for a particle is $I/(2\pi)$. The unperturbed phase space for the particles are nested rational ($I/(2\pi) = r/s$, r and s any integers) and irrational tori.

III. SOME PROPERTIES OF THE STANDARD MAP

If in Eqs. (10a, 10b) we replace I by $I + 2\pi$, the mapping equations remain invariant. So the standard map is periodic in I with period 2π . Thus, when looking at a surface-of-section we need to display I between $-\pi$ and π only. The rest of phase space will look exactly the same.

Consider a particle whose initial angle $\theta_0^{(1)}$ and action $I_0^{(1)}$ are such that $I_1^{(1)} = I_0^{(1)}$ and $\theta_1^{(1)} = \theta_0^{(1)} \pmod{2\pi}$ (*i.e.* after a kick there is no change in the particle's action and angle). Here the subscript denotes the mapping iteration index and the superscript denotes the number of iterates required to come back to the initial values of action and angle (modulo 2π). Then, from Eqs. (10a, 10b), we note that $\theta_0^{(1)} = 0$ or π , and $I_0^{(1)} = 2m\pi$, for m any integer. The points represented by these action-angle values are known as fixed points (since they do not change their values after any number of kicks). Thus, the standard map has two sets of fixed points: $(\theta^{(1)}, I^{(1)}) = (0, 2m\pi)$ and $(\theta^{(1)}, I^{(1)}) = (\pi, 2m\pi)$. In analogy with the fixed points of the nonlinear oscillator, the stability of these fixed points can be easily determined (see *e.g.* [2]). We find that the first set of fixed points corresponds to hyperbolic fixed points and the

motion in the vicinity of these fixed points is unstable. The second set of fixed points corresponds to elliptic fixed points provided $K < 4$ and the motion in the vicinity of these fixed points is stable. However, for $K > 4$ the second set of fixed points also become hyperbolic. The fixed points having the properties discussed here are known as "first order" fixed points. An s -th order fixed point, $(\theta^{(s)}, I^{(s)})$, satisfies the relations: $\theta_n^{(s)} = \theta_0^{(s)} \pmod{2\pi}$, $I_n^{(s)} = I_0^{(s)}$ for $n = s$ and not for any other integer $0 < n < s$. An s -th order fixed point corresponds to a particle whose orbit lies on a rational torus with $I/(2\pi) = r/s$ for r any integer.

There is another set of points associated with the standard map that are of interest. Consider the case when the amplitude of the wave is an integer multiple of 2π , i.e. $K = 2\pi k$ (k being a positive integer) and a particle's initial angle is $\pi/2$ and its initial action is $2\pi l$ (l being any integer). Then after each subsequent kick the particle's action will increase by $2\pi k$. If the initial angle was $3\pi/2$ the particle's action will decrease by $2\pi k$ after each kick. These are known as "accelerator modes."

IV. NUMERICAL RESULTS OF THE STANDARD MAP

In plotting the numerical results for the standard map we need to show only the range $-\pi \leq I < \pi$. The angle θ , which describes the poloidal motion of a particle on the phase-space torus, will be plotted as a linear coordinate with period 2π . So, clearly, all values of I at $\theta = 2\pi$ are identical to those at $\theta = 0$. Thus, the unperturbed (i.e. $K = 0$) motion of a particle will form a set of discrete points at a fixed I ranging in θ from 0 to 2π . Different particles will correspond to different sets of initial conditions.

Fig. 2 displays the surface-of-section when $K = 0.1$ for a number of different initial conditions. It is easy to identify the orbit of a given particle as most of the orbits form almost closed curves. Whereas all the particles' orbits were along straight lines of constant I for $K = 0$, we see that, for $K = 0.1$, there is a dramatic modification to the orbits which are around $I = 0$. However, outside this region the orbits are small deviations away from straight lines of constant I . The behavior near $I = 0$ can be easily understood. From Eqs. (6a, 6b), we see that, for small amplitudes, $\alpha = eEk/(m\omega^2) \ll 1$, the motion of a particle resonant with a given wave (labelled n), i.e. a particle whose velocity is near $n\omega/k$ ($n = 0, \pm 1, \pm 2, \dots$), is most affected by that wave. In other words, a particle which is nearly at rest in the frame of one of the plane waves will be most affected by that wave. The effect of other waves will essentially phase mix to give a very small perturbation. However, as seen in the first section, particles whose velocities are near the phase velocity of a plane wave are trapped and the motion corresponds to a nonlinear

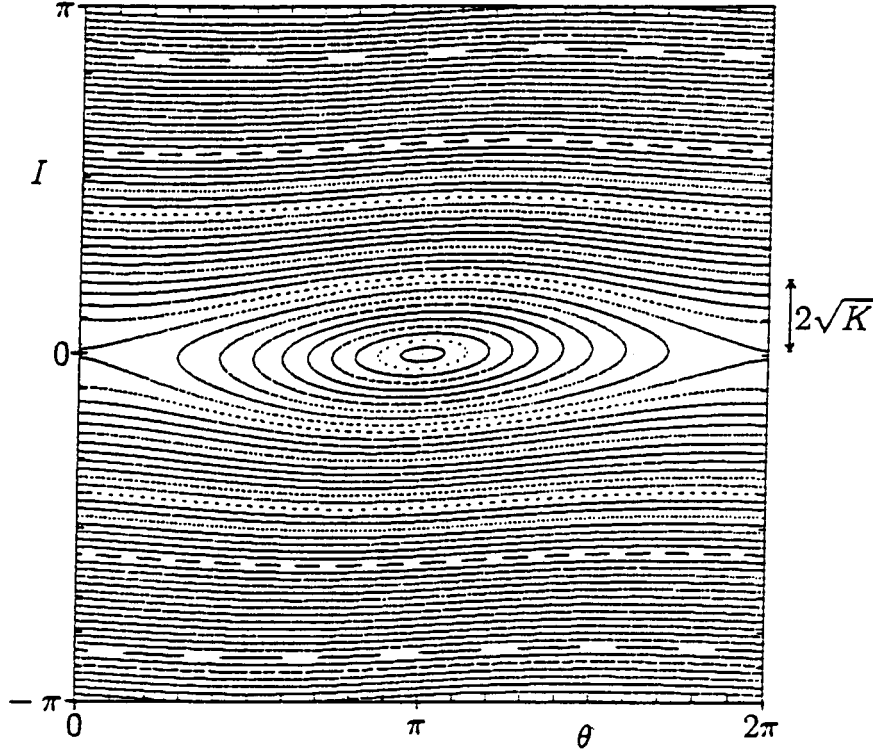


Figure 2. Surface-of-section for $K = 0.1$ showing a first order phase-space island of trapping width $2\sqrt{K}$ centered at $I = 0$.

oscillator. Indeed, Fig. 2 shows exactly the nonlinear oscillator behavior, as in Fig. 1, in the region around $I = 0$. The trapping width for any of the plane waves is $(\Delta v)_{tr}^n = 2\sqrt{\alpha}(\omega/k)$, or in terms of the normalized action-angle variables: $(\Delta I)_{tr}^n = 2\sqrt{K}$. A quick check of Fig. 2 shows that the trapping width is exactly what would be expected from this simple argument. Moreover, the location of the first order hyperbolic and elliptic fixed points at $I = 0, \theta = 0$ and $I = 0, \theta = \pi$, respectively, are exactly as indicated in the previous section.

The consequences of two very important theorems are on display in Fig. 2. The first theorem, referred to as the Poincaré-Birkhoff theorem [8], states that on a rational torus corresponding to the unperturbed motion, with winding number r/s , there will remain $2ls$ ($l = 1, 2, \dots$) number of fixed points after a small perturbation. Since for the unperturbed motion $I/(2\pi) = 0$ is a rational surface with $s = 1$, the number of fixed points observed in Fig. 2 at $I = 0$ are in agreement with the Poincaré-Birkhoff theorem. The similar breakup of other rational tori are not visible in Fig. 2 as their trapping widths are very small. The second theorem, referred to as the KAM theorem (named after Kolmogorov, Arnold, and Moser [9–11]) states that unperturbed irrational tori which are sufficiently

far away from the nearest unperturbed rational tori are stable to small perturbations (details of the theorem and the conditions for its validity can be found in [2]). Fig. 2 shows many such tori which have been slightly modified from their unperturbed forms. Such tori are referred to as KAM tori or KAM surfaces.

Figure 3 shows the results of the standard map for $K = 0.5$. Even though the amplitude of the perturbation is large, the breakup of the rational tori with $s = 2$ at $I = \pm 2\pi/2 = \pm\pi$ and with $s = 3$ at $I = \pm 2\pi/3$, in agreement with the Poincaré-Birkhoff theorem, can be clearly identified. Furthermore, even though the amplitude is greater than that required for the rigorous validity of the KAM theorem, there continue to be KAM surfaces which persist at this large amplitude. In this figure additional features are clearly discernable near $I = 0$ and $\theta = 0$. A magnification of the region marked by the box is shown in Fig. 4. Here we notice the richness and the complicated behavior of the motion in the vicinity of the hyperbolic fixed point. There exist a series of high-order fixed points, both elliptic and hyperbolic, with the nonlinear oscillator type of motion occurring in the vicinity of elliptic points. Thus, as is apparent, the phase-space picture is self-similar with the phase-space structure of Fig. 3 being repeated on a finer scale. The nearly uniformly dense region surrounding the hyperbolic fixed point at $I = 0$ and $\theta = 0$ and extending along the separatrix of the first order fixed point (seen in Fig. 3) is due to a single particle. The usual phase-space tori are completely destroyed in this region and the motion in the vicinity of the hyperbolic fixed point is very complex. This motion is referred to as "stochastic" or "chaotic" motion and we shall discuss detailed properties of this type of motion later. Figs. 3 and 4 show regions of local stochasticity where no periodic motion is discernable and the motion of the particle is no longer restricted to the surface of a torus.

In section I, it was shown that there emanate stable and unstable manifolds from a hyperbolic fixed point. While these manifolds overlapped for the nonlinear oscillator, small perturbations tend to separate out these manifolds. A manifold cannot intersect itself, otherwise the solutions to the equations of motion would not be unique for a given set of initial conditions. However, the stable and unstable manifolds can intersect each other. This intersection point in phase space is known as a "homoclinic" point. (The intersection point of a stable manifold from one hyperbolic fixed point with an unstable manifold from a different hyperbolic fixed point is known as a "heteroclinic" point.) A homoclinic point is not a fixed point of the motion, and if there exists at least one homoclinic point, then there must be an infinite number of them. The density of homoclinic points increases as one approaches the hyperbolic fixed point. This, along with the requirement that Hamiltonian systems

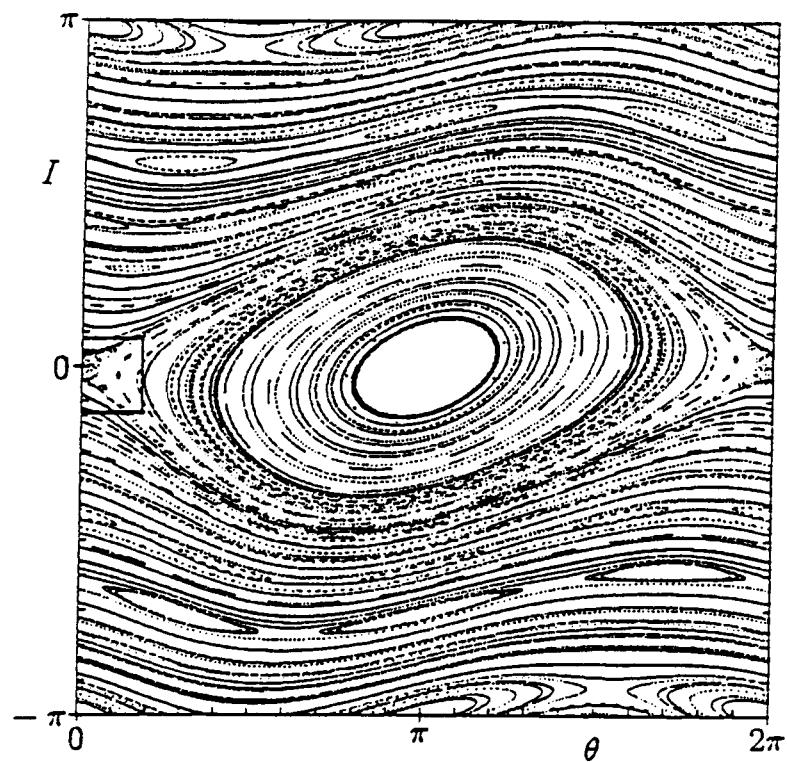


Figure 3. Surface-of-section for $K = 0.5$ showing the existence of higher order islands.

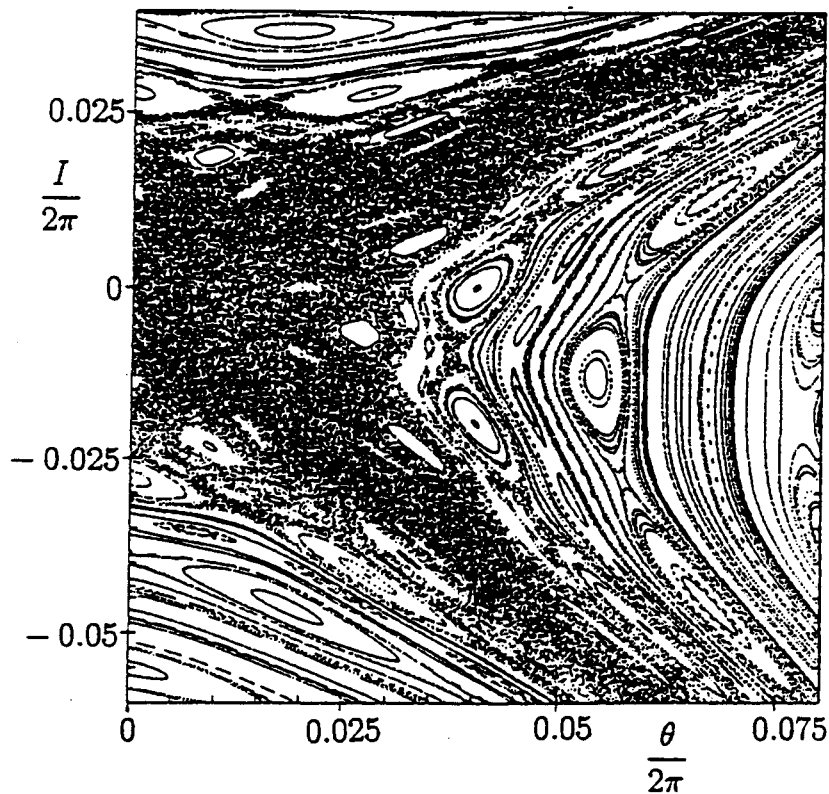


Figure 4. A magnified view of the rectangular region marked in Fig. 3 near the hyperbolic fixed point at $\theta = 0$, $I = 0$.

satisfy Liouville's theorem, leads to the extremely complicated behavior in the vicinity of hyperbolic fixed points and along the separatrix. Details of this complexity are beyond the scope of this article. Interested readers are referred to [1, 2] and references therein. Fig. 4 gives evidence of the complicated interaction not only between stable and unstable manifolds of the hyperbolic fixed point at $(I = 0, \theta = 0)$ but also between different hyperbolic fixed points generated through the breakup of rational tori.

Upon comparing Fig. 2 with Fig. 3 we notice that, as the amplitude of the perturbation is increased, more KAM tori are destroyed with the concurrent appearance of more fixed points. KAM surfaces form barriers in phase space which do not allow, for example, intersection of stable and unstable manifolds from hyperbolic points on different sides of the KAM surface. Thus, particle orbits, which can wander in phase along these manifolds (as seen in Fig. 4), are prohibited from crossing those parts of phase space where KAM tori exist. In other words, the existence of KAM tori stops the phase-space motion of certain particles from becoming globally stochastic where these particles have access to the entire range of action. One is inevitably led to ask the question: at what amplitude is the last KAM surface destroyed? A simple way to answer this question is as follows. Each rational torus $I = 2\pi n$ ($n = 0, \pm 1, \pm 2, \dots$) corresponds to a particle velocity being equal to the phase velocity of the n -th plane wave in Eq. (6b), i.e. the particle is in resonance with the n -th plane wave. These tori are also called resonant tori. The trapping width, as discussed above, associated with the resonant tori is approximately given by $(\Delta I)_{tr}^n = 2\sqrt{K}$ where each resonant torus is treated independently of other resonant tori (i.e. each plane wave is treated independently of other plane waves). Consider two such neighboring tori l and $l+1$. If the sum of the trapping width of each of these tori is equal to the separation between the tori, i.e. the trapping widths of neighboring resonant tori overlap, then it is intuitively clear that there cannot exist any KAM surface between these tori. This criterion can be expressed as: $(\Delta I)_{tr}^l + (\Delta I)_{tr}^{l+1} \gtrsim (\Delta I)_{l,l+1}$ where $(\Delta I)_{l,l+1}$ is the separation in action between two neighboring resonant tori. This is known as the simple Chirikov resonance overlap criterion. For the standard map this condition gives $K \gtrsim \pi^2/4$. This condition is modified significantly due to the presence of secondary resonances (corresponding to rational tori besides those at $I = 2\pi n$) as seen in Fig. 2. Detailed numerical calculations show that the last KAM surface is destroyed for $K \approx 0.9716$ [12]. Thus, the simple resonance overlap criterion is too pessimistic. Once the last KAM surface is destroyed we have a transition from local to global stochasticity. The portrait of the standard map at $K = 1$ in Fig. 5 shows a very rich phase-space structure. Notice that remnants of the resonant tori at $I = 0, \pm 2\pi/3, \pm \pi$ still remain. Thus, the motion of many particles

remains coherent for values of K just exceeding the one that destroys the last KAM surface. The majority of initial conditions do not lead to chaotic dynamics until K is closer to, or greater than, the values of the Chirikov condition.

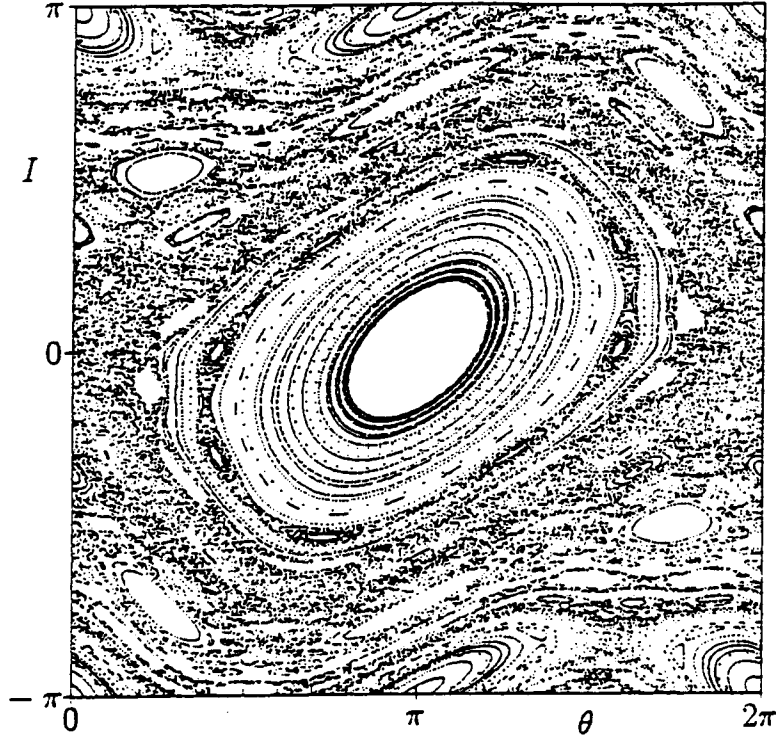


Figure 5. Surface-of-section for $K = 1$. This K is slightly greater than the critical $K_c \approx 0.9716$, for which the last KAM surface is destroyed.

V. PROPERTIES OF CHAOTIC MOTION

There are distinct differences between coherent and chaotic motion besides those that appear in the surface-of-section plots discussed above. For motion occurring in three phase-space dimensions (θ , I , and τ , being the phase-space variables for the standard map), a Poincaré surface-of-section is two-dimensional so that the entire dynamics can be visualized easily. However, in cases when the phase-space dimensions are greater than three, a Poincaré surface-of-section does not allow for simple visualization so that regions of chaotic and coherent motion may not be easily discernable. In this section, using the standard map as an example, we will discuss some of the distinguishing features between co-

herent and chaotic motion that are applicable to dynamical systems with phase-space dimensions greater than three.

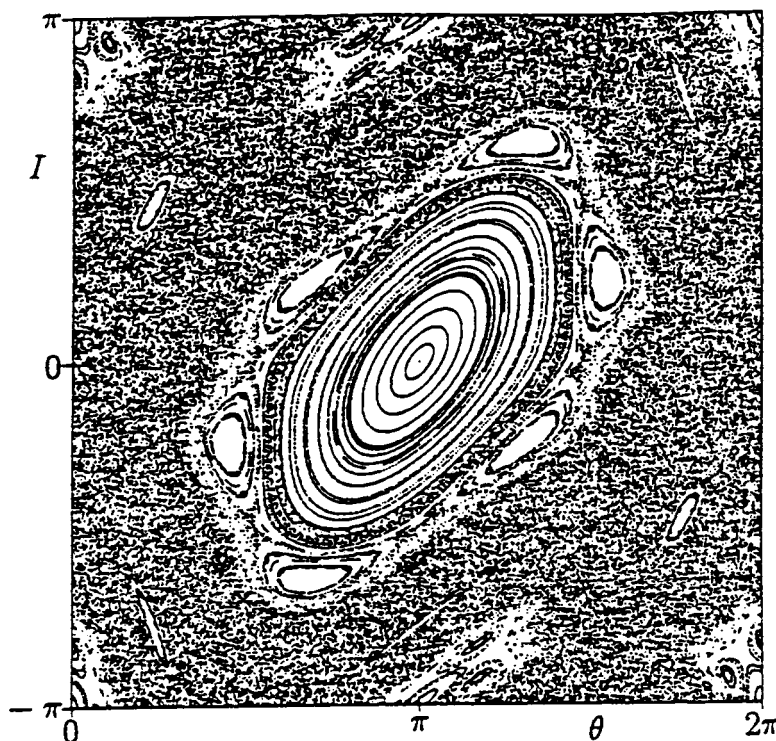


Figure 6. Surface-of-section for $K = 1.5$.

A. Evolution of Particle Orbits

Figure 6 shows regions of coherent and chaotic motion in the surface-of-section plot for the standard map when $K = 1.5$. The coherent part of the phase space is dominated by the island surrounding the first order elliptic fixed point discussed earlier. Consider a set of initial conditions, given by the circle in Fig. 7a, located inside this island for $K = 1.5$. After 100 iterates of the standard map this circle is mapped into the curve shown in the same figure. A magnified view of the tip, given in Fig. 7b, clearly shows that the curve obtained after 100 iterates is a closed curve. The area enclosed by this curve is the same as the area of the circle. This is a consequence of Liouville's theorem. Next consider a set of initial conditions, given by the circle in Fig. 8a and having the same area as the circle in Fig. 7a, located in the chaotic part of the phase space of Fig. 6. The mapping of this curve after four iterates of the map and after seven iterates of the map is shown in the same figure.

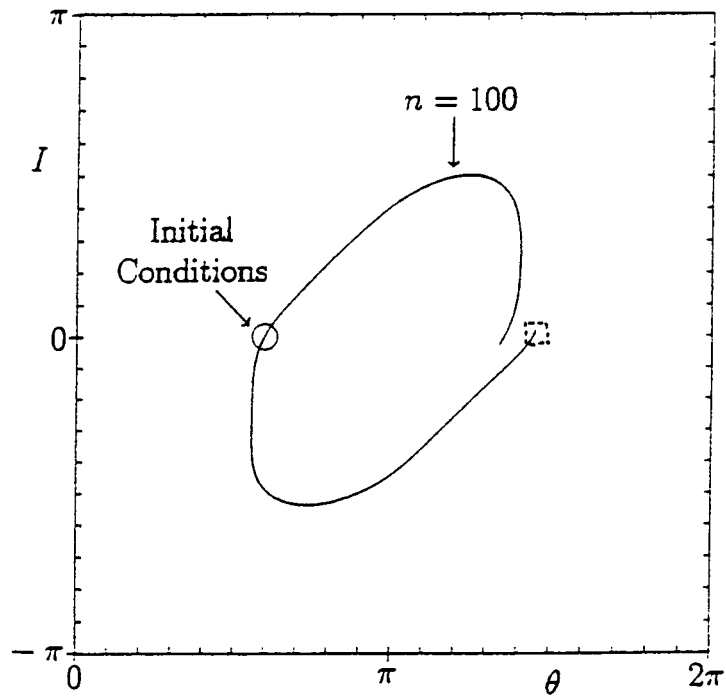


Figure 7a. Phase-space portrait of a set of particles, in the coherent part of phase space, at $n = 0$ and at $n = 100$ for $K = 1.5$.

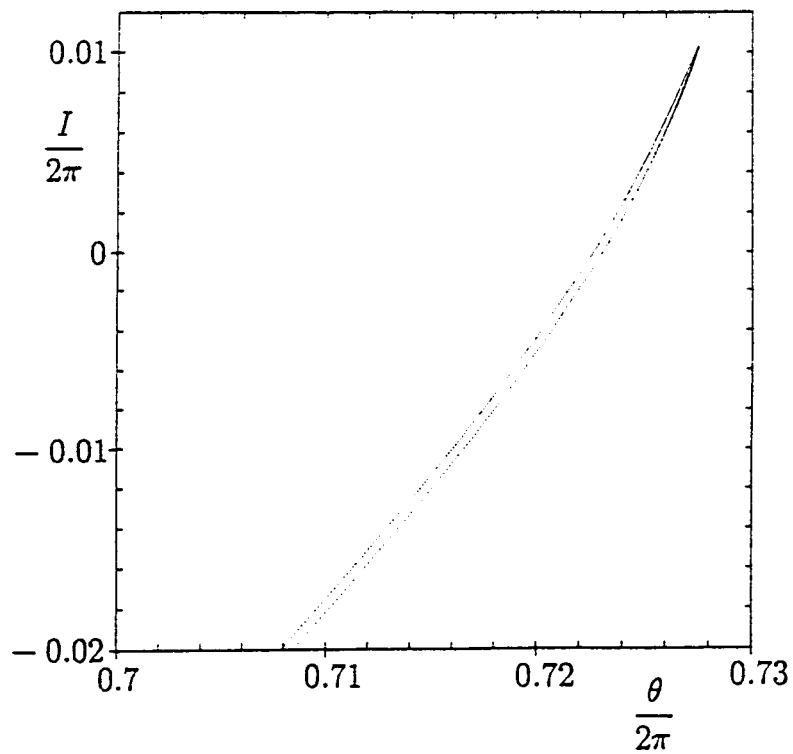


Figure 7b. A magnified view of the box shown in Fig. 7a.

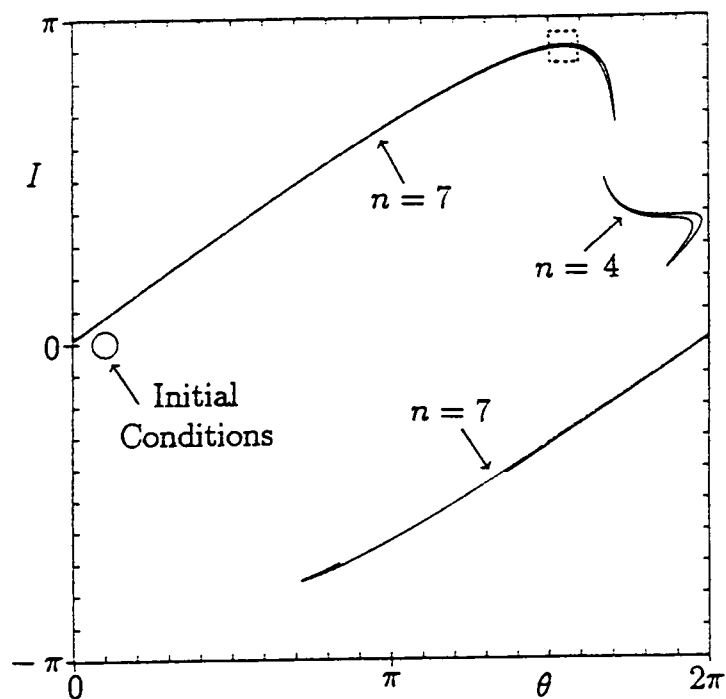


Figure 8a. Phase-space portrait of a set of particles, in the chaotic part of phase space, at $n = 0$, $n = 4$, and $n = 7$.

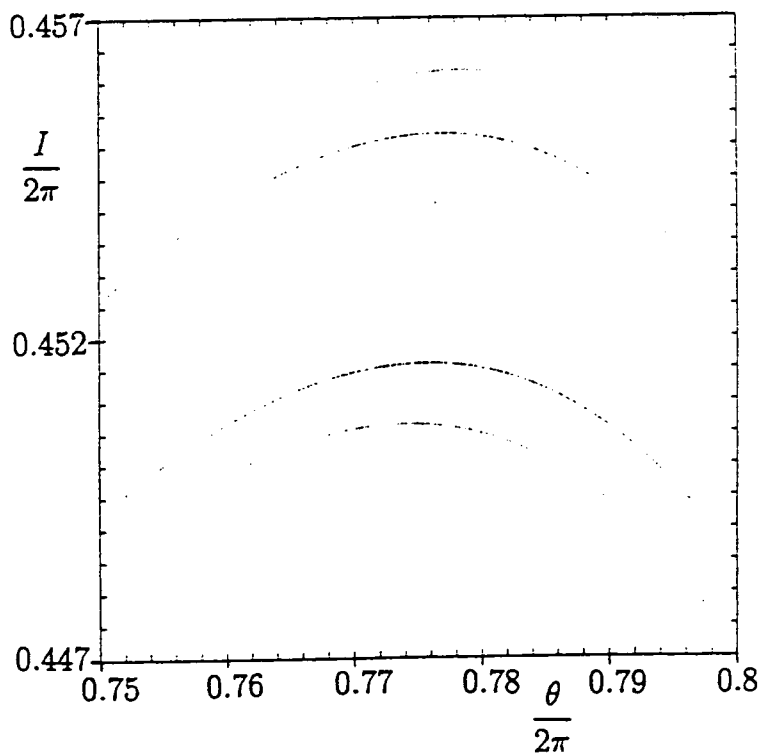


Figure 8b. A magnified view of the box shown in Fig. 8a.

Clearly, the initial circle is mapping into a complicated curve after seven iterates. This curve is thinner and longer than the circle and, as expected, encloses an area which is the same as the area of the circle. The complicated feature of this curve is exemplified in Fig. 8b where a magnified view of a part of the curve shows multiple sheets associated with the curve. These sheets are generated by a stretching and folding over of the original circle of initial conditions. After 100 iterates of the map, the initial circle of initial conditions maps into the picture shown in Fig. 8c. Clearly, considerable stretching and folding has taken place in order to produce the observed surface-of-section. The initial conditions are now spread out over the chaotic region of Fig. 6. The large scale regions which are empty correspond to coherent motion. A comparison of Fig. 8c with Fig. 7a shows a dramatic difference in the evolution of particle trajectories between the coherent and the chaotic regions.

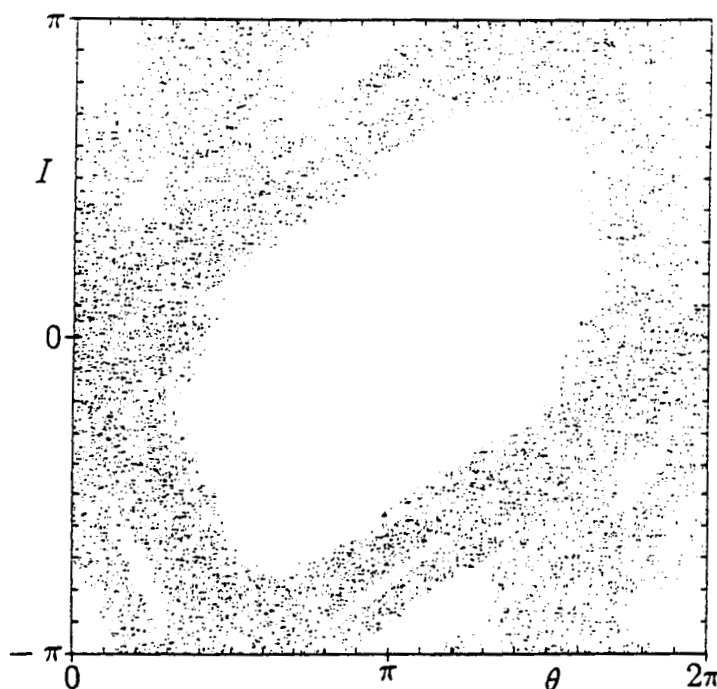


Figure 8c. Phase-space portrait at $n = 100$ for the set of particles shown in Fig. 8a.

B. Separation of Orbits of Initially Nearby Particles

Consider two particles which are initially separated in action by 1.0×10^{-8} and have the same θ . If both of these particles are located in the

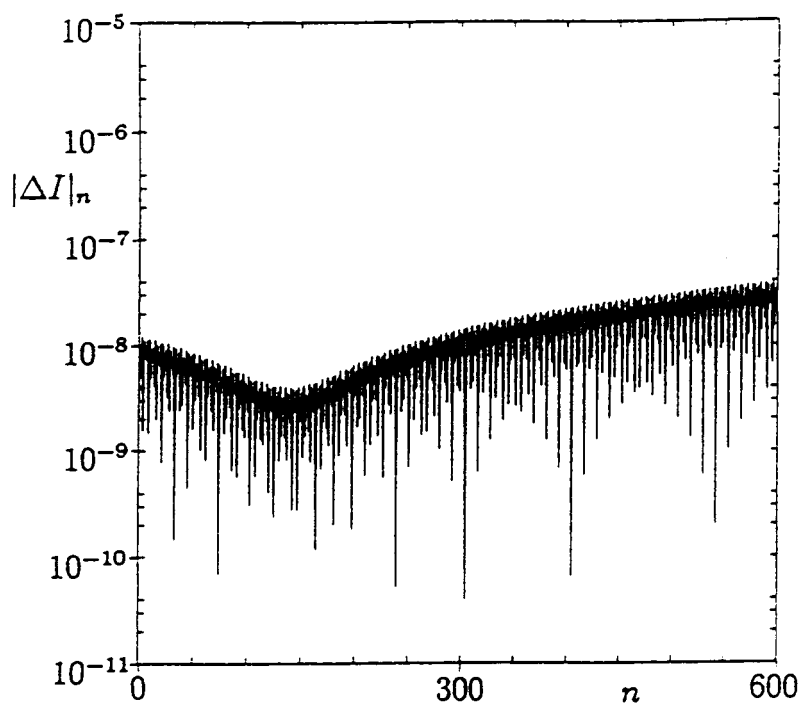


Figure 9. The magnitude of the difference in action of two particles versus n ($K = 1.5$), located in the coherent part of phase space.

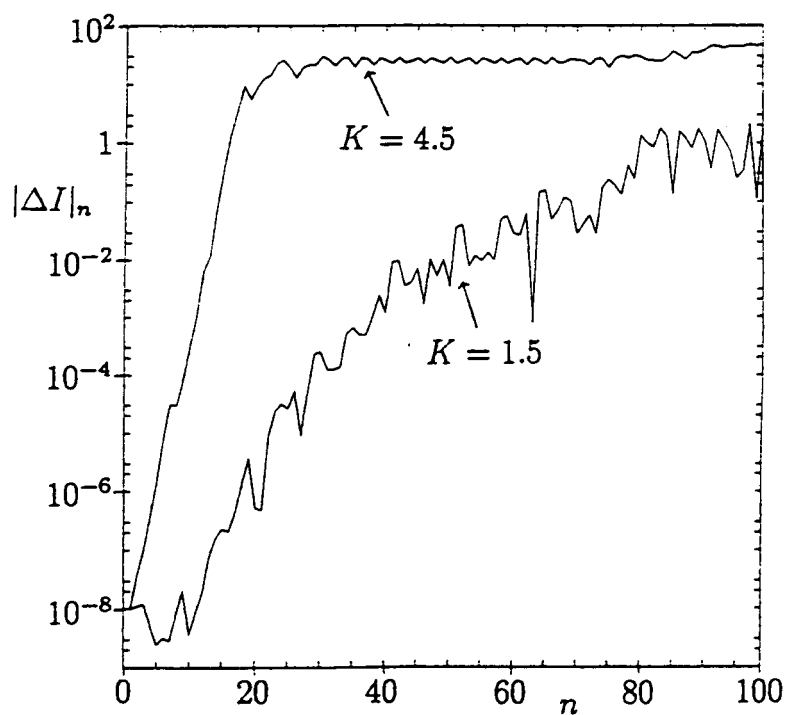


Figure 10. Same as Fig. 9, except that the particles are initially located in the chaotic part of phase space.

coherent part of phase space (*i.e.* lying initially within the circle of Fig. 7a), the separation in action between these particles as function of the number of iterates of the map is as shown in Fig. 9 for $K = 1.5$. The actions of the two particles remain close to each other over an extended period of time. However, if the two particles are located in the chaotic part of phase space (*i.e.* lying initially within the circle of Fig. 8a), then the difference in the actions of the particles increases exponentially with time for early times. This is shown in Fig. 10 for two values of K . The separation is faster for larger amplitudes of the waves and the separation in action saturates at earlier times as the amplitude is increased. The exponential increase in the separation of initially nearby orbits in phase space indicates dynamics with sensitive dependence on initial conditions; this is the essential feature which leads to loss of information in chaotic systems. Small errors in measurements at some initial time will grow exponentially with time leading to unpredictability.

C. Frequency Spectrum of Particle Orbits

An orbit of a particle in phase space can be decomposed into a frequency spectrum leading to additional information about the dynamics. In particular, periodic, quasiperiodic, and chaotic properties of the orbit can be determined from the spectrum analysis. In order to illustrate the connection between a particle's orbit and its frequency spectrum we Fourier analyze the action of a particle obtained from the standard map.

Fig. 11a is the surface-of-section for a single particle started in the coherent part of phase space for $K = 1.5$. The particle's orbit initially started off on one island returns to that island after every six iterates of the standard map. The sixth-order islands shown in Fig. 11a are easily discernable in Fig. 6 where they surround the primary island. The discrete set of actions generated by Eq. (10b), leading to Fig. 11a, are Fourier analyzed to give the frequency spectrum, $I(\nu)$ as a function of the frequency ν , shown in Fig. 11b. Since the mapping equations generate a value for the action after one (normalized) unit of time, the frequency spectrum is bound to lie in the interval $[-0.5, 0.5]$. However, the spectrum is symmetric around $\nu = 0$ so we only show the spectrum in the interval $[0, 0.5]$. There are two primary frequencies which determine the frequency spectrum of orbit. The first frequency corresponds to the particle jumping from island to island in the surface-of-section and the other frequency corresponds to the motion of the particle in any given island. The former frequency is obviously $1/6$ and dominates the spectrum in Fig. 11b. The latter frequency has its main peak near $\nu = 0.2$. The rest of the spectrum is essentially composed of harmonics and sums and differences of these frequencies. The motion of the particle is clearly periodic.

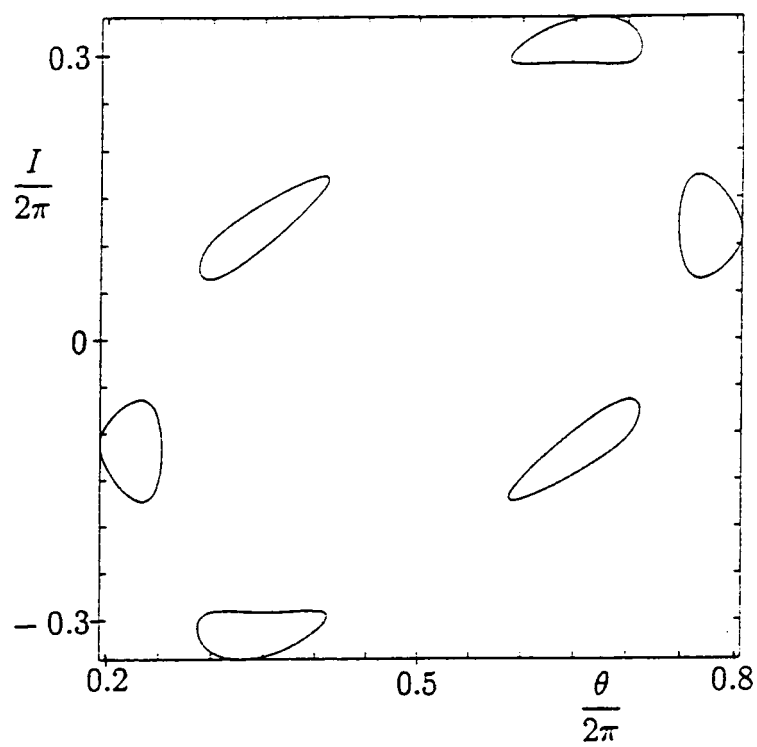


Figure 11a. Surface-of-section for a single particle ($K = 1.5$).

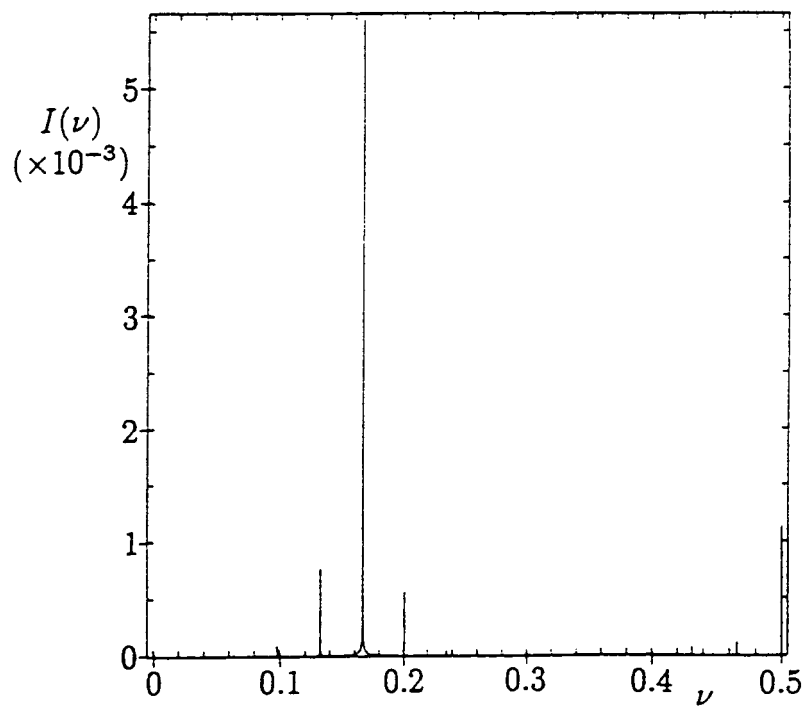


Figure 11b. Frequency spectrum of the orbit in Fig. 11a.

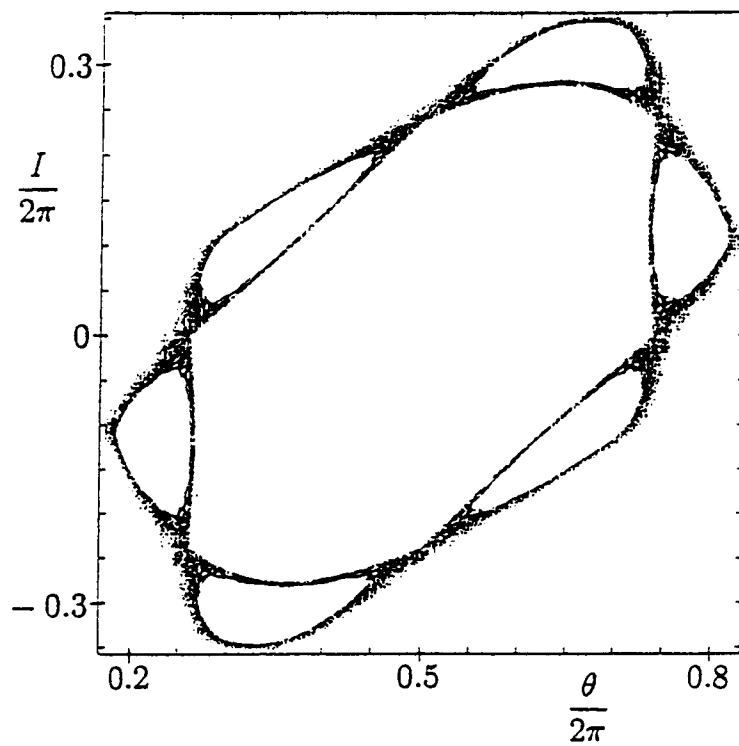


Figure 12a. Surface-of-section for a single particle ($K = 1.5$).

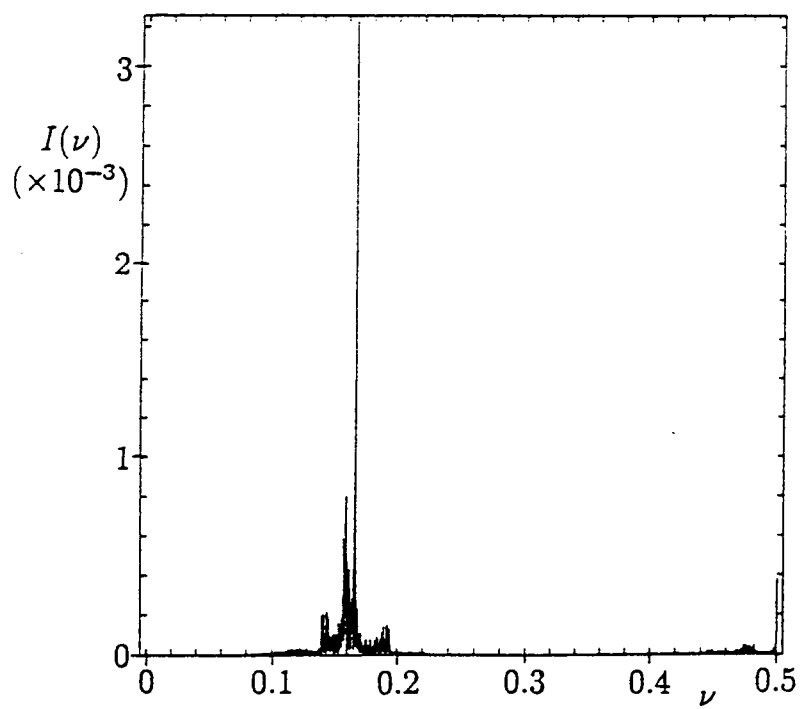


Figure 12b. Frequency spectrum of the orbit in Fig. 12a.

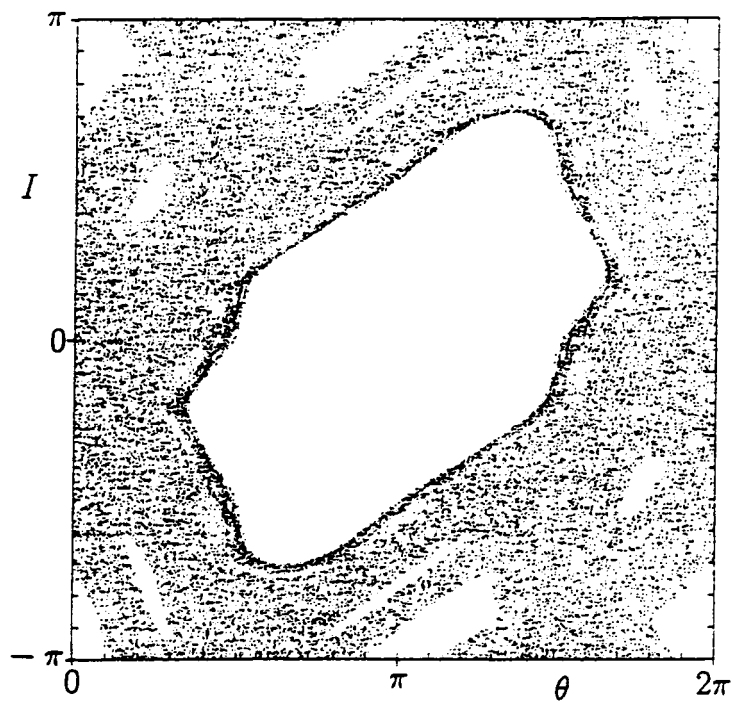


Figure 13a. Surface-of-section for a single particle ($K = 1.5$).

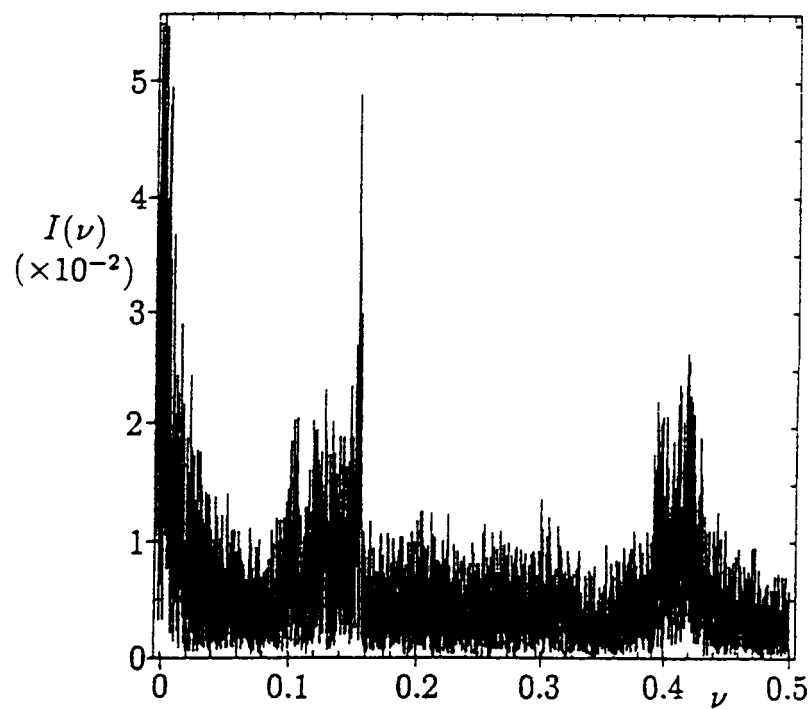


Figure 13b. Frequency spectrum of the orbit in Fig. 13a.

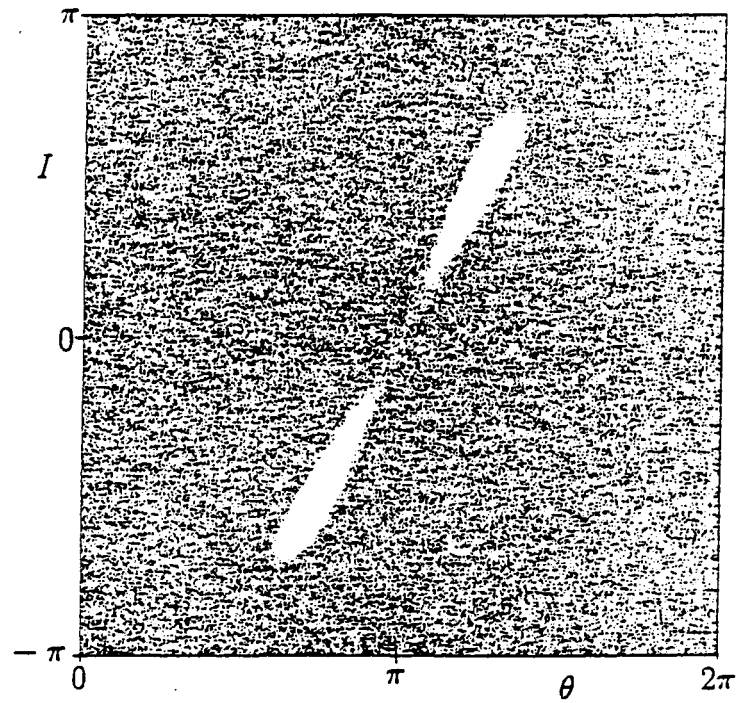


Figure 14a. Surface-of-section for a single particle ($K = 4.5$).

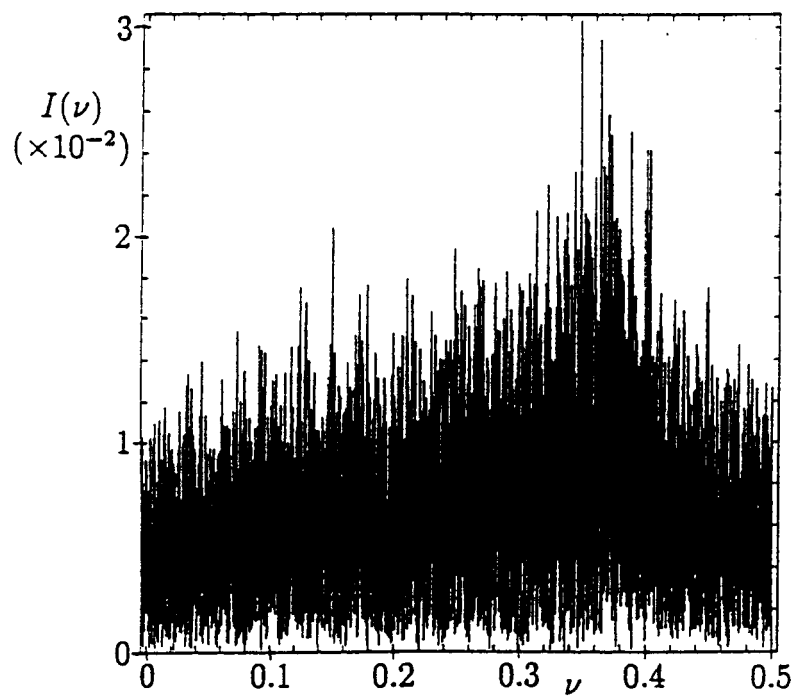


Figure 14b. Frequency spectrum of the orbit in Fig. 14a.

Fig. 12a shows the orbit of a particle started near the separatrix of the sixth-order islands of Fig. 6 for $K = 1.5$. The corresponding frequency spectrum, apart from the dominating peak at $\nu = 1/6$ corresponding to the sixth-order island, is a broadband spectrum and shown in Fig. 12b. The spectrum corresponding to the motion of the particle around any given island is broadband, composed of many peaks, and centered around $\nu = 0$. The jumping of the particle from island to island in the surface-of-section shifts the spectrum to lie near $\nu = 1/6$, maintaining the features of being broadband and composed of many peaks.

Fig. 13a shows the surface-of-section for the orbit of a single particle, for $K = 1.5$, which is initially located in the chaotic part of phase space. It is worth noting that this picture is essentially the same as generated in Fig. 8c. One aspect which is intuitively clear from Fig. 13a but difficult to prove is that the motion of a single particle in chaotic phase space will eventually come arbitrarily close to any given point in the connected chaotic phase space. This property forms a basis for the *ergodic hypothesis* [2]. The frequency spectrum for this particle, Fig. 13b, is broadband covering the entire frequency range. The peak at $\nu = 1/6$ is a consequence of the fact that the particle, during its travels in the chaotic phase space, spends a lot of time near the sixth-order chain of islands discussed above. This is obvious in Fig. 13a where the darker part of phase space is near the sixth-order islands.

Figs. 14a and 14b show the surface-of-section for a single particle in chaotic phase space and the corresponding frequency spectrum, respectively, for $K = 4.5$. The spectrum is more uniformly broadband than in Fig. 13b. Fig. 14a shows that the fixed point at $I = 0$, $\theta = \pi$ which was elliptic for $K = 1.5$ (Fig. 6) has now become hyperbolic. This transition in the character of a fixed point has been discussed earlier. A comparison of Figs. 13a and 14a, and of Figs. 13b and 14b, shows that as the amplitude K is increased a larger part of phase space becomes chaotic and the frequency spectrum becomes more uniformly broadband, *i.e.* more "noiselike."

In summary, we have shown in this section that, initially, nearby particles in phase space will diverge exponentially if these particles are located in the chaotic phase space. Also, the frequency spectrum of an orbit of a particle located in chaotic phase space will be broadband. The trajectory of a single particle will wander through the entire connected region of chaos.

VI. EFFECT OF AN ELECTROSTATIC WAVE ON A CHARGED PARTICLE IN A MAGNETIC FIELD

In space plasmas and laboratory plasmas, static magnetic fields play

an important role in determining the dynamics of charged particles. Electrostatic waves, which either exist in the plasma or are externally imposed, can interact with the charged particles and significantly modify their trajectories. An example of such electrostatic waves is lower hybrid waves whose frequencies typically lie in the range of the ion-plasma frequency or below. In auroral plasmas, lower hybrid waves are generated by energetic electrons which are injected into the supraaural region from the plasma sheet. It has been shown that these lower hybrid waves, propagating across the magnetic field, interact with ions (H^+ and O^+) of ionospheric origin and accelerate them upwards along the magnetic field lines [13]. In laboratory plasmas, lower hybrid waves are excited by means of waveguide grills at the edge of the plasma. The interaction of lower hybrid waves with ions has been of considerable interest and has been extensively studied [14–18]. Below we describe some of the interesting features of the motion of an ion in the presence of lower-hybrid type of waves.

Consider the motion of an ion in a constant magnetic field, being acted upon by an electrostatic wave propagating across the magnetic field. The Hamiltonian for the motion of the ion is:

$$H(x, v; t) = \frac{v^2}{2} + \frac{\Omega^2 x^2}{2} + \frac{QE_0}{Mk} \cos(kx - \omega_0 t) \quad (11)$$

where the magnetic field is assumed to be along the \hat{z} -direction, the electrostatic wave is propagating along the \hat{x} -direction, x and v are the position and velocity (along \hat{x}), respectively, of an ion of mass M and charge Q , E_0 is the electrostatic field amplitude with ω and k being the frequency and wave vector (along \hat{x}), respectively, and $\Omega = QB_0/M$ is the ion cyclotron frequency in a magnetic field of strength B_0 . Upon normalizing $\omega t \rightarrow \tau$, $kx \rightarrow q$, $kv/\omega \rightarrow p$, $\Omega/\omega \rightarrow \omega_0$, the above Hamiltonian can be transformed to:

$$H(q, p; \tau) = \frac{p^2}{2} + \frac{\omega_0^2 q^2}{2} + \epsilon \cos(q - \tau) \quad (12)$$

where $\epsilon = QE_0 k/(M\omega^2)$. The unperturbed Hamiltonian describes the motion of a simple pendulum. A canonical transformation to the action-angle ($I - \theta$) variables of the simple pendulum:

$$I = \frac{\omega_0}{2} \left(q^2 + \frac{p^2}{\omega_0^2} \right) ; \quad \theta = \tan^{-1} \left(\frac{\omega_0 q}{p} \right) \quad (13)$$

yields the Hamiltonian:

$$\begin{aligned}
 H(\theta, I; \tau) &= \omega_0 I + \epsilon \cos \left(\sqrt{\frac{2I}{\omega_0}} \sin \theta - \tau \right) \\
 &= \omega_0 I + \epsilon \sum_{n=-\infty}^{\infty} J_n \left(\sqrt{\frac{2I}{\omega_0}} \right) \cos(n\theta - \tau) \quad (14)
 \end{aligned}$$

where J_n is the Bessel's function of the n -th order. The unperturbed Hamiltonian, as expected, is just a function of the action, and the action as defined in Eq. (13) is a positive quantity. The Hamiltonian is periodic in τ with period 2π . A surface-of-section plot is obtained by numerically integrating the equations of motion corresponding to the above Hamiltonian and plotting the action-angle coordinates of the orbit after every 2π interval in τ . There are two distinct cases which are of interest and will be discussed below: the on-resonance case when $1/\omega_0 = \text{integer}$ (i.e. the wave frequency is a harmonic of the cyclotron frequency), and the off-resonance case when $1/\omega_0$ is close to an integer.

For the case of $1/\omega_0 = 5$, corresponding to an on-resonance case, and $\epsilon = 10^{-2}$, a plot of the surface-of-section is shown in Fig. 15a. The hyperbolic and the elliptic fixed points can be easily identified in the figure and it is interesting to note that neighboring islands, vertically or horizontally, have a common separatrix. Furthermore, all the separatrices are connected in such a way that a particle started on any given separatrix can, in principle, move to arbitrary values of the action along the separatrices. This phase-space picture does not change in its essential characteristics for any amplitude $\epsilon < 10^{-2}$, however infinitesimally small the amplitude becomes, provided $\epsilon > 0$. Thus, unlike the standard map where the trapping width corresponding to the primary island (island of order 1) increased in size as the square-root of the amplitude for small amplitudes of the perturbation, the trapping width corresponding to the primary islands remains essentially independent of amplitude for small amplitudes. There are no KAM surfaces separating the primary islands. The Chirikov resonance overlap criterion would not seem to apply since the neighboring islands overlap, sharing a common separatrix, for arbitrarily small amplitudes. The phase-space plot in Fig. 15a can be easily understood.

Consider a canonical transformation of the Hamiltonian in Eq. (14) to a new set of canonical variables (ψ, J) which are defined as: $\psi = m\theta - \tau$, $J = I/m$, where m is an integer. The transformed Hamiltonian is:

$$\begin{aligned}\bar{H}(\psi, J; \tau) &= (m\omega_0 - 1)J + \epsilon J_m \left(\sqrt{\frac{2mJ}{\omega_0}} \right) \cos(\psi) \\ &+ \epsilon \sum_{\substack{n=-\infty \\ n \neq m}}^{\infty} J_n \left(\sqrt{\frac{2mJ}{\omega_0}} \right) \cos \left\{ \frac{n}{m} \psi + \left(\frac{n-m}{m} \right) \tau \right\}\end{aligned}\quad (15)$$

In the on-resonance case, there exists an integer m such that $m\omega_0 = 1$. Since the terms under the summation sign depend explicitly on time the average effect on the motion of the particle can be ignored for small amplitudes. The leading order Hamiltonian in this case is just $\bar{H}_0(\psi, J; \tau) = \epsilon J_m \cos(\psi)$, and the corresponding equations of motion are:

$$\frac{d\psi}{d\tau} = \epsilon \frac{m}{\sqrt{2J}} J'_m \left(m\sqrt{2J} \right) \cos(\psi) \quad (16a)$$

$$\frac{dJ}{d\tau} = \epsilon J_m \left(m\sqrt{2J} \right) \sin(\psi) \quad (16b)$$

where the prime denotes a derivative with respect to the argument. There are two sets of fixed points of Eqs. (16a) and (16b), given by (ψ_h, J_h) and (ψ_e, J_e) , which satisfy, respectively, the following equations:

$$\cos(\psi_h) = 0 \text{ and } J_m \left(m\sqrt{2J_h} \right) = 0 \quad (17a)$$

$$\sin(\psi_e) = 0 \text{ and } J'_m \left(m\sqrt{2J_e} \right) = 0 \quad (17b)$$

It is easy to show that the first set of conditions, Eq. (17a), corresponds to hyperbolic fixed points while the second set of conditions, Eq. (17b), corresponds to elliptic fixed points. Let us define $j_{m,s}$ and $j'_{m,s}$ ($s = 1, 2, \dots$) to be such that $J_m(j_{m,s}) = 0$ and $J'_m(j'_{m,s}) = 0$, respectively. Then, for a given s , hyperbolic fixed points are located at $J_{h,s} = j_{m,s}^2/(2m^2)$ and $\psi_{h,s} = (2l+1)\pi/2$ ($l = 0, 1, 2, \dots$), and elliptic points are located at $J_{e,s} = j_{m,s}'^2/(2m^2)$ and $\psi_{e,s} = l\pi$ ($l = 0, 1, 2, \dots$). Since a surface-of-section for an orbit is obtained by determining the action-angle coordinates of a particle every 2π steps in τ , and since the angle coordinate θ is periodic with period 2π , then, from the transformation equations relating (ψ, J) to (θ, I) , the hyperbolic and elliptic points will be located at $I_{h,s} = j_{m,s}'^2/(2m)$, $\theta_{h,s} = (2l+1)\pi/(2m)$, and $I_{e,s} = j_{m,s}^2/(2m)$, $\theta_{e,s} = l\pi/m$, for $s = 1, 2, \dots$ and $l = 0, 1, \dots, 2m-1$. Thus, for any given s there will be $2m$ hyperbolic and $2m$ elliptic fixed points.

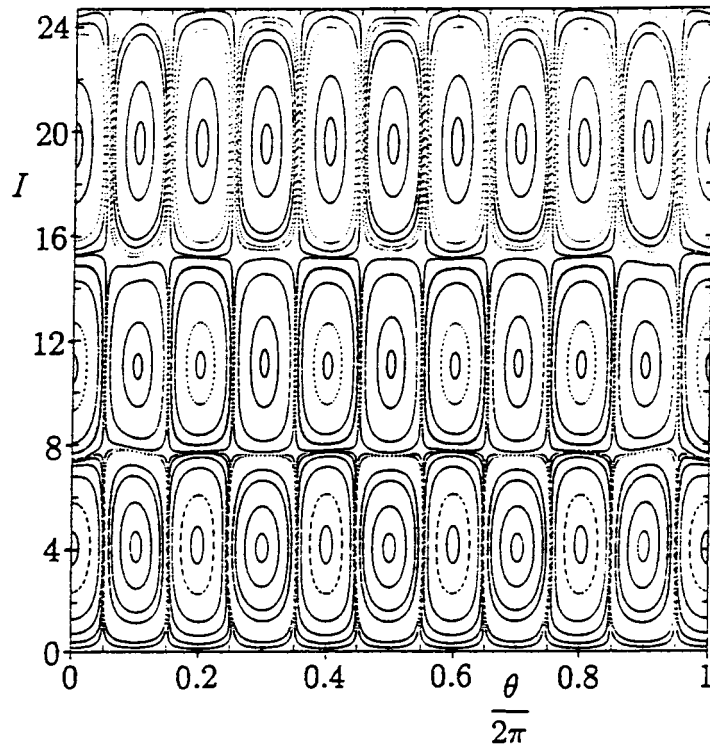


Figure 15a. Surface-of-section for $\omega_0 = 1/5$ and $\epsilon = 10^{-2}$.

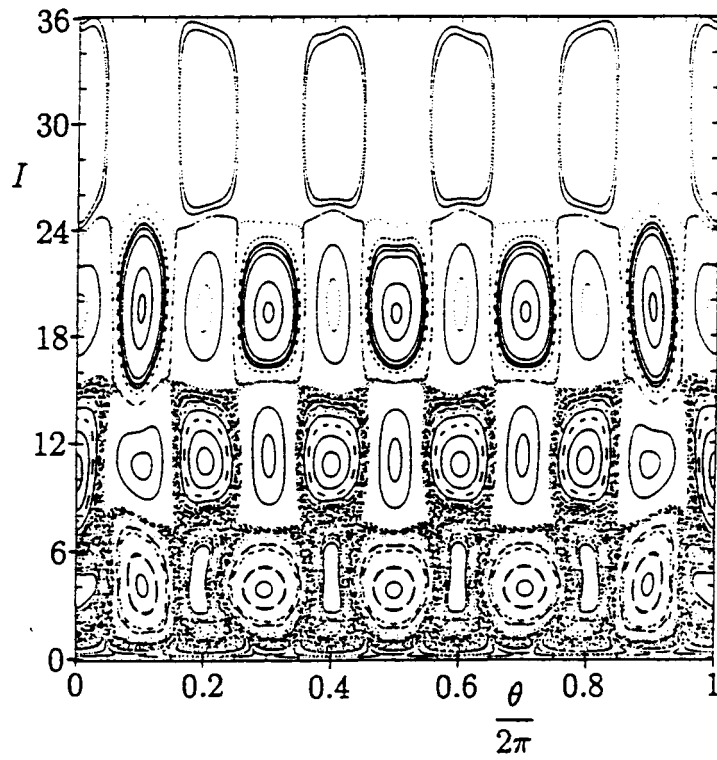


Figure 15b. Surface-of-section for $\omega_0 = 1/5$ and $\epsilon = 5 \times 10^{-2}$.

For $m = 5$ the first couple of zeros of the Bessel's function and its derivative are [19]: $j_{5,1} \approx 8.77$, $j_{5,2} \approx 12.34$, $j'_{5,1} \approx 6.42$ and $j'_{5,2} \approx 10.52$. Then the hyperbolic points are at $I_{h,1} \approx 7.69$ and $I_{h,2} \approx 15.22$. For each of these actions the hyperbolic points are at $\theta = \pi/10, 3\pi/10, 5\pi/10, \dots, 19\pi/10$. The elliptic points are at $I_{e,1} \approx 4.12$ and $I_{e,2} \approx 15.23$. For each of these actions the elliptic points are at $\theta = 0, \pi/5, 2\pi/5, \dots, 9\pi/5$. These locations of the fixed points are in good agreement with those in Fig. 15a that are determined by numerically integrating the complete equations of motion.

The simple analysis given above breaks down as the amplitude of the perturbation is increased since the terms under the summation sign in Eq. (15) cannot be ignored. For $1/\omega_0 = 5$ and $\epsilon = 5 \times 10^{-2}$ the surface-of-section plot is shown in Fig. 15b. From this figure it is apparent that a chaotic layer in phase space develops around the separatrices. This chaotic layer grows in thickness as the amplitude of the perturbation is increased. Also, for a fixed amplitude, the thickness increases with decreasing action. This is known as web stochasticity and has been discussed in the literature [20]. As the amplitude is increased the connected region of chaos expands. However, unlike the standard map which is periodic in action, the chaotic phase space is always bounded in action for any finite amplitude. This is apparent from Fig. 15b where we note that the regions of large action are not chaotic while the regions of smaller action are chaotic.

In the off-resonance case the wave frequency is not a harmonic of the cyclotron frequency. Let us consider the slightly off-resonance case when $\omega_0 = (1 - \delta_m)/m$ where m is an integer and $|\delta_m| \ll 1$. Using arguments similar to those for the on-resonance case, the leading order Hamiltonian for small amplitudes is:

$$\bar{H}_0(\psi, J; \tau) = -\delta_m J + \epsilon J_m \left(m\sqrt{2J} \right) \cos(\psi) \quad (18)$$

where in the argument of the Bessel's function we have made use of the assumption that $|\delta_m| \ll 1$. The corresponding equations of motion are:

$$\frac{d\psi}{d\tau} = -\delta_m + \epsilon \frac{m}{\sqrt{2J}} J'_m \left(m\sqrt{2J} \right) \cos(\psi) \quad (19a)$$

$$\frac{dJ}{d\tau} = \epsilon J_m \left(m\sqrt{2J} \right) \sin(\psi) \quad (19b)$$

For $\epsilon = 0$, the leading order Hamiltonian in Eq. (18) is not zero, and from Eq. (19b) J is a constant of the motion. Thus, the surface-of-section will be made up of lines of constant I . Furthermore, for $\epsilon = 0$, there are no fixed points for Eqs. (19a) and (19b). There is a threshold value of ϵ for

which there will exist fixed points of these equations. The conditions for the existence of fixed points (ψ_h, J_h) and (ψ_e, J_e) is:

$$J_m(m\sqrt{2J_h}) = 0 \quad \text{and} \quad \epsilon \frac{m}{\sqrt{2J_h}} J'_m(m\sqrt{2J_h}) \cos(\psi_h) = \delta_m \quad (20a)$$

$$\psi_e = l\pi \quad \text{and} \quad (-1)^l \epsilon \frac{m}{\sqrt{2J_e}} J'_m(m\sqrt{2J_e}) = \delta_m \quad (20b)$$

where $l = 0, 1, 2, \dots$. It can be easily shown that, if the above conditions are satisfied, Eq. (20a) will give the hyperbolic fixed points and Eq. (20b) will give the elliptic fixed points. From Eq. (20a) the condition for the existence of a hyperbolic fixed point is:

$$\epsilon \geq \left| \frac{\delta_m \xi_h}{m^2 J'_m(\xi_h)} \right| \quad (21)$$

where $\xi_h = m\sqrt{2J_h}$ satisfies $J(\xi_h) = 0$. From Eq. (20b) the condition for the existence of elliptic fixed points at a given $\xi_e = m\sqrt{2J_e}$ is that:

$$\epsilon \geq (-1)^l \frac{\delta_m \xi_e}{m^2 J'_m(\xi_e)} \quad (22)$$

Since the local maxima of $|J'(\xi)|$ occur for those ξ where $J(\xi) = 0$, Eqs. (21) and (22) give the same condition for the threshold amplitude for the existence of hyperbolic and elliptic fixed points. One can easily show from the above expressions that the threshold amplitude increases for increasing action I and decreases for increasing harmonic number m .

As an example of a slightly off-resonance case we choose $\omega_0 = 1/5.05$, $m = 5$, so that $\delta_m \approx 0.0099$. From the conditions in Eqs. (21) and (22) we find that the threshold amplitude for the existence of elliptic (corresponding to l being an even integer) and hyperbolic fixed points is $\epsilon_{th} \approx 0.0134$. Elliptic fixed points (corresponding to l being an odd integer) have a threshold amplitude of $\epsilon_{th} \approx 0.0136$. At this amplitude there appear another set of hyperbolic fixed points. This is borne out by numerical integration of the exact equations of motion. Figs. 16a and 16b show the surface-of-section plots for $\epsilon = 10^{-2}$, which is just below the threshold amplitude for the appearance of fixed points, and $\epsilon = 2.5 \times 10^{-2}$, respectively. It should be noted that the phase-space islands are not connected to each other as in the on-resonance case. As the amplitude is increased, fixed points appear at larger values of the action while there appear regions of chaos for lower values of the action. This is evident in Fig. 16c which gives the surface-of-section for $\epsilon = 5 \times 10^{-2}$. The appearance of chaos is similar in fashion to the on-resonance case discussed earlier. Chaos appears near the separatrix and this region widens in phase space as the amplitude is increased. The chaotic region is always bounded in action.

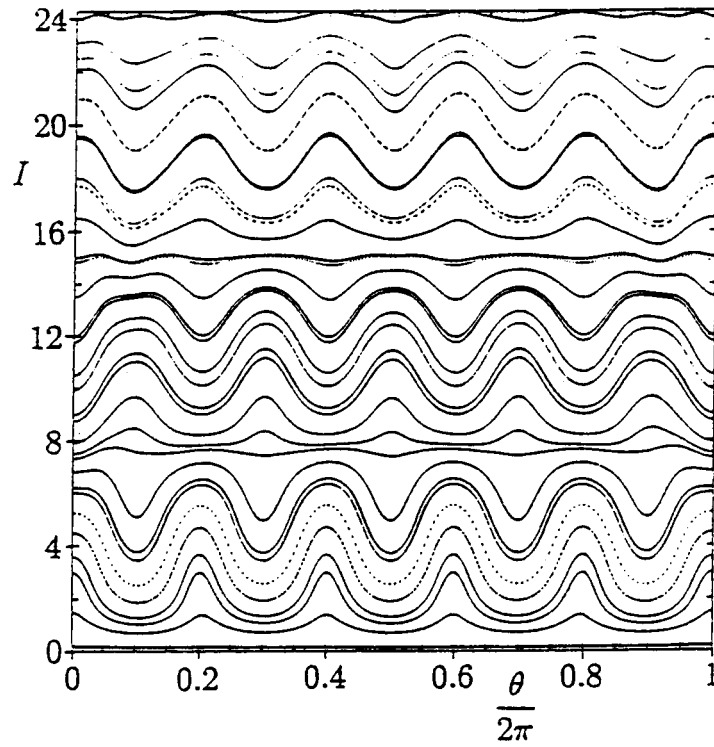


Figure 16a. Surface-of-section for $\omega_0 = 1/5.05$ and $\epsilon = 10^{-2}$.

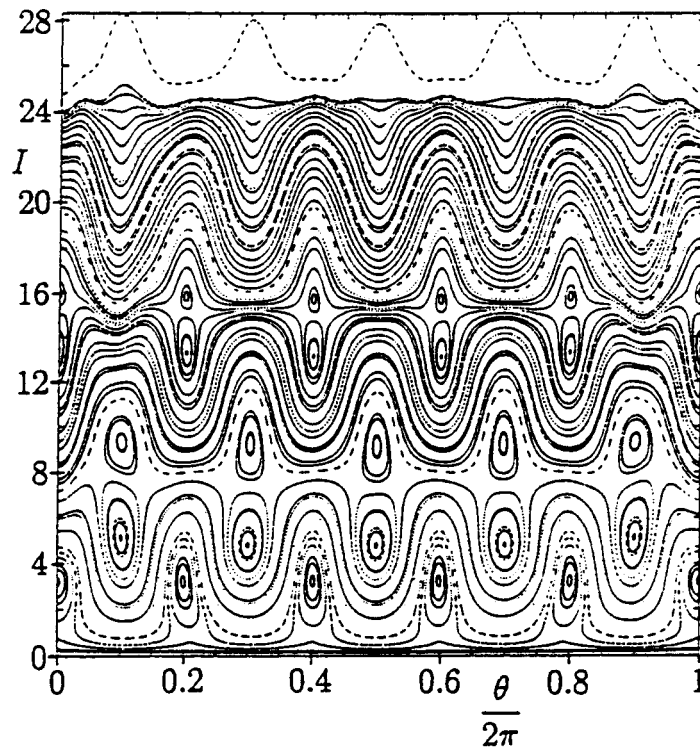


Figure 16b. Surface-of-section for $\omega_0 = 1/5.05$ and $\epsilon = 2.5 \times 10^{-2}$.

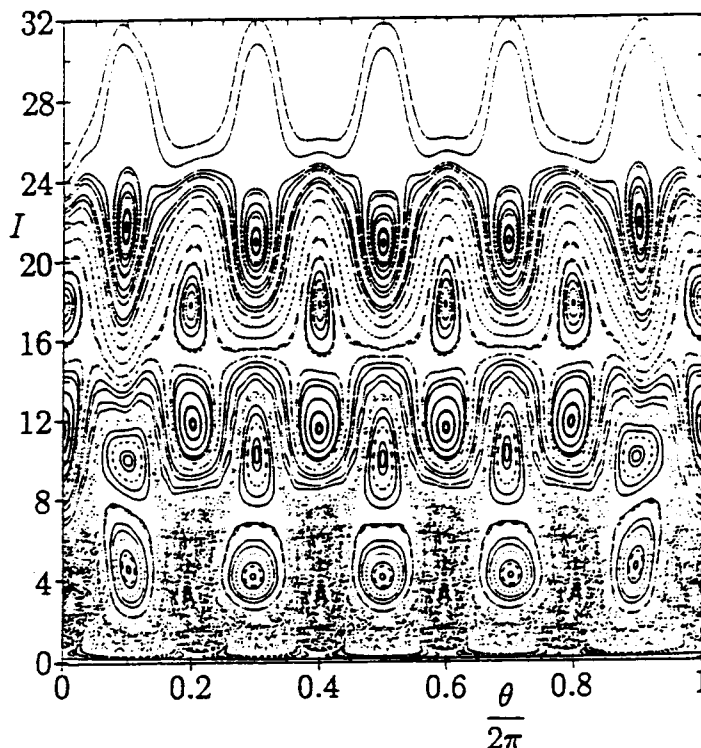


Figure 16c. Surface-of-section for $\omega_0 = 1/5.05$ and $\epsilon = 5 \times 10^{-2}$.

VII. CONCLUSIONS - GLOBAL DESCRIPTIONS

We have illustrated features of chaotic particle motion in prescribed coherent fields and conditions for the existence of such motion using models which are paradigms of nonlinear wave-particle dynamics. When there is a region in phase space that is chaotic, an initial distribution of particles, which is localized in action in the chaotic part of phase space, will spread out to cover the entire region of connected chaos in action. This was shown for the standard map, in Figs. 8a and 8c, where a localized circle of initial conditions evolved to fill up the entire chaotic phase space. It was also shown that nearby orbits diverged exponentially, thereby making it difficult/impossible to keep track of an orbit of a particle accurately in the chaotic phase space, thus rendering the interaction irreversible.

Based upon the above, one may attempt to describe the statistical evolution of a distribution of particles when the dynamics is chaotic. If an initial distribution of particles is localized in action near small values of the action in chaotic phase space, they will, on the average, gain energy and/or momentum from the wave as they spread to cover higher values of the actions in the chaotic phase space. Particles which stick to KAM

surfaces will, on the average, not gain energy and/or momentum from the waves. In the chaotic phase space, the particle dynamics appears as if the particles are acted upon by random forces. In such circumstances one attempts to describe the evolution of a distribution function through the Fokker-Planck equation, where the chaotic dynamics is accounted for by a diffusion coefficient. Although this is very useful as a global description, there are many uncertainties and limitations associated with such a description of Hamiltonian chaos. In cases of physical interest, the chaotic phase space is bounded, as in Figs. 15b and 16c, and there are regions of coherent motion imbedded in regions of chaotic phase space. Also, in chaotic phase space there persist long-time correlations, *i.e.* the orbits of particles do not become randomized or ergodic on a short time scale (*e.g.* if the standard map represented Brownian motion, then the correlation time would be one iterate of the map – this is clearly not the case since, based on the computational results in Figs. 8a and 10, correlations exist over many iterates of the map). These issues complicate the derivation of the Fokker-Planck description and the associated evaluation of the diffusion coefficient. Some aspects of these issues remain unresolved. A study of the Fokker-Planck description and the diffusion coefficient is beyond the scope of this tutorial. However, the reader is referred to [2, 21] for details and further discussion. Finally, we want point out that in some chaotic dynamics of wave-particle interactions one encounters “chaotic streaming” [22, 23] for which a Fokker-Planck description is inadequate [24, 25].

ACKNOWLEDGEMENTS

This work was supported by NASA Grant No. NAGW-2048, by DOE Grant No. DE-FG02-91ER-54109, and by NSF Grant No. ECS-88-22475.

REFERENCES

- [1] M. V. Berry, in *Topics in Nonlinear Dynamics, Volume 46*, S. Jorna, ed. (American Institute of Physics, New York, 1978), p. 16.
- [2] A. J. Lichtenberg, M. A. Lieberman, *Regular and Stochastic Motion* (Springer-Verlag, New York, 1983).
- [3] M. Tabor, *Chaos and Integrability in Nonlinear Dynamics: An Introduction* (John Wiley, New York, 1989).
- [4] H. Goldstein, *Classical Mechanics* (Addison-Wesley, Massachusetts, 1980).
- [5] B. J. Taylor, Culham Lab. Prog. Report CLM-PR 12 (1969).
- [6] B. V. Chirikov, Phys. Rep. 52, 263 (1979).
- [7] See [1] and references therein.

- [8] G. D. Birkhoff, *Mem. Pont. Acad. Sci. Novi. Lyncaei* 1, 85 (1935).
- [9] A. N. Kolmogorov, *Dokl. Akad. Nauk. SSSR* 98, 525 (1954).
- [10] V. I. Arnold, *Russ. Math. Surveys* 18, 85 (1963).
- [11] J. Moser, *Nachr. Akad. Wiss. Goettingen Math. Phys. K1*, 1 (1962).
- [12] J. Greene, *J. Math. Phys.* 20, 1183 (1979).
- [13] T. Chang and B. Coppi, *Geophys. Res. Lett.* 8, 1253 (1981).
- [14] G. R. Smith and A. N. Kaufman, *Phys. Rev. Lett.* 34, 1613 (1975).
- [15] A. Fukuyama, H. Momota, R. Itatani, and T. Takizuka, *Phys. Rev. Lett.* 38, 702 (1977).
- [16] C. F. F. Karney and A. Bers, *Phys. Rev. Lett.* 39, 550 (1977).
- [17] C. F. F. Karney, *Phys. Fluids* 21, 1584 (1978).
- [18] R. L. Lysak, in *Ion Acceleration in the Magnetosphere and Ionosphere, Geophysical Monograph Series, Volume 38*, T. Chang, M. K. Hudson, J. R. Jasperse, P. M. Kintner, M. Schulz, and G. B. Crew, eds. (American Geophysical Union, Washington, D.C., 1986), p. 261.
- [19] M. Abramowitz and I. A. Stegun, *Handbook of Mathematical Functions* (Dover Publications, New York, 1972).
- [20] G. M. Zaslavsky, *Chaos* 1, 1 (1991).
- [21] A. K. Ram, A. Bers, and K. Kupfer, *Phys. Lett. A* 138, 288 (1989).
- [22] K. Kupfer, A. Bers, and A. K. Ram, in *Research Trends in Physics: Nonlinear and Relativistic Effects in Plasmas*, V. Stefan, ed. (American Institute of Physics, New York, 1992), p. 670.
- [23] S. D. Schultz, A. Bers, and A. K. Ram, in *Radio Frequency Power in Plasmas, Conference Proceedings No. 289*, M. Porkolab and J. Hosea, eds. (American Institute of Physics Press, New York, 1994), p. 433; and Plasma Fusion Center Report, PFC/JA-93-5, Massachusetts Institute of Technology, Cambridge, MA (1993).
- [24] V. A. Afanasiev, R. Z. Sagdeev, and G. M. Zaslavsky, *Chaos* 1, 143 (1991).
- [25] G. M. Zaslavsky, D. Stevens, and H. Weitzner, *Phys. Rev. E* 48, 1683 (1993).
- [26] E. T. Whittaker, *A Treatise on the Analytical Dynamics of Particles and Rigid Bodies* (Dover Publications, New York, 1944).
- [27] I. S. Gradshteyn and I. M. Ryzhik, *Table of Integrals, Series, and Products* (Academic Press, Boston, 1994).

APPENDIX A: PARTICLE MOTION IN A PLANE WAVE

Consider a particle which at time $t = 0$ has $q = q_0$ and $p = p_0$. Since $H(q_0, p_0) = p_0^2/2 + \alpha \cos(q_0) \equiv H_0$ is a constant of the motion, i.e. the particle's q and p at some time t are such that $p^2/2 + \alpha \cos(q) = H_0$, using Eq. (2a) we get:

$$\int_{q_0}^q \frac{dq'}{\sqrt{H_0 - \alpha \cos(q')}} = \sqrt{2} \int_0^t dt' \quad (A1)$$

The integral on the left-hand side can be evaluated analytically [26, 27] for the case of trapped and passing particles.

Trapped Particles

Since $|H_0| \leq \alpha$ for trapped particles, $|q| \leq \cos^{-1}(H_0/\alpha)$. The maximum value of $|q|$ corresponds to the turning point of the trapped particle. Without loss of generality, we can set $q_0 = \pi$. Then the solution of Eq. (A1) is:

$$q = 2 \cos^{-1} [\kappa \operatorname{sn}(K(\kappa^2) + \sqrt{\alpha}t \mid \kappa^2)] \quad (A2)$$

where $\kappa^2 = (H_0 + \alpha)/(2\alpha)$, $K(\kappa^2)$ is the complete elliptic integral of the first kind, and sn is the sine amplitude Jacobian elliptic function [19]. (Note that the complete elliptic integral of the first kind will be referred to as $K(\kappa^2)$ in order to distinguish it from the amplitude of the standard map.) From Eq. (A2) it readily follows that:

$$p = -2\kappa\sqrt{\alpha} \operatorname{cn}(K(\kappa^2) + \sqrt{\alpha}t \mid \kappa^2) \quad (A3)$$

where cn is the cosine amplitude Jacobian elliptic function [19].

Passing Particles

For untrapped particles $H_0 > \alpha$ and we assume that $q_0 = 0$. Then, Eq. (A1) gives:

$$q = 2 \cos^{-1} \left[\operatorname{sn} \left(K(\beta^2) + \frac{\sqrt{\alpha}}{\beta} t \mid \beta^2 \right) \right] \quad (A4)$$

where $\beta = 1/\kappa$. Using Eq. (2a):

$$p = -2\frac{\sqrt{\alpha}}{\beta} \operatorname{dn} \left(K(\beta^2) + \frac{\sqrt{\alpha}}{\beta} t \mid \beta^2 \right) \quad (A5)$$

where dn is the delta amplitude Jacobian elliptic function [19].

APPENDIX B: ACTION-ANGLE VARIABLES FOR THE NONLINEAR OSCILLATOR

The action-angle variables can be obtained by solving the Hamilton-Jacobi equation [4]. Here we give the results without going into details

of the Hamilton-Jacobi theory.

The action variable is defined as:

$$I = \frac{1}{2\pi} \oint dq p = \frac{1}{\sqrt{2}\pi} \oint \sqrt{H_0 - \alpha \cos(q)} \quad (B1)$$

where the integral is over one orbit for a trapped particle, and from 0 to 2π for the passing particle. The action is a constant of the motion (being a function of H_0 only) and the Hamiltonian can be expressed as a function of I only. The angle coordinate is given by:

$$\theta = \frac{1}{\sqrt{2}} \frac{\partial H_0}{\partial I} \int_{q_0}^q dq' \frac{1}{\sqrt{H_0 - \alpha \cos(q)}} \quad (B2)$$

where q_0 is the initial coordinate of the particle. As in Appendix A we treat passing and trapped particles separately.

Trapped Particles

The integral in Eq. (B1), tabulated in [27], is evaluated by appropriately accounting for the turning points of the trapped particle. This gives:

$$I = \frac{8}{\pi} \sqrt{\alpha} [(\kappa^2 - 1) K(\kappa^2) + E(\kappa^2)] \quad (B3)$$

where $E(\kappa^2)$ is the complete elliptic integral of the second kind [19]. The action is a function of the Hamiltonian only. This relationship can be inverted to express the Hamiltonian as a function of the action only. Thus, the action is a constant of the motion.

Since all trapped particles pass through the point $q = \pi$, the integral in Eq. (B2) for the angle is evaluated by setting $q_0 = \pi$. Again, this integral is tabulated in [27] and we find:

$$\theta = \frac{\pi}{2K(\kappa^2)} F(\eta, \kappa^2) \quad (B4)$$

where F is the elliptic integral of the first kind [19], and $\kappa \sin(\eta) = \cos(q/2)$. The frequency of oscillation, Ω_{tr} for the trapped particles is given by the time derivative of Eq. (B4). This is equivalent to taking the derivative of the Hamiltonian with respect to the action [4]. Thus:

$$\Omega_{tr} \equiv \frac{d\theta}{dt} = \frac{dH_0}{dI} = \frac{\pi}{2} \frac{\sqrt{\alpha}}{K(\kappa^2)} \quad (B5)$$

Passing Particles

The action is:

$$I = \frac{4}{\pi} \sqrt{\alpha} \kappa E(\beta^2) \quad (B6)$$

where β is defined in Appendix A.

The angle θ is obtained from Eq. (B2) by setting $q_0 = 0$. The resulting integral is tabulated (see [27]) so that:

$$\theta = \frac{\pi}{K(\beta^2)} F(\xi, \beta^2) \quad (B7)$$

where $\sin(\xi) = \sin(q/2)/\cos(\eta)$. The frequency of oscillation for the passing particles, where a single oscillation corresponds to going from $q = 0$ to $q = 2\pi$, is:

$$\Omega_p \equiv \frac{d\theta}{dt} = \frac{dH_0}{dI} = \frac{\pi\kappa\sqrt{\alpha}}{K(\beta)}. \quad (B8)$$

APPENDIX C: DERIVATION OF THE STANDARD MAP

Here we solve Eqs. (9a) and (9b) and derive the standard mapping equations. Let $\theta_{n-\epsilon}$ and $I_{n-\epsilon}$ be the angle and action of the particle, respectively, at time $\tau_0 = n - \epsilon$ (where $\epsilon \ll 1$). Thus, τ_0 is the time just before the particle receives its n -th kick. The action of the particle $I(\tau)$ at a subsequent time τ , where $n < \tau < (n+1) - \epsilon$, is obtained by integrating Eq. (9b):

$$I(t) - I_{n-\epsilon} = K \sin(\theta_n) \quad (C1)$$

where $\theta_n = \theta(n)$ is the angle of the particle at time n . Then, from Eq. (9a), the angle of the particle at time t is:

$$\theta(t) - \theta_{n-\epsilon} = \{I_{n-\epsilon} + K \sin(\theta_n)\} (\tau - \tau_0) \quad (C2)$$

If $\theta_{n+1-\epsilon}$ and $I_{n+1-\epsilon}$ are the angle and action of the particle, respectively, at time $\tau = (n+1) - \epsilon$, then, in the limit $\epsilon \rightarrow 0$ Eqs. (C1) and (C2) reduce to the mapping equations (7a) and (7b).